Lappeenranta University of Technology

School of Energy Systems

Energy Technology

Heimo Hiidenkari

Dynamic Core-Annulus Model of Circulating Fluidized Bed Boilers

Master's Thesis

Examiner: Docent (D.Sc. Tech.) Jouni Ritvanen

Professor, (D.Sc. Tech.) Timo Hyppänen

Supervisors: M.Sc. Tech. Sami Tuuri

Lic.Sc. Tech. Jari Lappalainen

ABSTRACT

Lappeenranta University of Technology
School of Energy Systems
Energy Technology

Heimo Hiidenkari

Dynamic Core-Annulus Model of Circulating Fluidized Bed Boilers

Master's Thesis

2018

115 pages, 66 figures, 11 tables and 4 appendices.

Examiners: Docent (D.Sc. Tech.) Jouni Ritvanen
Professor, (D.Sc. Tech.) Timo Hyppänen

Keywords: circulating fluidized bed, CFB, core, annulus, dynamic, simulation, 1D, 1.5D, Apros, hydrodynamics, heat transfer

This Master's Thesis presents a dynamic core-annulus model of circulating fluidized bed (CFB) boilers which is implemented in Apros simulation software. In describing and verifying the model, the focus is on the solids balance and heat transfer inside the furnace. The model is to be used as a training simulator and engineering tool for CFB boilers.

The first objective of the work was to gather a comprehensive theory basis on CFBs, focusing on the main physical phenomena inside the furnace. The second objective was to document the modelling solutions of the new CFB model that were implemented in the Apros environment. The third objective was to develop and verify the CFB model so that the desired scope of operation is met.

The first and second objectives were met, but the third was not. The CFB model was further developed by using the theory basis gathered in this work. In addition, the theory basis acted as a foundation in determining the correctness of the model and the future development needs found with the simulation cases. The mass and heat balances of the model were verified and found correct. The functionality of the model was verified with six simulation cases. The model did well in the cases, but in some of them, single variables had to be controlled to get realistic results. The simulation cases showed that the model can be made to work realistically, but it demands experience and understanding of the functionality of the model. Therefore, the functionality of the model is not yet on a desired stage. The simulation cases were however successful in revealing important subjects of development for the model. Further development of the model is continued in the future.

TIIVISTELMÄ

Lappeenrannan teknillinen yliopisto
LUT School of Energy Systems
Energiatekniikan koulutusohjelma

Heimo Hiidenkari

Dynaaminen core-annulus-malli kiertoleijupedille

Diplomityö

2018

115 sivua, 66 kuvaa, 11 taulukkoa ja 4 liitettä.

Tarkastajat: Dosentti, TkT Jouni Ritvanen
Professori, TkT Timo Hyppänen

Hakusanat: kiertoleijupeti, CFB, dynaaminen, simulointi, 1D, 1.5D, Apros, hydrodynamiikka, lämmönsiirto

Tässä diplomityössä esitellään dynaaminen core-annulus-malli kiertoleijupedeille (CFB), joka on toteutettu Apros-simulointiohjelmistolle. Mallin kuvauksessa ja verifioinnissa keskitytään kiintoainetaseeseen sekä lämmönsiirtoon kattilan sisällä. Mallin käyttötarkoitus on toimia koulutussimulaattorina ja insinöörityökaluna CFB-kattiloille.

Työn ensimmäisenä tavoitteena oli kerätä kattava teoriakatsaus kiertoleijupedeistä, keskittyen merkittävimpiin ilmiöihin kattilan sisällä. Toisena tavoitteena oli dokumentoida Apros-ympäristöön tehdyn uuden CFB-mallin mallinnusratkaisut. Kolmantena tavoitteena oli kehittää ja verifioida CFB-mallia, jotta mallin toiminta saadaan halutulle tasolle.

Ensimmäinen ja toinen tavoite saavutettiin, kolmatta tavoitetta ei. CFB-mallia jatkokehitettiin työssä kerätyn teoriakatsauksen avulla. Lisäksi teoriakatsaus toimi perustana mallin oikeellisuuden arvioinnille sekä tulevaisuuden jatkokehitys -tarpeille, jotka löydettiin simulointikokeiden yhteydessä. Työssä verifioitiin mallin massa- ja energiataseet, jotka todettiin paikkansapitäviksi. Mallin toimintaa verifioitiin kuudella simulointikokeella. Malli suoriutui kokeista, mutta osassa tapauksista yksittäisiä parametreja oli säädettävä realististen tulosten saamiseksi. Simulointitapaukset osoittivat, että mallin saa toimimaan realistisesti, mutta se vaatii kokemusta ja ymmärrystä mallin toiminnasta. Täten mallin toiminta ei ole vielä halutulla tasolla. Simulointitapauksilla onnistuttiin kuitenkin selvittämään tärkeitä kehityskohteita mallille. Mallin kehitys jatkuu tulevaisuudessa.

ACKNOWLEDGEMENTS

This work was done for Fortum, in Keilaniemi, Espoo. The work was a joint project between Fortum and VTT Technical Research Centre of Finland. During these eight months, I have have been happy to work as a part of a creative and motivated team, in a creative and motivating work environment.

I would like to thank my instructors Sami Tuuri and Jari Lappalainen. Your advice and guidance always helped me go forward and see things more clearly. Special thanks also to Jukka Ylijoki for programming the CFB model and for giving insightful advice. I am grateful to keep working with you after this thesis.

Many thanks to my examiner, Docent Jouni Ritvanen from Lappeenranta University of Technology for your expert advice regarding CFBs, mathematical modelling and the writing process. I express my gratitude also to Professor Timo Hyppänen for his guidance by the end of this work.

I am thankful to the work community in Fortum, especially the Apros team which I was a part of. Your support and advice was invaluable. I would also like to thank my respected colleague and great friend, Jaakko Timonen, for his support during the journey of this work. I am more than grateful for my family and friends who supported me during this work.

Espoo 17.10.2018

Heimo Hiidenkari

TABLE OF CONTENTS

NOMENCLATURE

A	node cross sectional area	m^2
D_{eq}	equivalent diameter of a column	m
d	diameter	m
g	acceleration due to gravity	9.81 m/s^2
H	height	m
h	heat transfer coefficient	$W/m^2/K$
k	coefficient	-
m	mass	kg
$\dot{m}$	mass flow	kg/s
P	pressure	Pa, kPa, bar
Q	energy	kJ
q	energy flow	W
q_m	mass flow	kg/s
T	temperature	K, °C
t	time	s
u	velocity	m/s
V	node volume	m^3
z	height, axial position	m

Greek Letters

α	split coefficient from core to annulus	-
β	split coefficient from annulus to core	-
δ	wall layer thickness	m
ε	voidage	-
μ	dynamic viscosity	kg/m/s
ρ	density, suspension density	kg/m^3

Subscripts

a	annulus
ac	annulus to core
avg	average

c	core
ca	core to annulus
end	at the end of simulation
g	gas
hdb	high-density bed
i	i^{th} element/node
int	interface
p	particle
s	solids
t	terminal
tot	total
vel	velocity

Superscripts

*	dimensionless

Abbreviations

1D	one-dimensional
1.5D	core-annulus
BFB	bubbling fluidized bed
CFB	circulating fluidized bed
EHE	external heat exchanger
LHV	lower heating value
HTC	heat transfer coefficient
PA	primary air
PC	particle convection
PSC	particle storage component
SA	secondary air
SCL	Simantics Constraint Language
WWHE	wing wall heat exchanger

1 INTRODUCTION

1.1 Background

The climate system has been warming over the period of 1880–2012, as stated by the International Panel of Climate Change (Wang et al. 2016). There is increasingly more evidence that global warming is mainly caused by human-generated greenhouse gases, carbon dioxide for the most part (Huang et al. 2012). Figure 1.1 by the International Energy Agency shows that in 2017, 61 % of global carbon dioxide (CO_2) emissions were generated by industry and production of electricity and heat. Emissions from biomass are not included in the figure. As energy consumption in each of these fields is bound to rise in the future, cleaner ways of producing the energy must grow in number to hinder global warming.

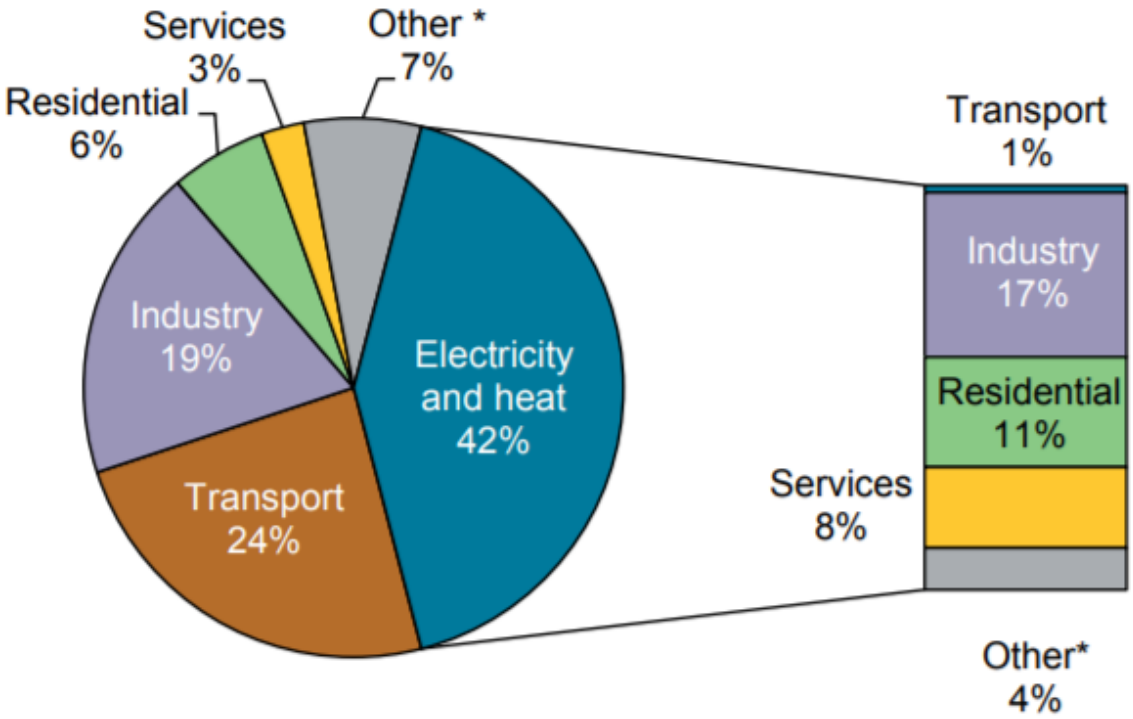

Figure 1.1. World CO_2 emissions from fuel combustion, by section, in 2015. * Other includes agriculture/forestry, fishing, energy industries other than electricity and heat generation, and other emissions not specified elsewhere. (IEA 2017.)

Fluidized bed combustion has become one of the most environmentally friendly ways to burn solid fuel. Different fuels, even those of lower quality, can be burned with minor emissions, because the fuel burns efficiently and emission control is relatively easy.

(Hyppänen & Raiko 1995, 417) Even as the future prospects of fossil fuels are weak, fluidized bed combustion stays relevant in burning biomass. The world's largest biomass-only fluidized bed boiler of 299 MW_e starts its operation in 2020, in Teesside, UK (Amec Foster Wheeler 2016). Biomass is a renewable energy source and in many applications it can be considered carbon neutral, meaning zero impact to global CO_2 levels.

1.2 Research Problem, Objectives and Exclusions

Dynamic modelling and simulation of power plants is very important for the energy industry. It for example aids process optimization, helps analyse and improve safety issues and assists the training of power plant operators. Apros simulation software is a comprehensive tool made for the dynamic modelling and simulation of process, automation and electrical systems. A circulating fluidized bed (CFB) model has been developed for it prior to this thesis, see (Lappalainen et al. 2014; Lappalainen et al. 2017). The model could not, however, simulate all of the desired operation conditions, such as the startup and shutdown of a furnace. To expand the scope of operation, the solid balance structure of the Apros CFB model was redesigned. Not everything in the model was redesigned, and the model required further development, thorough testing and verification. This thesis was commissioned for this reason. The desired scope of operation includes the following items:

1. Adding new material to the furnace does not cause unrealistic behaviour in the solid phase;
2. Startup and shutdown of the furnace can be simulated;
3. The model is capable for certain special cases, such as emptying the furnace or a sudden stop in air feed;
4. The heat transfer submodel better reflects the real physical phenomenon.

This thesis has three objectives:

1. To gather a comprehensive theory basis on fluidization and existing dynamic 1D CFB models, focusing on the physical phenomena inside a CFB, especially hydrodynamics and heat transfer;
2. To document the modelling solutions implemented in the current Apros CFB model;
3. To develop and verify the CFB model so that the desired scope of operation is met.

To reach the first objective, a theoretical overview of CFBs is made, explaining the basic phenomena inside the CFB furnace. The information is to be used as a backbone for the CFB

model development by identifying the most crucial physical phenomena in the furnace and by guiding the decisions on modelling solutions. Also, a review on existing models is to be made to identify the necessary development areas. To reach the second objective, the modelling solutions implemented in the current Apros CFB model have to be thoroughly documented. The soundness of the modelling solutions is to be addressed and sensitivity analyses are to be made for the most important empirical correlations used. Finally, to reach the third objective, the Apros model should be verified. The model will be used as a training simulator and engineering tool for CFB boilers and therefore, at this development stage, a smaller accuracy of the model is accepted, the focus being in getting transient responses in the process as physically plausible.

Figure 1.2 shows the process of model development, verification and validation and their meanings in detail. A mathematical model is verified to determine that the model implementation accurately represents the developers' conceptual description of the model (Thacker et al. 2004, 10). For verification to be successful, the model must have no errors in it and it has to work as planned. After verification, the model is validated, to determine how accurate a representation the model is of the real world process from the perspective of the intended uses of the model (Ibid., 13).

For validation to be successful, the model's predictive capability of experimental data has to be within a decided threshold. In this work, the CFB model is only verified by succeeding in mass and heat balance tests and specific cases. The model will not be validated in this work, because there is no sufficient experimental data available and because validation would be too time-consuming for this work.

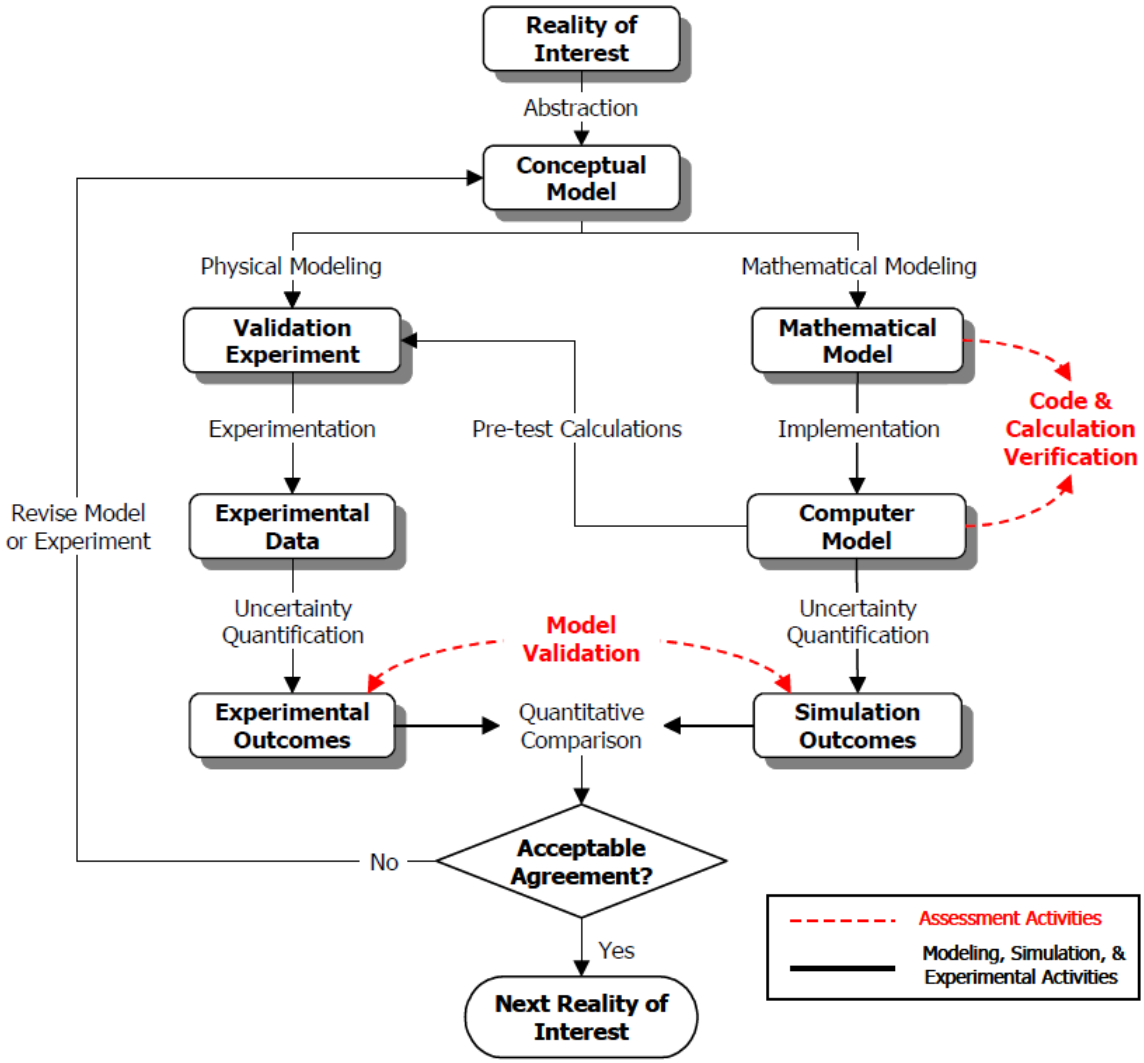

Figure 1.2. A detailed process of model development, verification and validation (Ibid., 7).

The theoretical scope of CFB boilers is tremendous, so certain aspects must be excluded from the work in order for it to be coherent and sufficiently compact. Accordingly, the CFB theory in this thesis will focus on furnace hydrodynamics and heat transfer, while combustion is discussed only shortly and emissions are entirely excluded from this thesis. Moreover, everything that the CFB bed material does not touch is excluded from the scope of the theory part. But, in the model verification part, a water/steam loop and simple automation are used for the CFB boiler. Lastly, as the objective is to further develop the one-dimensional (1D) dynamic CFB model, only dynamic modelling and published dynamic 1D models are discussed.

1.3 Thesis Structure

This thesis essentially comprises three parts:

1. An overview of CFB theory;
2. A review of CFB models and the introduction of the Apros model;
3. The operation of the Apros model.

The theory part begins with basics of fluidization and then moves on to CFBs specifically. The most crucial processes in CFB boilers regarding hydrodynamics, combustion and heat transfer are discussed, with more focus given to the processes to be modelled.

Then, five dynamic 1D CFB models are reviewed, with the most crucial and interesting aspects highlighted. Some of this information is then used in modelling the CFB components, which is presented after the model review. A comprehensive presentation and analysis of equations and modelling solutions for the model are given.

The third part of the work consists of verifying the model. The functionality of the model is first verified with mass and heat balances. Then the transient responses of the model are tested with cases where one input parameter is varied at a time. Finally, verification and testing results are discussed, and attention is drawn on the soundness of modelling solutions. Model improvement options in the future are discussed, and finally, conclusions are drawn.

2 FLUIDIZATION

This chapter explores the basics of fluidization and fluidized bed combustion. The purpose of this chapter is to build a general understanding of fluidization regimes and fluidized bed boilers. This is important for understanding the concepts of the CFB furnace, introduced in Chapter 3.

Fluidization occurs when fluid is blown or pumped through a bed of small particles at a sufficient velocity. When fluidized, the bed expands and starts to behave like a liquid. This means for example good mixing of particles in the bed. Fluidization is used in numerous applications in different fields of technology, including drying or coating of particles, but perhaps the most notable application is fluidized bed combustion.

Fluidized beds can be divided into different types, depending e.g. on fluid velocity and particle size and density. This chapter introduces the main fluidization regimes but focuses mostly on bubbling fluidized beds (BFB) and CFBs.

2.1 Fluidized Beds

When gas flows upwards through a bed of fine solids at a low flow velocity, it flows in the gaps between the particles. The particles may vibrate, but the bed remains stationary. This is called a fixed bed, Figure 2.1a. (Kunii & Levenspiel 1991, 1.)

Increasing the gas velocity increases drag force of the gas on the particles. Increasing the velocity enough makes the drag force counterbalance the weight of the bed and the bed becomes fluidized, Figure 2.1b. The gas velocity needed for this is called the minimum fluidization velocity. (Ibid.)

When gas velocity is further increased, gas bubbles begin to form in the bed and the bed reaches a state called bubbling fluidization, Figure 2.1c. For larger particles this happens immediately after minimum fluidization, but for finer particles the needed velocity can be several times larger than the minimum fluidization velocity. (Kunii & Levenspiel 1991, 1–2; 73.)

The BFB consists of two phases: gas bubbles and solid suspension. A portion of the gas keeps the solid suspension at minimum fluidization and the extra gas flows in the suspension as bubbles. The bubbles travel upwards in the suspension due to buoyancy, passing by the solids. Bubbles pull some particles upwards in their wakes and as the bubbles reach the bed surface, they erupt, throwing particles into the freeboard, the space above the bed. (Basu 2015, 24.)

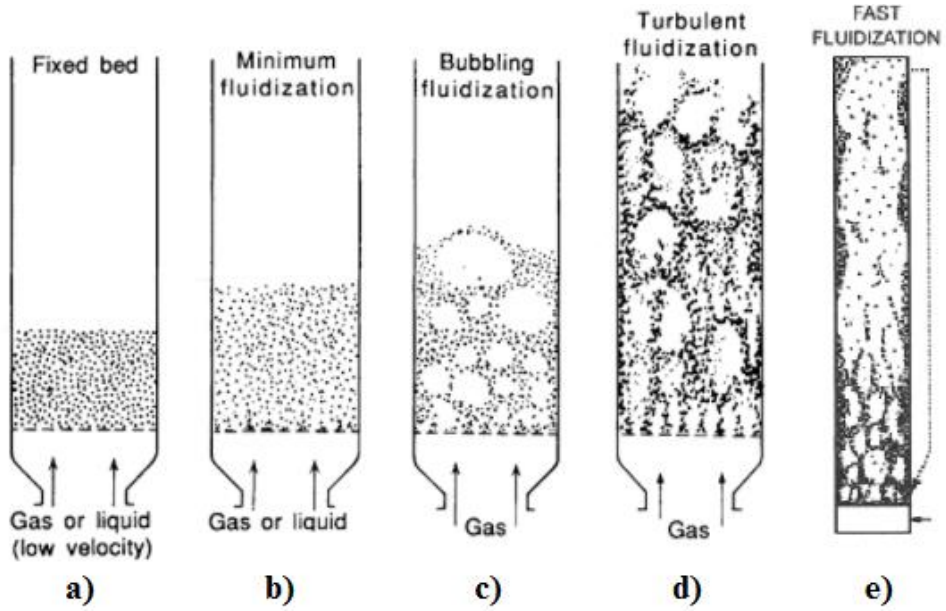

Figure 2.1. Regions of fluidization (Kunii & Levenspiel 1991, 2; Grace et al. 1997, 7).

Increasing the gas velocity in a BFB, the bed reaches a point where the bubbles coalesce and break up vigorously and instead of bubbles in a coherent bed, there are solid clusters and voids of gas of many sizes and shapes. Solids are thrown into the freeboard, but only the finer particles in the solids are entrained with the gas. Massive migration of solids with the gas does not yet occur at this velocity and the vast majority of the particles fall back into the bed. This is called a turbulent bed, Figure 2.1d (Basu 2015, 25–27; Kunii & Levenspiel 1991, 3.)

Increasing the gas velocity of a turbulent bed causes more and more particles to be entrained with the gas, until the gas reaches a velocity that is high enough to transport every particle from the bed. It then needs a return mechanism for the solids in order for the bed to keep on existing. This kind of bed is called a fast bed, Figure 2.1e. (Basu 2015, 29–30.) CFB boilers

normally operate in the fast bed regime. Therefore, the fast bed hydrodynamics and heat transfer will be covered in more detail, in Chapter 3.

2.2 Fluidized Bed Combustion

Fluidized beds were invented in 1921, but fluidized bed combustion did not enter commercial energy production until the 1970's (Basu 2015, 1; Teir 2003, 37). It has since proven to be very advantageous in energy production, and is used especially in combustion of biomass and when low nitrogen oxide (NO_x) and sulphur emissions are required (Vakkilainen 2017, 15).

There are two types of commercial fluidized bed boilers: BFBs and CFBs. In a BFB, the bed is in the bubbling regime and the particles generally remain in the bed. In a CFB, the bed is in the turbulent and fast regimes. Particles circulate both internally and externally with the help of external circulation components, promoting the mixing of gases and particles.

Figure 2.2 shows the structures of a BFB and a CFB boiler. By referring to the plant worker in both pictures, the size difference of the boilers can be grasped. The CFB boiler is discussed in more detail in the next chapter.

The main advantage of BFB boilers over CFB boilers is that they are more flexible in respect of fuel quality than CFB boilers. CFB boilers on the other hand have higher combustion efficiencies than BFBs and their emissions are smaller. Generally, the power output of a BFB boiler is lower than 100 MW_e, whereas for CFB boilers it is between 100 and 500 MW_e. (Teir 2003, 38–39.) The main reason why BFB boilers are not used in bigger units is that the cross-section of the bed would have to be very large (Vakkilainen 2017, 15).

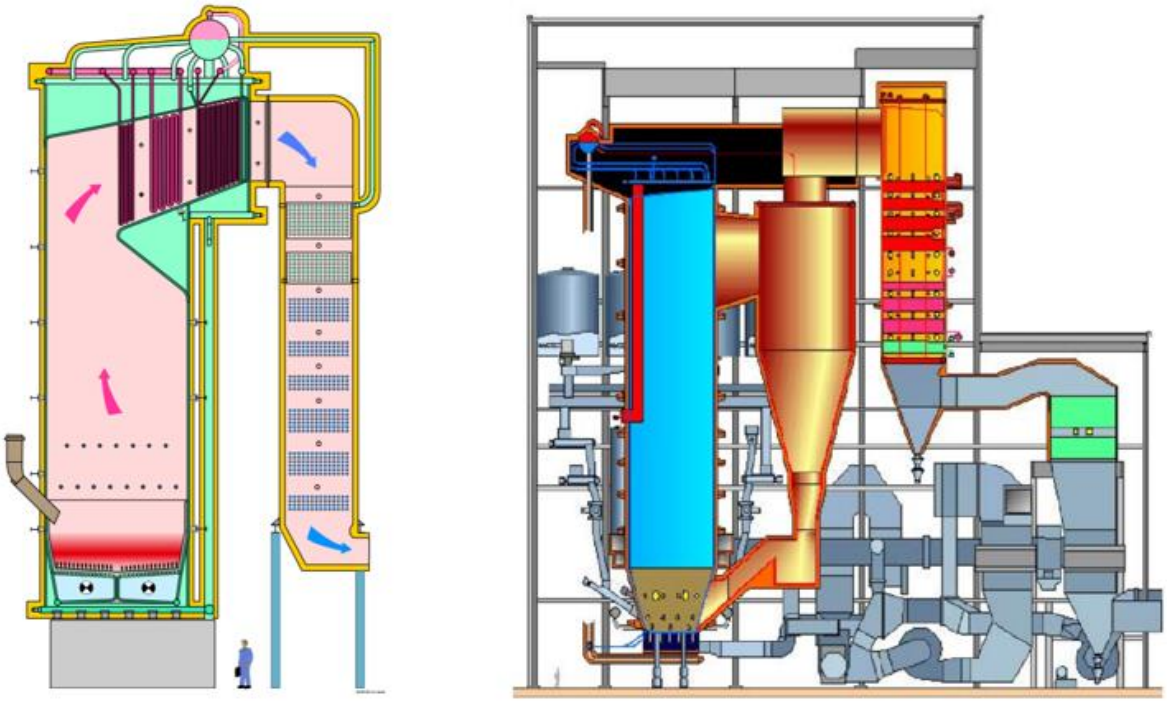

Figure 2.2. Fluidized bed boilers: a) BFB, 30.8 MW_{th}; b) CFB, 550 MW_{th}. (Teir 2003, 38; 43.)

Fluidized bed boilers have an immense mass of mixing hot solids. The bed consists of mainly sand, ash, lime, gypsum and fuel. The burning fuel particles only comprise roughly 1…3 % of the total bed mass (Basu 2015, 92). Therefore, due to the large thermal mass of the bed in relation to fuel, the fuel dries and heats up to its ignition temperature quickly without having much effect on the average temperature of the bed. This allows a large variety of fuels to be used in BFBs and CFBs. Even low quality fuels can be used with a high combustion efficiency in the same boiler. (Huhtinen et al. 2000, 157–160.)

The mixing action of hot solids stabilizes temperature gradients in the bed, meaning that the bed is almost isothermal. In a CFB boiler, where the particles flow even in the upper parts of the furnace, the whole furnace is close to isothermal. Hot particles in the upper furnace significantly increase the heat transfer rate in a CFB compared to a BFB. The efficient mixing also means that the amount of unburnt fuel is low as fuel particles come into contact with oxygen efficiently.

The temperature of fluidized beds is relatively low, typically around 850 °C, the temperature range being between 800…900 °C. There are several reasons why the beds are not hotter. A

bed with a higher temperature would mean that the ash in the bed would begin to melt, resulting in particle agglomerates, which would have an influence on fluidization. Also, an increased temperature increases the formation of thermal NO_x emissions. In addition, sulphur emission control is done by inserting lime into the furnace and the sulphur capture reaction is at its optimum at approximately 850 °C. The vaporization of alkali metals from the fuel is also reduced at lower temperatures. This means that fouling, caused by condensation of the alkali metals to boiler tubes, is significantly reduced. (Basu 2015, 115.)

The air injection to fluidized bed boilers is divided between at least two locations. Primary air, injected through nozzles at the bottom of the furnace, is used to keep the bottom bed at a desired fluidization regime, having desired combustion characteristics. In normal operation, primary air comprises around 40…60 % of the stoichiometric air amount. The remaining air, secondary air, is typically injected above the refractory lining of the lower furnace. The secondary air injection finishes the combustion of volatiles released from the fuel and helps reduce NO_x emissions. The secondary air increases gas velocity above the feed ports, making the bed less dense above the secondary air injection in CFB boilers. The furnace bottom is typically narrower in cross-section than the upper furnace to maintain more similar superficial velocities before and after secondary air injection (Basu 2015, 172–175).

3 CFB FURNACE

This chapter covers features and physical phenomena of a CFB furnace. The information in this chapter is used to further develop the Apros CFB model and to gain a general understanding of the CFB furnace.

First, features and vocabulary of CFBs are discussed, after which each main physical phenomenon of a CFB are discussed separately. There are three main physical phenomena in CFB units, all of which affect each other (Pallarès & Johnsson 2013, 537):

1. Fluid dynamics;
2. Reaction chemistry;
3. Heat transfer.

Figure 3.1 shows how sensitive each process is to one another, the arrow thickness indicating the sensitivity. The figure shows that fluid dynamics affects the reaction chemistry and heat transfer the most and is relatively insensitive to changes in the other two processes. Modelling fluid dynamics should therefore be done very carefully and thoroughly. Fluid dynamics, or hydrodynamics, and heat transfer are discussed thoroughly in this chapter, because they are the key areas in the current model development.

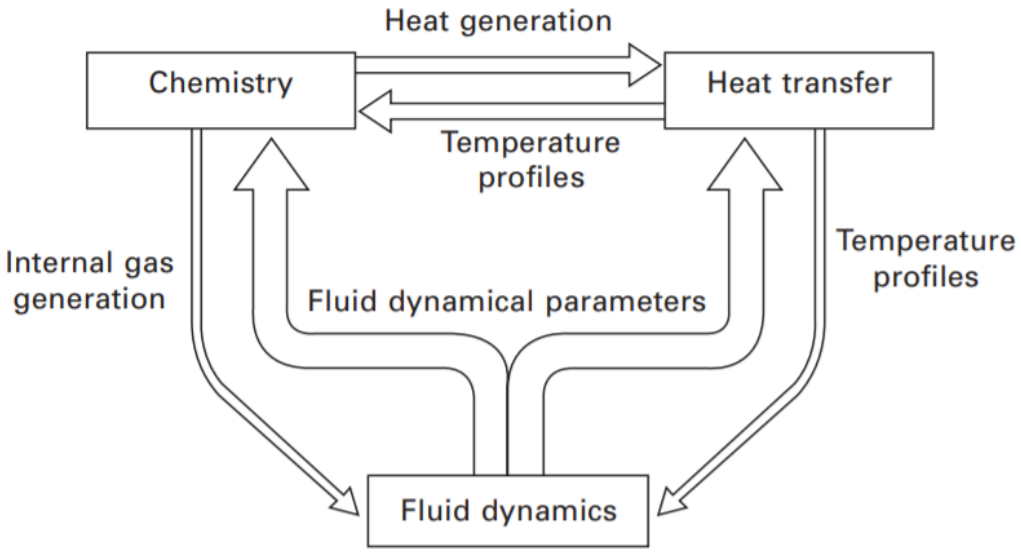

Figure 3.1. Input-output data exchange in the CFB model. The thicknesses of the arrows indicate the magnitude at which one process influences the other. (Pallarès & Johnsson 2013, 537.)

3.1 Unique Features and Vocabulary of CFBs

Figure 3.2 shows a general description of a CFB boiler and its heat exchanger surfaces. The scope of this thesis covers the primary loop, i.e. where the bed material circulates. CFBs have a riser, where solids flow generally upwards and exit it at the top. External circulation is enabled by a cyclone, a standpipe and a loopseal. Solids flow from the riser to the cyclone, where flue gas and solids are separated. Flue gas and the finest particles go to the backpass, and the separated solids flow down to the standpipe. A standpipe, also known as the return leg, is the vertical pipe after a cyclone that contains a large solids inventory. After the standpipe, there is a loopseal which is fluidized. The standpipe has a high column of solids that push the fluidized material of the loopseal back to the furnace. The loopseal prevents fluidizing air from flowing from the furnace to the standpipe.

Another two unique features in CFB boilers are wing wall heat exchangers (WWHE) and external heat exchangers (EHE), which increase the heat transfer capacity to the water/steam line. WWHEs are located inside the furnace and are thus exposed to bed material contact and high temperatures, making heat transfer efficient. They are depicted in Figure 3.2 as the additional heat exchanger pipes in the upper furnace, but they may also be the height of the entire furnace. An EHE is essentially a BFB where heat exchanger tubes are immersed, and it is located outside the furnace, after the standpipe. In the figure, the EHE is in parallel with the loopseal, but they may also be in series, in which case the EHE is located between the standpipe and the loopseal. The EHE increases fuel flexibility and load control, because it enables easier control of heat transfer in the primary loop (Basu 2015, 74). This is done by altering the mass flow of hot solids to the EHE.

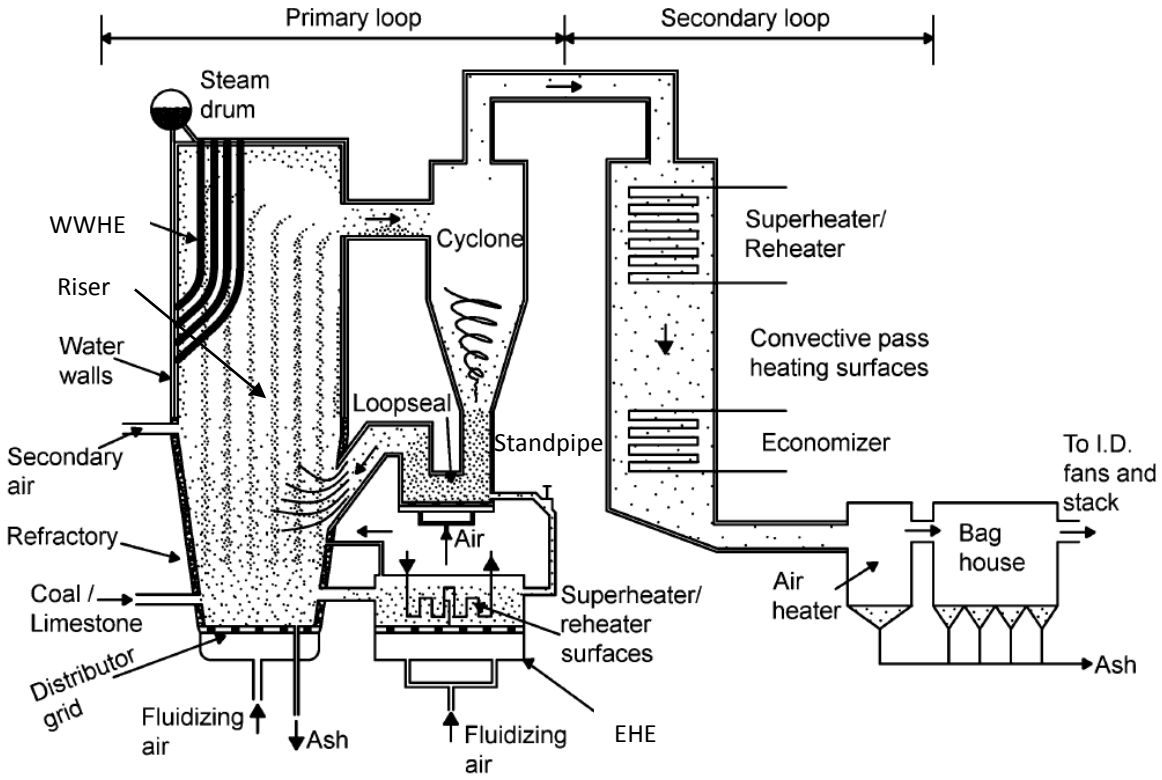

Figure 3.2. A schematic of a CFB boiler and its heat exchanger surfaces (Basu 2015, 52).

Important variables concerning fluidized beds are suspension density, solids concentration and voidage. Suspension density and solids concentration describe the weight of solids per unit volume in the furnace. They are basically synonyms, but suspension density is usually used when referring to e.g. cross-sectional averages or entire furnace zones. Solids concentration is more often used when talking about local units of volume, e.g. at the wall. Voidage tells the share of gas by volume, in a unit of volume.

3.2 Hydrodynamics

A general presentation of CFB hydrodynamics is seen in Figure 3.3. Macroscopically, gas flows vertically and, to a lesser extent, laterally inside the furnace and exits the system at the cyclone. Solids enter the bed from feed ports and from the loopseals. The gas flow drags the solids from the bottom furnace to the upper. Some of the solids travel all the way to the cyclone to be separated from the gas, but most turn to the walls and fall downwards.

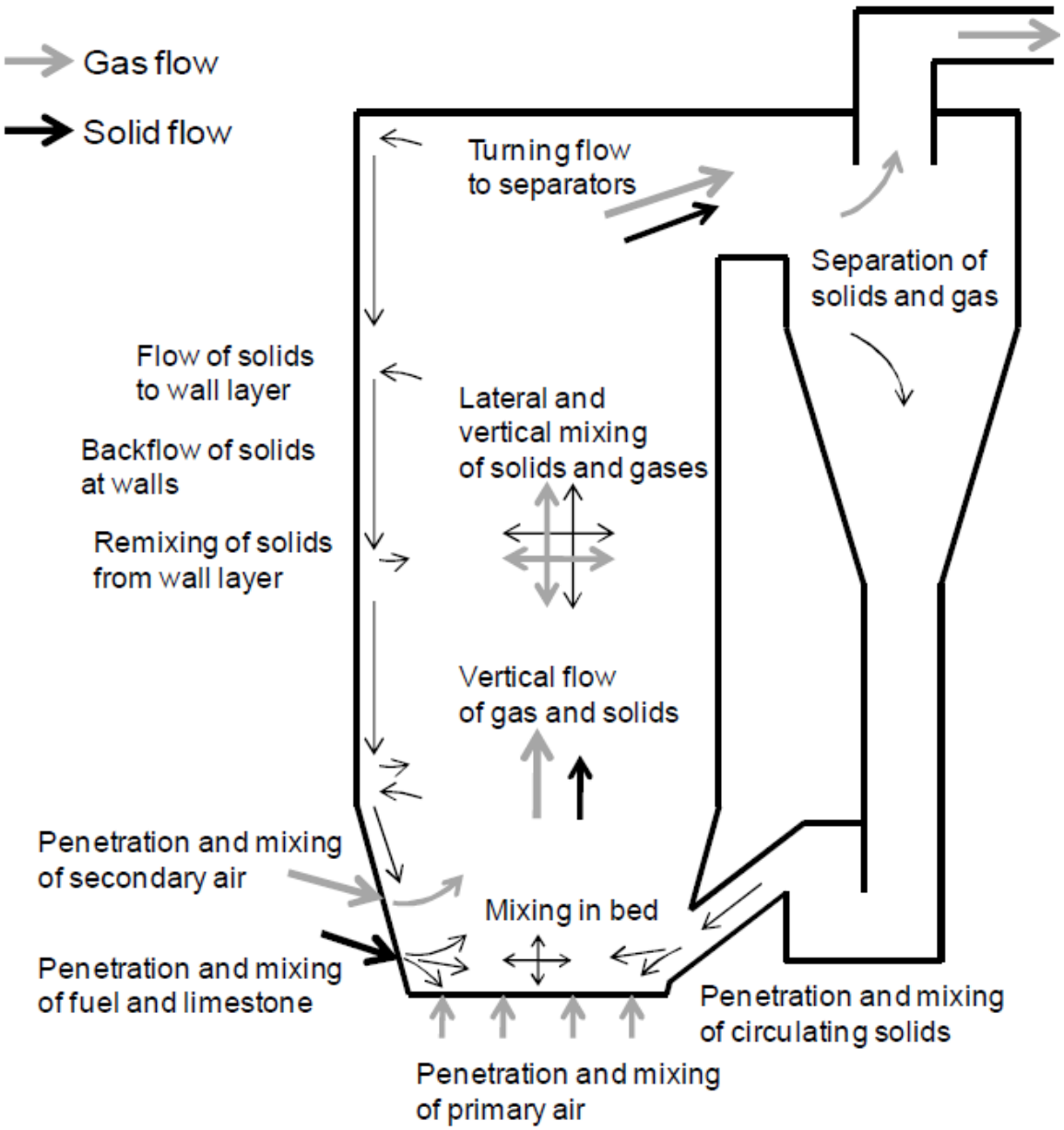

Figure 3.3. CFB hydrodynamics at a macroscopic scale (Myöhänen 2011, 37).

Figure 3.4 illustrates the CFB furnace flow mechanisms in more detail. Particles tend to form clusters (also referred to as streamers or packets) of closely-packed solids, which makes the behavior of the particles more unpredictable. Clusters may move both up or down near the furnace axis where gas velocity is higher, and down near the walls where it is smaller (Grace & Lim 2013, 154).

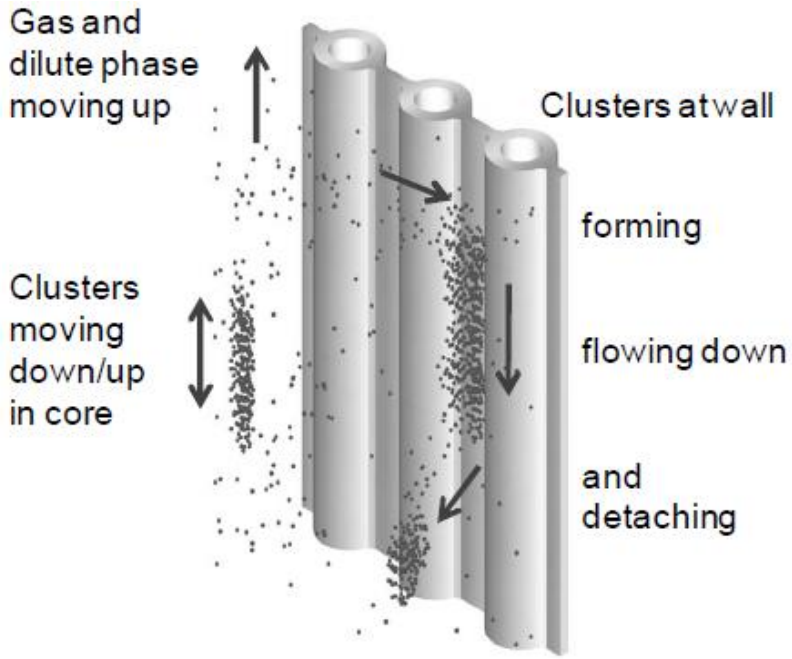

Figure 3.4. General flow mechanisms in a CFB (Myöhänen 2011, 38).

Clusters form as seen in Figure 3.5. Solids in a gas flow leave tiny wakes downstream of the flow, Figure 3.5a. When there are enough solids in the riser, a particle will enter this kind of wake, causing the fluid drag on it to decrease and the particle to drop on the trailing particle due to gravity. The upward speed of this kind of particle agglomerate is always lower than that of a single particle, as there is more mass compared to fluid drag. This makes the agglomerate slow down or fall in the riser, thus collecting more particles, Figure 3.5b. (Basu 2015, 30; 41.) The downward speed of the particle cluster is, however, higher than that of a single particle near the walls, where clusters may fall with the speed of 2…8 m/s, depending on bed material and furnace conditions (Blaszczuk & Nowak 2015, 466).

Clusters tend to form shapes of least drag and they are therefore roughly ellipsoid-shaped (Basu 2015, 41). They may travel down even for several meters before dissolving into the gas stream. Clusters can form anywhere in the CFB furnace, but most of them are formed near the walls where there is a higher concentration of particles. (Grace & Lim 2013, 154.) The cluster-forming rate decreases when there are less solids and when the solids are coarser (Basu 2015, 41).

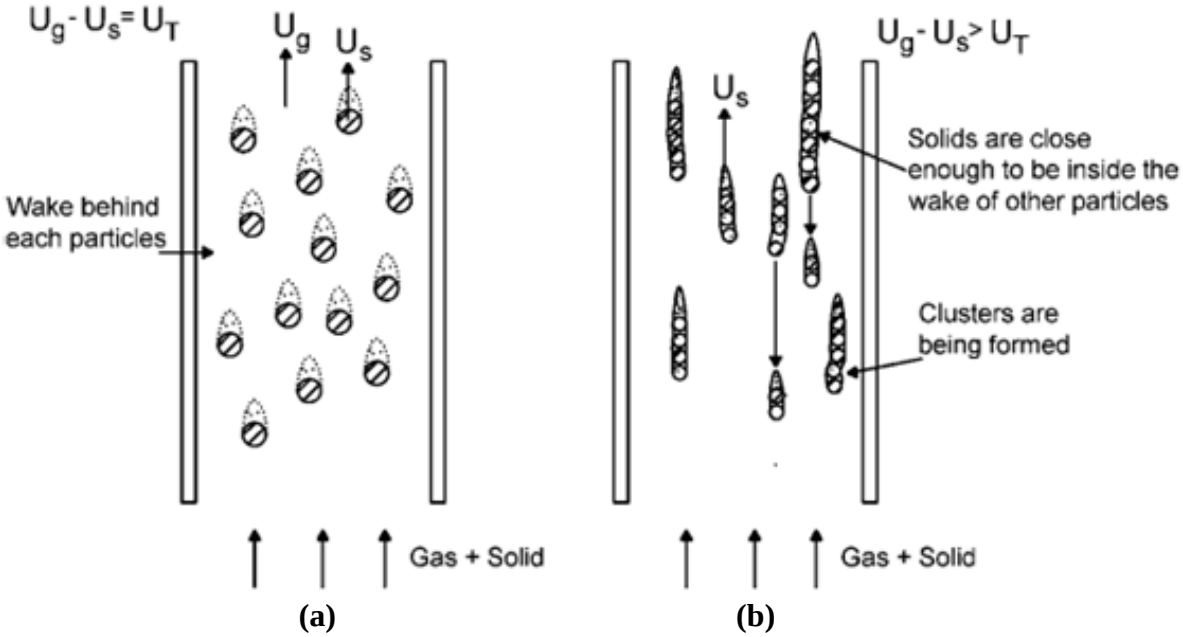

Figure 3.5. Formation of clusters: a) low concentration of solids flowing freely in the riser; b) increase in solids feed causes particles to form clusters and the regime of fluidization to shift to fast fluidization (Basu 2015, 31).

Another important factor affecting CFB hydrodynamics over a longer timespan is attrition. Attrition is the phenomenon where particles gradually degrade due to interparticle forces, i.e. solids colliding with other solids, and bed-to-wall impacts. This results in bed material slowly becoming finer which may lead to problems. Finer bed material is entrained more easily and they are more difficult to keep inside the system, meaning that more particles escape the cyclone with flue gas. An increased amount of particles in the flue gas means that the filter systems have to be larger. Attrition also leads to losses in bed material, unburnt fuel and sorbent, which causes a decrease in combustion and sulphur retention efficiencies. The increased duty of filters, increase in bed make up material, fuel and sorbent use, and the decreased efficiencies may become expensive. (Werther & Reppenhagen 2003, 201.) Furthermore, an increased amount of fines in the bed lowers the mean particle size, influencing bed hydrodynamics. Depending on the bed material, this can have a major effect on fluidizing conditions and therefore has to usually be accounted for.

3.2.1 Axial Distribution of Particles in the Furnace

Figure 3.6 illustrates a typical suspension density distribution as a function of furnace height in a CFB. The average suspension density is high in the bottom bed and it drops dramatically after it. If the riser is high enough, suspension density will converge to a specific value, determined by the furnace and bed conditions, among other variables (Basu 2015, 37). Usually however, suspension density rises at the top because of particles hitting the furnace ceiling and decelerating, increasing their inventory there (Hannes 1996, 40–41).

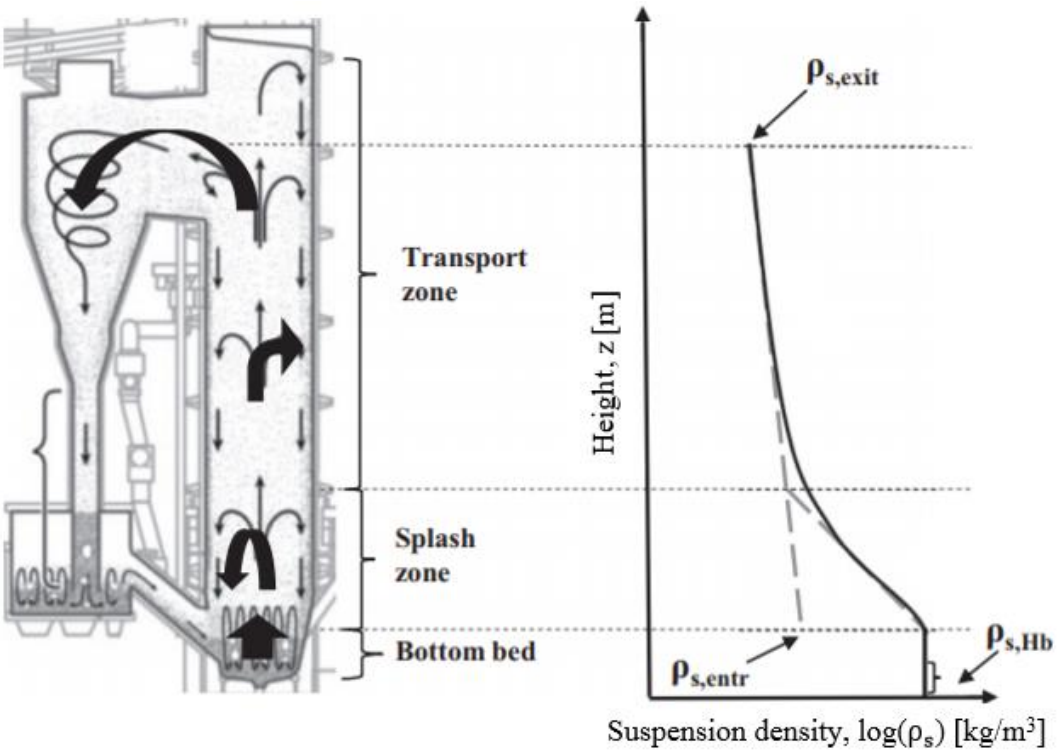

Figure 3.6. Axial profile of cross-sectional average suspension density in the different axial zones of the CFB (Djerf et al. 2018, 114).

As shown in Figure 3.6, the CFB furnace can be divided into three zones on top of each another:

1. bottom bed;
2. splash zone;
3. upper dilute zone, or transport zone.

The bottom bed consists of a two-phase flow, where the bed material is fluidized by a portion of the air and the rest of the air flows in bubble-like voids. The former is called the emulsion

phase and the latter is called the bubble phase. (Pallarès & Johnsson 2006, 545.) The vigorous movement of solids and gas allows good mixing in the bottom bed. The bottom bed has a generally uniform time-averaged solids concentration. (Johansson et al. 2007, 561–562.)

The splash zone, at the lower part of the riser, experiences a rapid decrease in time-averaged solids concentration with increasing height. This is caused by solids falling back to the bottom bed after having first been thrown upwards by gas voids. The transport zone experiences only a mild, gradual decrease in solids concentration. (Johansson et al. 2007, 561–562.) Brereton and Grace (1993, 2569–2571) found that clusters are more pronounced lower in the riser and a more dilute core-annulus flow dominates higher in the riser. The core-annulus flow is explained in the next sub-chapter. Consequently, the splash zone is characterized by strong back-mixing of solids due to the vigorous movement of solid clusters, whereas in the transport zone, back-mixing is less-pronounced with solids falling downward mainly near the wall (Djerf et al. 2018, 113).

3.2.2 **Radial Distribution of Particles in the Furnace**

From a macroscopic viewpoint, the fluidizing gas moves upwards in the furnace with a certain velocity. However, gas in direct contact with a wall has a velocity of zero. Therefore, the wall creates a boundary layer in which the gas velocity is less than in the core of the furnace. The decreased velocity means less drag on particles and so at some distance from the wall, the weight of the particles outweigh the drag, making the particles fall downwards. This creates a boundary layer for the annulus region, and inside the annulus region, solids fall down. The CFB riser can therefore be divided into two different regions in radial direction: the core and annulus region (Basu 2015, 41). In the core region particles move upward, and in the annulus region particles move downward. The core and annulus regions are shown qualitatively in Figure 3.7.

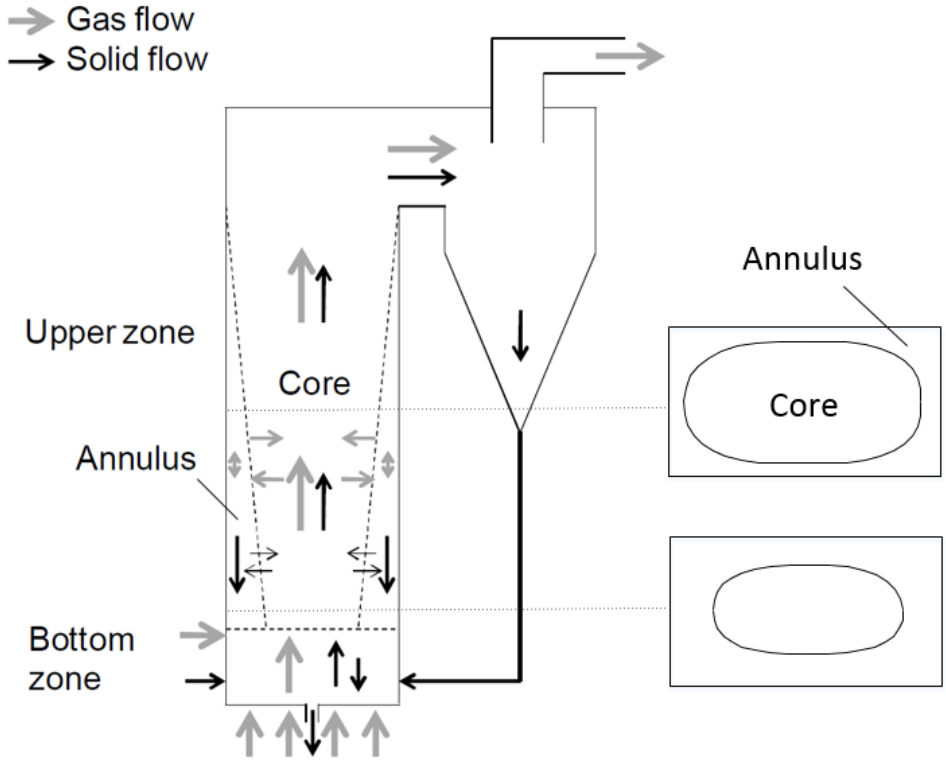

Figure 3.7. A characteristic presentation of the core and annulus regions in a CFB furnace. Modified from the reference (Myöhänen 2011, 34).

The size of the annulus region depends on the size of the riser. In commercial CFB units of 12…250 MW_e, the thickness of wall layers can be in the range of 70…350 mm, whereas in small laboratory units they can be just a few millimeters (Johansson et al. 2007, 566). The equation below for wall layer thickness in a rectangular riser was presented by Johansson et al. (2007, 571). It agrees well with data from very large operating CFB boilers (Grace & Lim 2013, 162).

$$\delta(z) = D_{eq}\left(0.008 + 4.52\left(1 - \varepsilon_{\text{avg}}(z)\right)\right), \tag{3.1}$$

where δ average wall layer thickness [m],

D_{eq} equivalent diameter of´the riser [m],

$\varepsilon_{\text{avg}}(z)$ cross-sectional average voidage at height z [-].

Equation (3.1) is defined for voidages 0.988…1. Therefore, it cannot be used for the entire furnace, only for the upper parts.

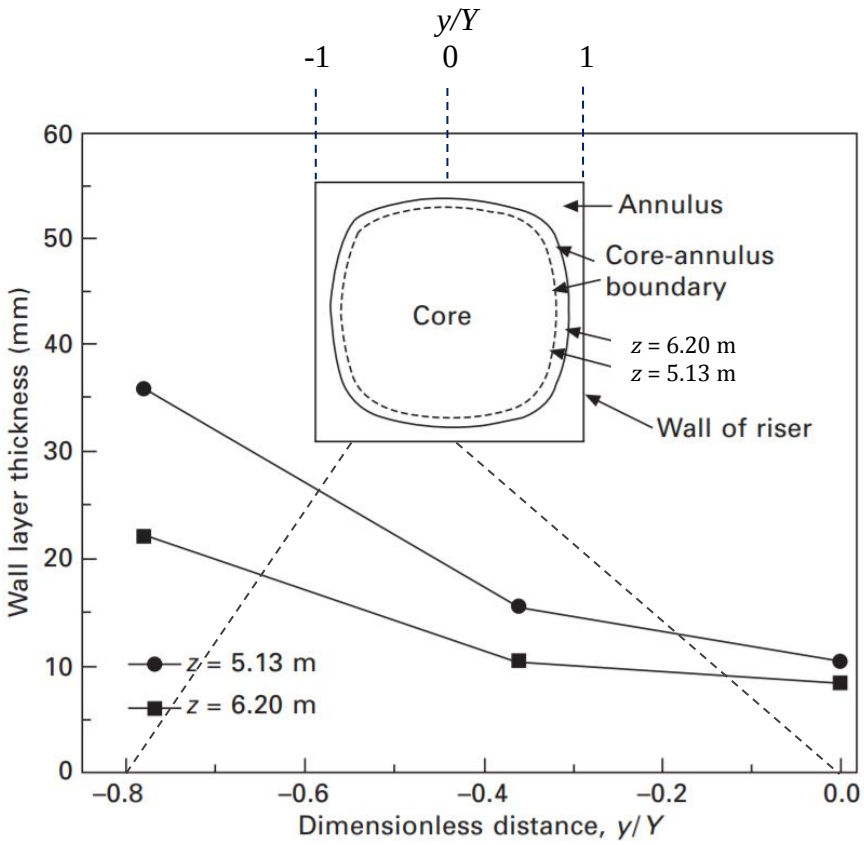

Figure 3.8. Wall layer thickness and annulus region of a rectangular riser. $y/Y = 0$ means the center of the wall and $y/Y = -1$ means the corner, Y being one half of the wall length and y varying from 0 to $-Y$. The dashed straight lines are used to clarify this. The cross-section of the riser was 146 mm x 146 mm. Modified from the reference (Zhou et al. 1995, 242).

Figure 3.9 presents a schematic of local voidage in radial direction. The figure shows that voidage is smaller near the walls than at the center of the furnace, meaning that the bed material density is bigger at the walls. With an increase in axial height, the difference in voidage is mitigated. This is in agreement with Figure 3.8 and Eq. (3.1) where it is shown that the annulus boundary layer becomes smaller with increased axial height.

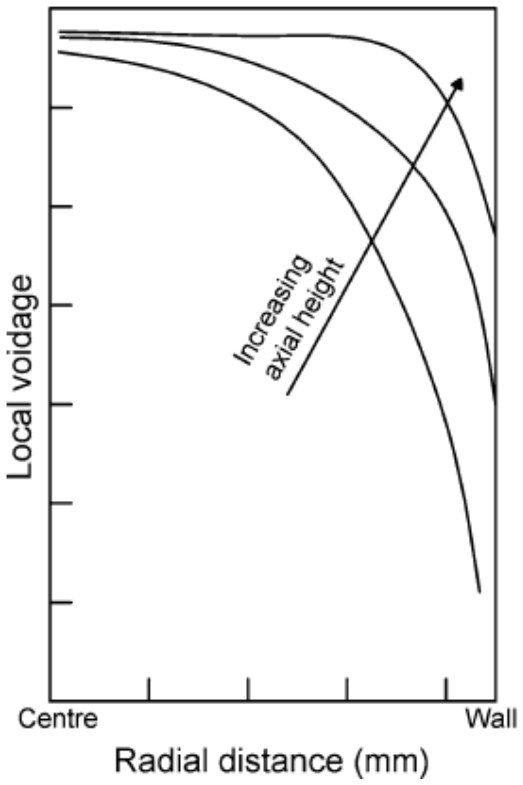

Figure 3.9. Voidage across the radius of the bed (Basu 2015, 43).

3.3 Combustion

Combustion of solid fuels can be divided into four stages: (Myöhänen 2011, 41)

1. heating up,
2. drying,
3. devolatilization/pyrolysis,
4. char combustion.

The elapsed time within these stages and the corresponding particle temperatures are presented in Figure 3.10.

In a CFB, particles normally heat up fast because of their small size and the large heat transfer rates in the bed. As particles heat up, water molecules encapsulated in the particles vaporize and escape them and the particles begin to dry. This may result in substantial particle shrinkage, especially with wet particles. Drying allows the particle to heat up, and at 400…700 °C, volatile substances, being mainly hydrocarbons, vaporize and start escaping the particle. If the volatiles cannot escape the particle fast enough, its inner pressure rises,

causing the particle to break (Oka 2004, 214). Volatiles burn in a flame outside of the particle or at its surface. When all volatiles are released, mostly carbon and ash remain. The remaining char particle burns slowly without a flame, and after the process only ash and sometimes unburnt char remain. (Scala et al. 2013, 325–327; Saastamoinen 1995, 139–154.)

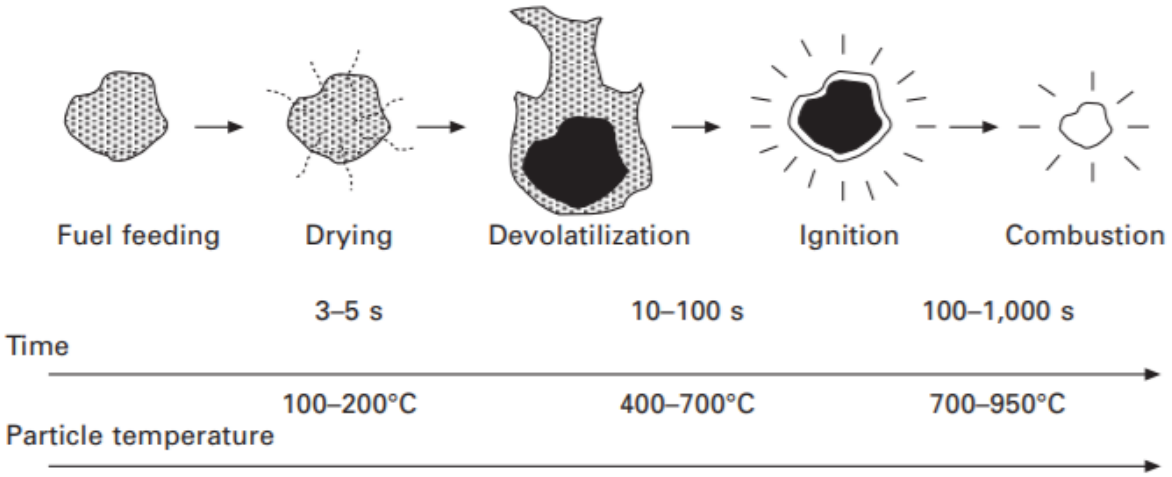

Figure 3.10. Stages of combustion of solid fuels (Scala et al. 2013, 326).

The secondary air port divides the CFB furnace into two zones from the combustion standpoint: the lower and upper zone. The lower zone is fluidized with primary air, making up 40–80 % of the stoichiometric air amount needed for combustion. (Basu 2015, 106–107.) As the fuel is fed into the lower zone, this means that much of the pyrolysis and char combustion in the zone occurs with a deficiency in oxygen. In addition, a substantial amount of the oxygen bypasses combustible matter as bubbles or gas voids. A large portion of the volatiles released in the lower zone are burned with secondary air at the upper zone. (Oka 2004, 213–214.)

The upper zone of the CFB, where most of a particle's char combustion occurs, is rich in oxygen. This is helped by the upper zone being significantly taller than the lower zone, increasing the residence time of particles alongside of internal circulation. More accurately, inside the upper zone, the core zone is oxygen-rich whereas the annulus zone is not. (Basu 2015, 114.) In the annulus zone, solids concentration, and therefore fuel concentration, is bigger and air flow is less pronounced than in the core zone, meaning that the annulus zone is more depleted in oxygen. The oxygen concentration difference is most pronounced lower in the furnace and declines with increasing height (Ibid).

3.4 Heat Transfer

This subchapter presents different heat transfer phenomena inside the CFB furnace. Heat transfer between core and annulus, bed material and wall as well as solids and gas are discussed. The most important of these is heat transfer to the water walls which is a very complex phenomenon. There are multiple modes of heat transfer and they are all affected by a number of factors. These factors include primary and secondary airflow, solids circulation, solids inventory, particle size distribution and temperature distribution (Basu 2015, 60). All of these are again affected by furnace geometry. In addition to the water walls, furnace components where heat can be extracted to the water/steam line include WWHEs, the cyclone, EHEs, superheaters before the cyclone and the furnace grid, but these are not discussed in this work.

3.4.1 Heat Transfer Between Core and Annulus

In a CFB furnace, hot solid clusters are constantly formed and broken up. The clusters, as well as individual particles, move axially and radially and this movement of solids, called the internal circulation, transports heat from the hot core to the colder annulus. Turbulent movement of flue gas also plays a part in flattening temperature gradients between the core and annulus regions. Additionally, radiation from gas and solids transfer heat from core to annulus. Radiation is more pronounced in the more dilute upper furnace, where beams can travel more freely for longer distances (Myöhänen 2011, 46–47). These phenomena make the furnace well-mixed and makes the axial temperature profile of the CFB relatively uniform. The moderately uniform temperature profile improves heat transfer to the walls.

3.4.2 Heat Transfer Between Bed Material and Wall

Solids in the CFB furnace move in two phases: dilute phase and cluster phase. The dilute phase consists of sparsely dispersed particles and the cluster phase consists of particle clusters. Generally speaking, the bulk of the solids move upward in the core in the dilute phase and the rest flow down in the annulus in the cluster phase. (Basu 2015, 57.) The dilute phase is less pronounced in the annulus and, conversely, the cluster phase is less pronounced in the core. The two phases are important regarding heat transfer to the water walls.

Figure 3.11 illustrates the principle heat transfer modes to the water walls. Heat transfer occurs through particle convection (PC) from the upflowing dilute phase, downflowing cluster phase, convection from flue gases and also radiation from solids and gas (Basu 2015, 57; Myöhänen 2011, 46). Convection from particles is basically conduction to the wall from the solids flow that is in contact with it. Therefore, this phenomenon is often called "particle conduction" in literature. However, the term convection is used, because there is a constant flow of solids along the walls and it describes the phenomenon better.

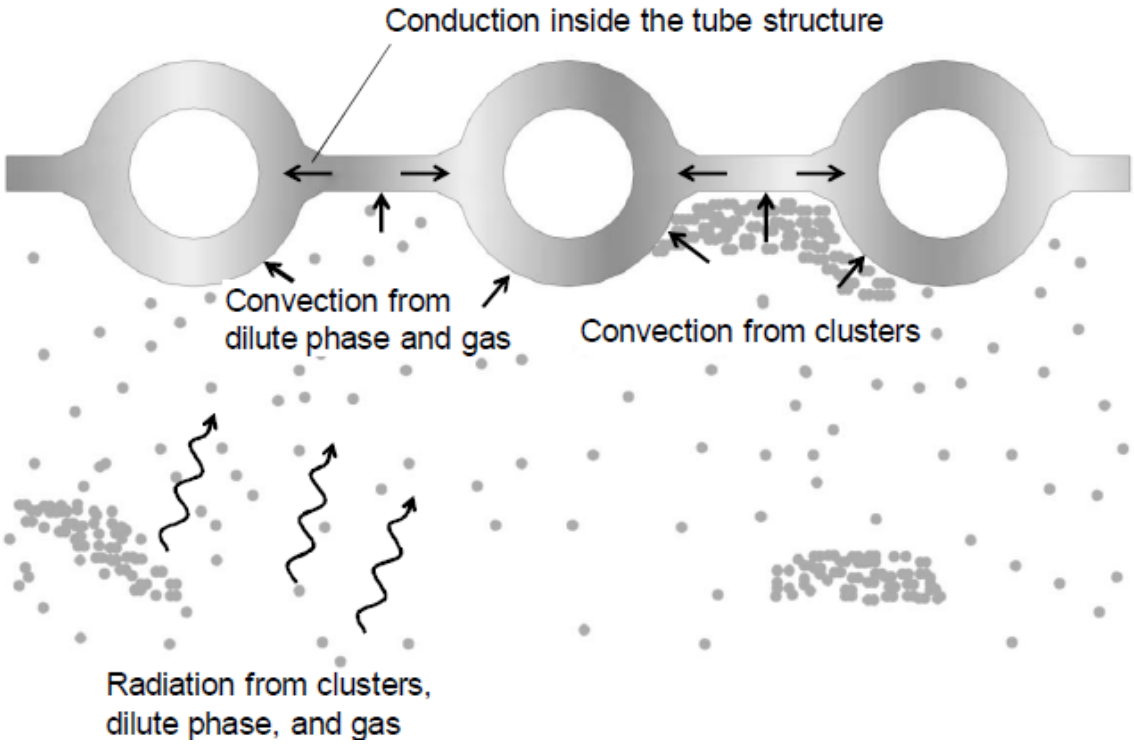

Figure 3.11. Main heat transfer methods to the water walls (Myöhänen 2011, 45).

Heat transfer by gas convection can be usually considered insignificant compared to other modes, at least at higher boiler loads (Myöhänen 2011, 46). This is supported by the observation that increasing fluidizing gas velocity has little effect on the total heat transfer coefficient (HTC), as long as vertical suspension density profiles remain similar (Basu 2015, 60). Consequently, radiation and PC are the most important heat transfer modes in a CFB.

PC from the cluster phase is much more intense than PC from the dispersed phase. When the bed is denser, i.e. lower in the furnace, clusters cover a larger portion of the wall than higher in the furnace where the bed is leaner, resulting in a larger HTC in the lower parts.

Due to the transient nature of clusters, the local value of time-average suspension density on the wall is the most significant factor that influences heat transfer from bed to wall in a fast bed. (Basu 2015, 58–61.)

Radiation is more intense in the upper furnace than in the lower. The population of particle clusters is higher in the lower furnace and they shield radiation from the core from hitting the walls. In addition, the clusters flowing near the water walls are cooled by the walls, resulting in smaller amounts of radiation from the clusters. (Myöhänen 2011, 46–47.) These factors contribute to PC being the dominating mode of heat transfer in the lower furnace and radiation in the upper furnace.

This is illustrated in Figure 3.12, where the dominating modes of heat transfer in different parts of the furnace at three different boiler loads are shown. Suspension density determines which mode is the most important. Lower in the furnace where suspension density is higher, particles are in contact with the walls more frequently and PC is the dominant mode of heat transfer. PC is proportional to the square root of suspension density, so its effect decreases with increasing height (Basu 2015, 82). In the upper furnace, where suspension density is small, radiation becomes the dominant mode of heat transfer. With smaller boiler loads, suspension density drops more dramatically with increasing height and thus radiation may be the dominating mode in almost the entire furnace.

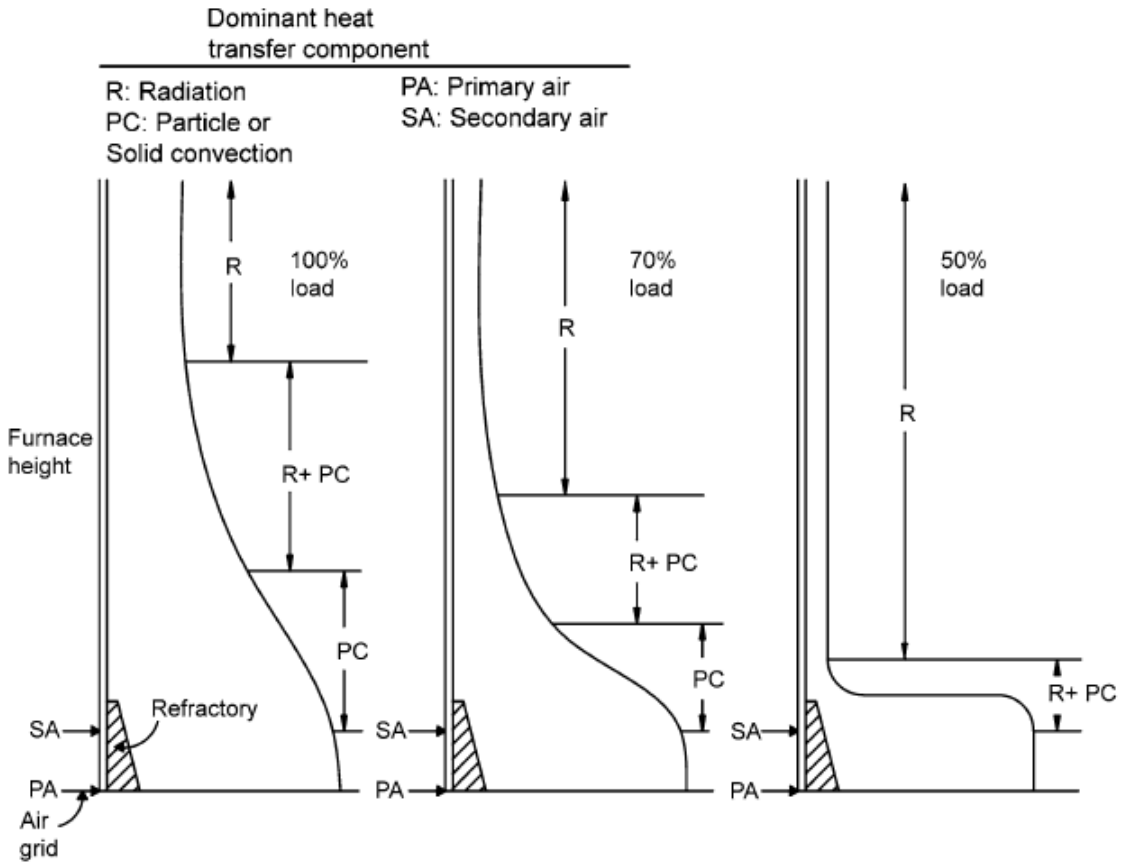

Figure 3.12. Dominant modes of heat transfer at different boiler loads. The lines depict suspension density qualitatively. (Basu 2015, 82.)

An increase in bed temperature has a positive effect on the total HTC. A higher bed temperature increases gas conductivity, positively affecting the HTC between water walls and clusters and inside the clusters. Higher bed temperatures also increase radiation from bed to water walls. (Basu 2015, 62.) Higher bed temperatures, so by and large over 900 °C, are however not desirable due to issues with emission control and agglomeration (Basu 2015, 115).

Solving the total HTC usually revolves around solving convection and radiation from the cluster and dilute phases and the time-average value of the fraction of the wall covered by clusters. This is called the cluster-renewal model and it has been researched by several authors (Blaszczuk & Nowak 2015; Dutta & Basu 2004; Ryabov and Kuruchkin 1991). It is expressed as (Dutta & Basu 2004, 1040)

$$h_{\mathrm{tot}} = f(h_{\mathrm{con}} + h_{\mathrm{rad}})_{\mathrm{cluster}} + (1-f)(h_{\mathrm{con}} + h_{\mathrm{rad}})_{\mathrm{dilute}} \qquad (3.2)$$

where f time-average fraction of wall covered by clusters [-],
h_{con} convection HTC [W/m^2/K],
h_{rad} radiation HTC [W/m^2/K].

The calculation processes for the components in Eq. (3.2) are long, as there are circa 15 equations to be solved in total. The calculation of heat transfer for clusters is particularly arduous, where variables such as gas layer thickness, the mean distance a cluster falls along the wall, and the specific heat of the clusters need to be calculated. Figure 3.13 illustrates the formation of a cluster in the vicinity of the wall. It is formed, then it flows along the wall at a distance that is the length of the gas gap and then it is disintegrated. L_c in the figure denotes the distance that the cluster falls along the wall and f is the fraction of the wall covered by the cluster. The figure also shows the temperature profile by the wall, showing a uniform distribution at the core and increasingly large gradients in the annulus layer when moving towards the wall. The major challenge for using Eq. (3.2) is solving f in different operating conditions.

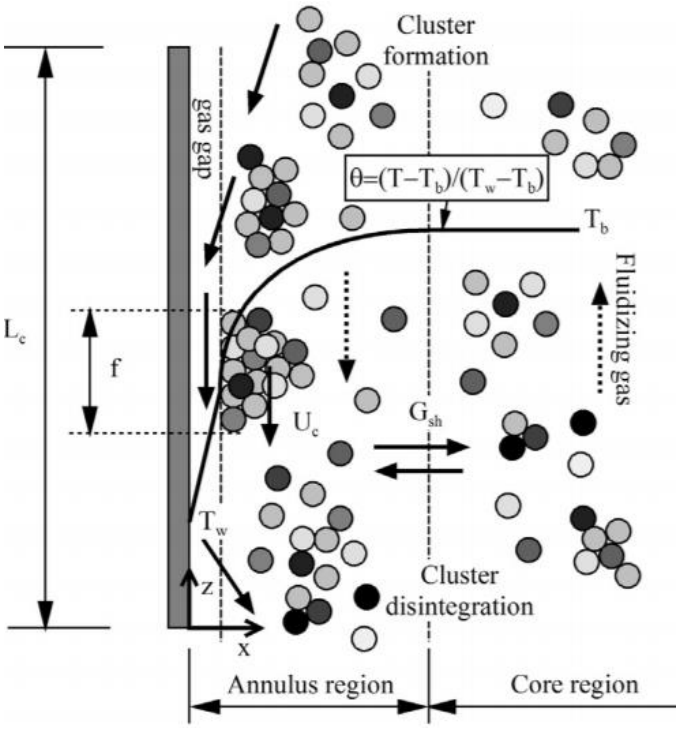

Figure 3.13. Single cluster formation, gas gap and temperature profile by the furnace walls (Blaszczuk & Nowak 2014, 738).

Referring to the objectives of this thesis, the Apros CFB model should be further developed based on this theoretical overview. The methodology for solving the HTC as presented above requires an excessive amount of data which is not available. Therefore, a simpler way to solve the HTC is needed.

Dutta and Basu (2002, 89) gathered data from a 170 MWe CFB boiler. They came to the conclusion that the total HTC on the water walls and wing walls depends mainly on the radial average of suspension density and temperature, and can be expressed as

$$h_{\text{water wall}} = C_{\text{water wall}} \cdot {\rho_{\text{avg}}}^{0.391} \cdot {T_{\text{avg}}}^{0.408} \tag{3.3}$$

$$h_{\text{wing wall}} = C_{\text{wing wall}} \cdot {\rho_{\text{avg}}}^{0.37} \cdot {T_{\text{avg}}}^{0.425}, \tag{3.4}$$

where
$C_{\text{water wall}}$ constant, 5.0 [-],
$C_{\text{wing wall}}$ constant, 3.6 [-],
ρ_{avg} average suspension density [kg/m^3],
T_{avg} average temperature [°C].

The equations were validated by Dutta and Basu (Ibid., 89–90) for several commercial CFB boilers, showing good agreement. The researchers did not, however, present exact ranges for suspension densities or temperatures within which the equations are valid. It must then only be assumed that the ranges consist of normal operating conditions of commercial boilers. For temperatures this means 800…900 °C.

These equations do not take into account the separate effects of particle convection or radiation, for instance. They are therefore less accurate compared to Eq. (3.2), but being simple, they respond better to the requirements of this thesis. Eq. (3.2) contains several variables that are not available in the Apros CFB model and it would require much further development to make the equation functional. This could be one issue for development in the future if the equation is considered necessary and if a detailed cluster formation model is available.

3.4.3 Heat Transfer Between Solids and Gas

Gas-bed heat transfer is initiated once solid particles and fluidizing gas are at different temperatures. A temperature difference between gases and solids is formed when primary and secondary air penetrate the bed, when reaction heat is released from fuel and when gas and particles are cooled by the water walls.

Heat transfer between gas and bed material is extremely efficient due to the large heat transfer area between them. A 1 m^3 packed bed of ideally spherical 100 μm particles has a combined surface area of roughly 31400 m^2. In industrial applications, where particles are not spherical and there is a particle size distribution, the surface area may be even 60 000 m^2, so almost twice as much (Di Natale & Nigro 2013, 206). Of course, in fluidized bed applications the bed is expanded, but this provides some reference to the surface area of the bed.

The dominant mode of gas-bed heat transfer is convection (Teir 2003, 163). The HTC for a unit surface of the emulsion phase is quite low, 4…25 W/m^2/K, but it is approximately a thousand times more for the unit volume of the emulsion (Di Natale & Nigro 2013, 206). Because of the efficient heat transfer, for example primary air reaches a temperature equilibrium with the bed almost instantly after the gas distributor. Because gas-bed temperature differences level out rapidly, it is often chosen not to model it with detail (Di Natale & Nigro 2013, 207). It is, however, important in some cases, for example in coal combustion, where the rate of heating of coal particles influences volatile release (Basu 2015, 53).

4 REVIEW OF DYNAMIC ONE-DIMENSIONAL MODELS FOR CFB FURNACE

This chapter deals with models used for the dynamic simulation of the CFB furnace. Because Apros is a software for 1D dynamic simulation, the emphasis will be on 1D dynamic models. More accurately, as the 1D models discussed are typically core-annulus models which have N axial and 2 radial elements, also the term 1.5D model can be used for them. The objective of this chapter is to investigate and review the modelling solutions of other models. This review can be used to further develop the Apros CFB model if suitable modelling solutions are found.

The Apros CFB model is semi-empirical. Semi-empirical models combine empirical correlations with theoretical principles to describe a process. The number of empirical correlations used varies significantly between models. The content of CFB sub-models may range from empirical expressions to transport equations. The models are typically based on solving the mass and heat balances for the discretized elements of the CFB, while momentum balances and turbulence are neglected. Generally, only the furnace is discretized, with a 1.5D or 3D grid, and other parts such as cyclones, standpipes and EHEs are modelled as 0D, so using a single calculation element only. (Pallarès & Johnsson 2013, 530.)

The gas and solid flows in the CFB riser are very complex phenomena and various mathematical models of different accuracies and mathematical formulations have been made over the years. The riser is the most important component of the CFB and the majority of modelling effort usually goes to modelling it. (Huang 2006, 37.) Complex, specific and relatively accurate 3D models require lots of work and calculation power as opposed to more simple and less accurate 1D models. Therefore, it is often important to find a solution that gives sufficiently accurate results without requiring massive computational power. These riser models can be roughly divided into three groups (Ibid.):

1. Models that predict variations of properties in axial direction, but not radial;
2. Models that predict the variations also in radial direction by considering two or more regions in radial direction, such as core-annulus or clustering annular flow models;
3. Models that employ the governing equations of fluid dynamics in order to predict the two-phase flow of gas and solids. These are 2D or 3D computational fluid dynamics (CFD) models.

One possible approach is also zero-dimensional, where the riser may be divided into just one or two blocks.

This chapter will focus on the second group in the previous list, as purely 1D dynamic models were not found. Unfortunately, there are not many dynamic 1.5D models of a CFB riser that are accessible and that are comprehensive, so only few were found that fulfilled the requirements. Models belonging to the third group are usually used for research purposes only, since they require too much measurement data and computational power to be effectively used in a general simulation software.

4.1 Riser Hydrodynamics

The most used approach for the dynamic modelling of the CFB furnace is the core-annulus, or 1.5D approach. The major advantage of the 1.5D approach against a pure 1D or 0D approach is that it allows back-mixing in the model and therefore a more realistic temperature profile can be achieved, for instance.

Table 4.1 presents modelling solutions of different dynamic 1.5D CFB models and the sizes of the CFBs used to validate results. Most of the authors validated their results with small CFBs. Three models out of five modelled the bottom bed with a discretized bubble-emulsion phase. It is quite analogous with the core-annulus zone with solids moving up in the bubble phase and down in the emulsion phase, allowing back-mixing. Four models modelled particle size distribution (PSD). This was done by dividing particles into several size classes, each having an average size. All models that covered PSD considered also attrition which is an important modelling parameter. Annulus thickness was calculated in almost every model. Most of the models used calculated parameters, split coefficients, to determine mass flows from core elements to the annulus as opposed to universal constants. Gungor (2009)

calculated the parameter using terminal and superficial velocities, while Chen & Xiaolong (2006) used solids concentrations, but did not present the equation used.

The modelling solutions provided in the references of Table 4.1 will not be applied in the Apros CFB model at this point. However, this table is useful in future development as it helps find references for different advanced modelling solutions.

Table 4.1. Important modelling principles of different dynamic CFB models.

Authors	Kim et al. 2016	Kovacs et al. 2012	Gungor 2009	Gungor & Eskin 2007	Chen & Xiaolong 2006
Validation CFB	300 MWe	pilot-scale	pilot-scale	pilot-scale	410 t/h Pyroflow
Bubble-emulsion phase at bottom bed	yes	no	yes	yes	no
PSD	yes	no	yes	yes	yes
Attrition	yes	no	yes	yes	yes
Annulus thickness	yes	yes	yes	yes	no
Global split coefficient used	NA	yes	no	no	no

4.2 Riser Heat Transfer

CFB riser heat transfer is a very complex phenomenon and there are many approaches with varying complexity and accuracy to model it. In the articles presented in Table 4.1, the authors cover heat transfer only briefly, most of them giving only citations to references containing the equations. Only Gungor (2009) presents the equations of the model thoroughly. Whether the models follow the equations entirely, or if some simplifications were made, is not addressed.

At least three of the five authors in Table 4.1 used a cluster or particle renewal model for modelling heat transfer. Kim et al. (2016) used a cluster renewal model suggested by Dutta & Basu (2004), Gungor (2009) used a cluster renewal model presented by Ryabov and Kuruchkin (1991) and Chen & Xiaolong (2006) used a particle renewal model given by Basu & Fraser (1991). Gungor (2009) and Chen & Xiaolong (2006) also used a separate heat transfer correlation for the bed bottom, given by Basu & Nag (1996). Kovacs et al. (2012) seemed to account only for heat transfer from the gas and Gungor & Eskin (2007) did not present their approach for modelling heat transfer.

4.3 Other CFB Process Parts

Important CFB parts besides the riser include WWHE, cyclone, standpipe, loopseal and EHE. There may also be external fluidized beds with heat exchangers that are a part of the solids returning system. Among the references presented in Table 4.1, the modelling of the other CFB parts is covered poorly.

Kim et al. (2016) and Chen & Xiaolong (2006) modelled the cyclone and standpipe with one element and the former modelled also the loopseal. The two models were quite comprehensive, assumably providing good simulation results. Comprehensive information on e.g. heat transfer in the components were not given. Kim et al. only mentioned that the heat transfer coefficients were obtained by fitting operational data. Wing walls were modelled only by Kim et al. who discretized the wing walls into multiple elements, but other information was not given.

5 PRELIMINARY APROS CFB MODEL

This chapter introduces the preliminary CFB model that has been implemented to Apros. The model has been developed for some years, so much of the modelling work has already been done. Before the beginning of this thesis, the Apros CFB model was redesigned to some extent by most notably implementing the core-annulus approach in the solids balance of the model. Therefore, many of the modelling solutions presented in this chapter are not the author's contribution. The presented modelling solutions follow the CFB model specification document by Tuuri & Lappalainen (2018). The author has, however, specified the requirements specification in more detail, tested the new features after implementation and contributed to further improvements.

The modelling solutions presented in Chapter 4 are not used in the Apros CFB model. Most of the modelling solutions in literature are too complex to ever be used in the model, as Apros models have their own application profile. However, the modelling solutions presented in literature can be used as guidelines in future development.

In this chapter, dynamic simulation and the basic functionality of Apros is presented first. Then, some important modelling solutions of the old CFB model are presented. After this, a detailed overview of the new model, its features and modelling solutions is given. Finally, sensitivity analyses are done for the most crucial empirical correlations in the model.

5.1 Dynamic Simulation

There are fundamentally two types of models used in the industry: steady state and dynamic models. Steady state modelling is widely used in the industry, and it is important for process conceptualization, design and evaluation. The steady state is, however, an idealistic definition, usually representing the design conditions. It does not capture e.g. changes in capacity or the inherent dynamic behaviour of a system. (da Silva, 2015). Dynamic models on the other hand provide time-dependent simulation results. With a dynamic model, the user can change a value in the model and see its consequences by monitoring or logging results at each time step. The dynamic model can be guided from one steady state to another,

making the application scope of dynamic simulation much wider than the scope of steady state simulation. This is depicted in Figure 5.1.

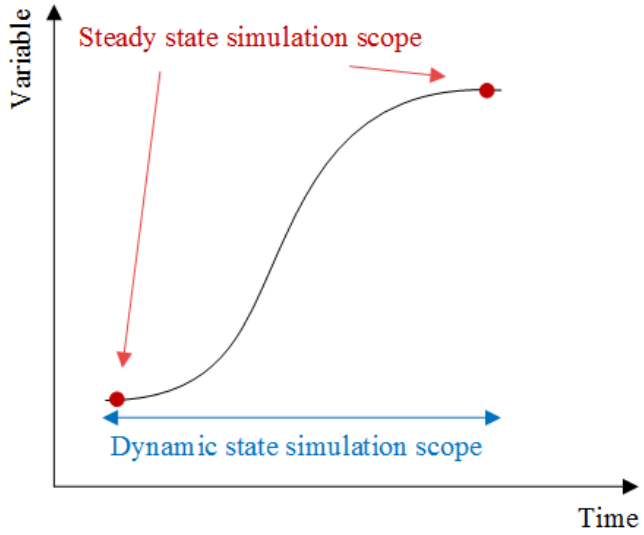

Figure 5.1. Comparison of dynamic and steady state modelling scopes. Adapted from reference (da Silva, 2015).

The most important uses of large-scale dynamic process simulation are as follows (Lappalainen et al. 2012, 65).

- Development of control strategies. The simulator is used as a test bench for control development.
- Analysis of the system operation. For example "what-if experiments" that are not possible in the real plant, can be conducted. Different transients, such as load changes or accidents can be studied with detail and the model can be used for making the real process and practices better.
- Verification of design.
- Testing of control system.
- Training of operators. Simulation training is an advantageous tool to ensure the safe operation of the plant in all situations and to speed up the start-up curve of a new plant.
- Development of operational practices and the control room. A simulator can be used to develop a control room so that the operator has the right information at hand at the right time, improving plant safety and economy.

5.2 Apros Simulation Software

Apros® is a dynamic process simulation software developed jointly by Fortum and VTT Technical Research Centre of Finland. It is used for modelling and simulating energy

systems, power plants and networks using thermal, nuclear, automation and electrical model components through a graphical user interface. This makes it very versatile for different problems requiring dynamic simulation.

Figure 5.2 shows the hierarchical structure of Apros models. The user manages a model with diagrams which are interconnected with connection flags. Each diagram consists of a separate subsystem such as a CFB boiler, steam generation or drum level automation. The diagrams are configured with process, automation or electrical component models that are dragged to diagrams from model libraries, and with so-called user components that are made by the user, using other components and programming. Each process component model generates a calculation level structure that comprises branches and nodes, at its simplest. Apros uses a staggered grid in thermal hydraulic model nodalisation, so mass and energy control volumes and momentum control volumes are not the same. In Apros calculation level this means that branches are connected to nodes and vice versa; momentum is calculated in the branches while mass, energy and fluid composition are calculated in the nodes.

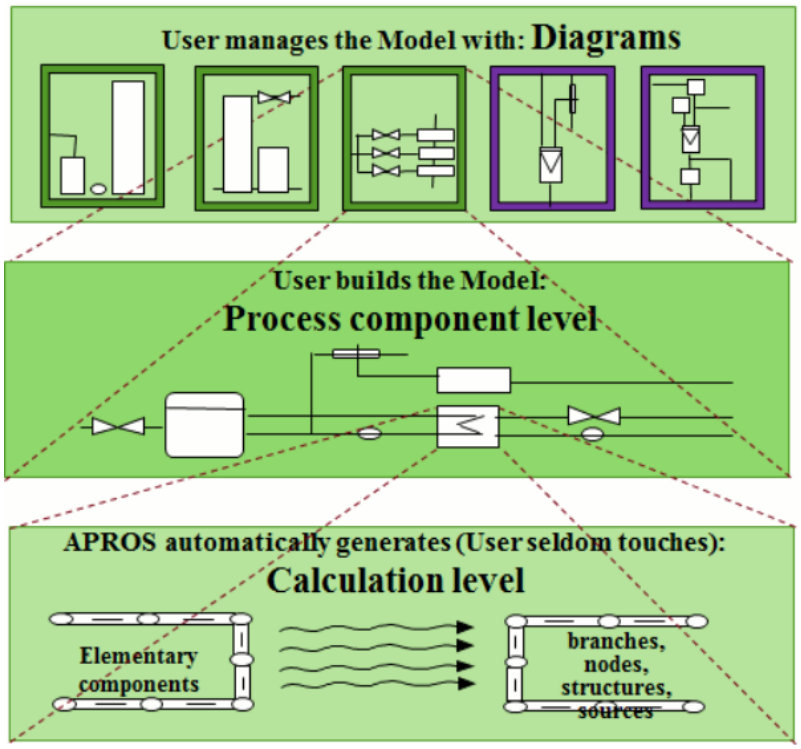

Figure 5.2. Hierarchical structure of Apros models (Apros 2018).

While building the model, key configuration values such as dimensions and pump nominal heads are given to process components. Boundary conditions are defined by excluding model components from simulation which means that their values remain constant. An example of an excluded component is a point which determines the thermodynamic properties of air. When simulation is started, Apros Solver implicitly solves differential and algebraic equations for thermodynamic variables, at each time step. Apros Solver uses the default and user given values at the first time step, previous calculation results thereafter and boundary conditions. (Fortum & VTT 2017, 13.)

Charts can be drawn for any property, showing simulated variables as trends at each time step or at desired intervals. The operation values of the model can be changed during simulation, so it is possible to graphically display how a drum level set point change plays out, for instance. It is also possible to draw property distributions at each time step. This can be, for example, steam pressure and temperature along a steam line. The simulation results can be exported to files and used in further analysis. Data can be also imported from files and used as simulation input values.

A momentary simulation state of the model can be saved as an initial condition. There can be multiple initial conditions for the same model configuration. This is beneficial, as it enables quick model initialization for different important system conditions. It is possible to have initial conditions e.g. for a power plant at 50, 100 and 110 % loads, making comparison easy and fast.

5.3 Previous Work Regarding the Apros CFB Model

Development of the Apros fluidized bed model was started almost ten years ago, first by developing a model for BFBs and then moving on to also CFBs. Description of the CFB component's calculation is presented in the reference Lappalainen et al. 2014, see especially Supplementary Material. A more recent work of Lappalainen et al. (2017) describes the further development of the CFB model component with respect to hydrodynamics, combustion and solids external circulation.

The solid balance in the previous CFB model was purely one-dimensional, i.e. the furnace consisted of homogeneous nodes over the whole furnace cross-section. The solid balance in the furnace was calculated by using an equation-based reference for the vertical voidage profile. Heat transfer consisted of only gas convection and gas radiation.

The solid balance model could not simulate some important transients, such as the startup and shutdown of a furnace. In addition, adding material to the furnace bottom affected heavily to the upper furnace, which is unrealistic. The solid balance model, not being suitable for the required scope of operation, needed to be improved. Also, the heat transfer model imposed problems, as it did not take into account the solid phase heat transfer in a reasonable manner, so it had to be improved as well.

5.4 Selected Model Approach for the Solid Balance

The modelling approach for the solid balance of the Apros CFB model was improved before the start of this thesis. The modelling principle that was chosen is the core-annulus model, because it captures the essential features of a CFB riser. The improved model brought many desired features:

- The scope of operation was expanded, as e.g. startup and shutdown of the furnace can be simulated;
- The main issues of the previous model were fixed;
- The model allows better scalability;
- There is a relatively small amount of parameters in the model;
- The temperature distribution of the furnace became more realistic.

All of the 1D dynamic CFB models found in literature, reviewed in Chapter 4, apply the core-annulus approach, further implying that the approach is a good modelling solution. Furthermore, should the model be improved in the future, the core-annulus model provides a good structure for further development.

5.5 Solid Balance in the CFB Furnace

Figure 5.3 illustrates the structure of the solid balance in the CFB component. In the furnace, solids are divided into core and annulus nodes that are in pairs. The volumes of a core-

annulus pair sum up to the volume of the corresponding gas node, depicted in the figure with the dashed rectangles. Although the solid phase has two nodes in radial direction, the gas phase has only one. The only node where there is not a core-annulus pair is the bottom node, i.e. the high-density bed, which consists of only one node. In other words, the high-density bed is modelled using a single ideally mixed and homogenous calculation node. This is because, as seen in Figure 3.6, the high-density bed has a quite uniform solids concentration and it is relatively well-mixed. On top of the bottom node, there is an interface layer. It describes the density on the high-density bed upper surface and significantly affects the mass flow going to the upper furnace.

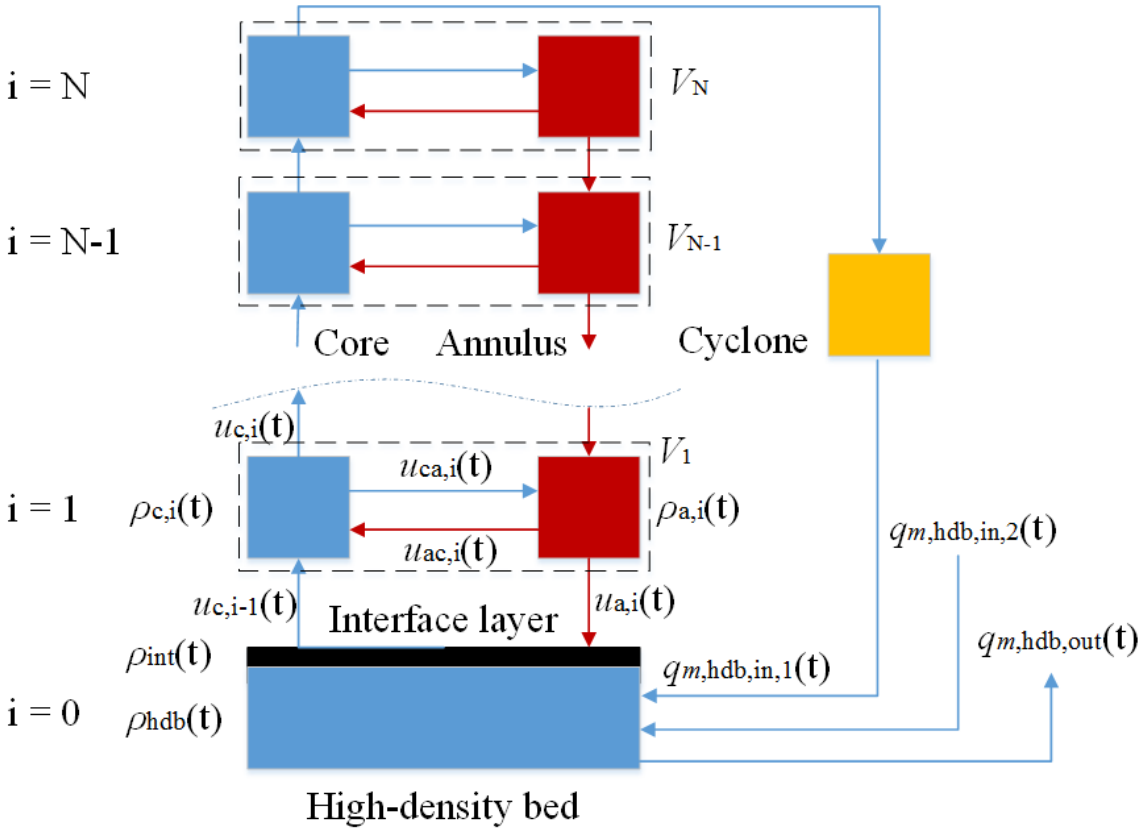

Figure 5.3. Illustration of the core-annulus model structure in Apros.

The core-annulus pairs are used for modelling the solids balance of the furnace above the high-density bed. There can be any number of these pairs between 1 and 99. Solids are extracted from the top core node to the cyclone. From the cyclone and other external solids circulation components, the solids return back to the bottom node. The external solids circulation system will be discussed later.

5.5.1 **Riser**

In Figure 5.3, solids flow upward through the series of core nodes and downward through the annulus nodes. Some solids also flow from the core to the annulus, and they can also flow from the annulus back to the core. The volumes of core or annulus zones are not included in this modelling solution. The densities of core and annulus nodes are calculated as masses in proportion to the gas node volume. This means that the average suspension density of a node is

$$\rho_{\mathrm{i}}(t) = \frac{m_{\mathrm{c,i}}(t)+m_{\mathrm{a,i}}(t)}{V_{\mathrm{i}}} = \frac{m_{\mathrm{c,i}}(t)}{V_{\mathrm{i}}} + \frac{m_{\mathrm{a,i}}(t)}{V_{\mathrm{i}}} = \rho_{\mathrm{c,i}}(t) + \rho_{\mathrm{a,i}}(t) \qquad (5.1)$$

where
$m_{\mathrm{c,i}}$ solids mass of core node i [kg],
$m_{\mathrm{a,i}}$ mass of annulus node i [kg],
V_{i} volume of gas node i [kg/ m^3],
$\rho_{\mathrm{c,i}}$ density of core i [kg/m^3],
$\rho_{\mathrm{a,i}}$ density of annulus i [kg/m^3].

It was chosen that the solids mass balance is calculated with densities as opposed to masses, to provide a better means for comparing different CFB units. Below, the mass balance of a core and an annulus node are introduced.

$$\frac{d\rho_{\mathrm{c,i}}(t)}{dt} V_{\mathrm{i}} = \dot{m}_{\mathrm{c,i-1}}(t) - \dot{m}_{\mathrm{c,i}}(t) + \dot{m}_{\mathrm{ac,i}}(t) - \dot{m}_{\mathrm{ca,i}}(t) \qquad (5.2)$$

$$\frac{d\rho_{\mathrm{a,i}}(t)}{dt} V_{\mathrm{i}} = \dot{m}_{\mathrm{a,i+1}}(t) - \dot{m}_{\mathrm{a,i}}(t) - \dot{m}_{\mathrm{ac,i}}(t) + \dot{m}_{\mathrm{ca,i}}(t) \qquad (5.3)$$

where
V_{i} volume of node i [m^3],
$\dot{m}_{\mathrm{c,i-1}}$ mass flow to core i [kg/s],
$\dot{m}_{\mathrm{c,i}}$ mass flow to core i+1 [kg/s],
$\dot{m}_{\mathrm{ac,i}}$ mass flow from annulus i to core i [kg/s],
$\dot{m}_{\mathrm{ca,i}}$ mass flow from core i to annulus i [kg/s],
$\dot{m}_{\mathrm{a,i+1}}$ mass flow to annulus i [kg/s],
$\dot{m}_{\mathrm{a,i}}$ mass flow to annulus i-1 [kg/s].

The mass flows leaving the core node in Eq. (5.2) are calculated as

$$\dot{m}_{\mathrm{c,i}}(t) = (1 - \alpha_{\mathrm{i}}) \cdot A_{\mathrm{i}} \cdot u_{\mathrm{c,i}}(t) \cdot \rho_{\mathrm{c,i}}(t) \quad (5.4)$$

$$\dot{m}_{\mathrm{ca,i}}(t) = \alpha_{\mathrm{i}} \cdot A_{\mathrm{i}} \cdot u_{\mathrm{ca,i}}(t) \cdot \rho_{\mathrm{c,i}}(t) \quad (5.5)$$

where α_{i} split coefficient from core i to annulus i [-],
$u_{\mathrm{c,i}}$ velocity of solids leaving from core i to core i+1 [m/s],
$u_{\mathrm{ca,i}}$ velocity of solids leaving from core i to annulus i [m/s],
A_{i} node area [m^2].

The split coefficient α_{i} from core to annulus is a factor between 0 and 1. If there was no solid transport from core to annulus, the mass flux from core i to core i+1 would be the solid velocity multiplied by the solid density in the core element. By introducing the split coefficient, a share of this mass flux is taken to the adjacent annulus element and the rest flows to the upper core element, as presented by Eq. (5.4) and (5.5).

The mass flows leaving the annulus node are calculated similarly as with core elements.

$$\dot{m}_{\mathrm{a,i}}(t) = (1 - \beta_{\mathrm{i}}) \cdot u_{\mathrm{a,i}}(t) \cdot \rho_{\mathrm{a,i}}(t) \quad (5.6)$$

$$\dot{m}_{\mathrm{ac,i}}(t) = \beta_{\mathrm{i}} \cdot u_{\mathrm{ac,i}}(t) \cdot \rho_{\mathrm{a,i}}(t) \quad (5.7)$$

where β_{i} split coefficient from annulus i to core i [-],
$u_{\mathrm{ac,i}}$ velocity of solids leaving annulus i to annulus i-1 [m/s].

The split coefficient β_{i} works in the same way as the split coefficient α_{i}. It allows solids in the annulus elements to flow back to the core. This solid migration is much less pronounced as from core to annulus and thus the split coefficient in Eq. (5.6) and (5.7) is of minor importance, and therefore often neglected. It was included to the model in order to provide an additional tool for modelling hydrodynamic phenomena according to different needs.

The split coefficients are determined as (Tuuri & Lappalainen 2018)

$$\alpha_{\mathrm{i}} = \alpha_{\mathrm{global}} \cdot \alpha_{\mathrm{local,i}}, \qquad 0 \leq \alpha_{\mathrm{i}} \leq 1 \quad (5.8)$$

$$\beta_{\mathrm{i}} = \beta_{\mathrm{global}} \cdot \beta_{\mathrm{local,i}}, \qquad 0 \leq \beta_{\mathrm{i}} \leq 1 \quad (5.9)$$

where $\alpha_{\mathrm{global}}, \beta_{\mathrm{global}}$ global split coefficient for each element [-],
$\alpha_{\mathrm{local,i}}, \beta_{\mathrm{local,i}}$ local split coefficient in element i [-].

As presented in Eq. (5.8) and (5.9), the split coefficients are obtained by multiplying the global and local split coefficients. The global coefficient is a uniform value for every core/annulus element and the local coefficient can be given to each element separately. This gives freedom for the tuning of internal circulation mass flows. The local coefficients can be given values between 0…10 and their default value is 1. The global coefficients as well as the total coefficients are limited to have only values between 0 and 1.

5.5.2 **High-density Bed and the Interface Layer**

If we assumed that the mass flux leaving the bottom bed was the product of the bottom bed density and solid velocity, a higher bed density would mean a higher mass flux. So, if the gas velocity is dropped, the bottom bed becomes less expanded, i.e. denser, but a smaller gas velocity also means less drag impacted on the bed material, so smaller solid velocity. Therefore, there would be complications when calculating the mass flux in the aforementioned manner. Hence, there is a need to model the solid densities of the high-density bed and upper furnace separately.

To solve this, a theoretical concept, an interface layer, was constructed between the high-density bed and the core-annulus structure, seen in Figure 5.3 (Tuuri & Lappalainen 2018). Its purpose is to give a boundary condition for the solver of the upper furnace and is therefore a very important parameter in calculation. It is assumed to be infinitely thin, thus having no volume and no need to account for in mass and energy balances. The interface density is a user-given value that determines the mass flux leaving the high-density bed to the first core node, as

$$\dot{m}_0(t) = u_{\mathrm{c},0}(t) \cdot \rho_{\mathrm{int}}(t) \cdot A_0 \tag{5.10}$$

In normal conditions, the interface density is not dependent of the density nor height of the high-density bed. However, if the bed material in the high-density bed is depleted to a low-enough level, less than 10 kg/m^3, the interface density is automatically decreased. This aims to prevent the upward solids flow from emptying the high-density bed in an unrealistic manner.

The dependence between the interface density and the split coefficients α is as follows, assuming split coefficients β to be 0 and the system to be in steady state. The derivation of the equations is provided in Appendix 1.

$$\rho_{\mathrm{int}} = \frac{\rho_{\mathrm{N}}}{C(1+D)} \tag{5.11}$$

where $$C = \prod_{\mathrm{i}=1}^{\mathrm{N}-1}(1-\alpha_{\mathrm{i}}) \cdot \prod_{\mathrm{j}=1}^{\mathrm{N}} \left(\frac{A_{\mathrm{i}-1} u_{\mathrm{c,i}-1}}{(1-\alpha_{\mathrm{i}}) \cdot A_{\mathrm{i}} \cdot u_{\mathrm{c,i}} + \alpha_{\mathrm{i}} \cdot A_{\mathrm{i}} \cdot u_{\mathrm{a,i}}} \right) \tag{5.12}$$

$$D = \alpha_{\mathrm{N}} \frac{A_{\mathrm{N}}}{A_{\mathrm{N}-1}} \tag{5.13}$$

Equations (5.11)…(5.11) are not used in the model itself. The equations can be used in the Apros environment by using the SCL programming language to get the desired exit density. In this situation, the suspension density at the Nth, so highest, node is given by the user. The suspension density required to get the desired exit density is then calculated with the equations. The suspension density profile can be then adjusted by modifying the global split coefficient α. Also, the local split coefficients α_{i} are usually defined beforehand. Fine-tuning can then be done by adjusting the split coefficients β_{i}. However, to acquire accurate results in this situation, equations (5.11)…(5.13) must be modified to include also the split coefficients β_{i}. Different interface densities lead to different suspension density profiles and different solid velocities in the nodes. Therefore, the equations must by calculated multiple times, because the desired interface density develops iteratively.

Normally, the interface density is a constant value and does not change during simulation. It may, however, be changed if needed. In Apros, it is possible to calculate the interface density at each time step and to give it as an input to the CFB component.

5.5.3 **Pressure Drop**

Solids in the furnace cause a pressure drop in the fluidizing gas. The gas pressure drop in the nodes is an important variable. Often only pressure loss measurement data can be obtained from commercial CFB furnaces. Hence, CFB boiler models can often be validated only by pressure loss data.

In the model, a loss coefficient caused by the solids is calculated for the gas flow

$$k = \frac{2\Delta p_{\mathrm{h}}}{\rho_{\mathrm{g}} u_{\mathrm{g}}^2} \tag{5.14}$$

where Δp_{h} hydraulic head over a node [Pa].

It is assumed that the pressure loss caused by the particles is the same as the hydraulic head of the fluidized solids. The hydraulic head is calculated as

$$\Delta p_{\mathrm{h}} = \frac{g m_s (\rho_{\mathrm{p}} - \rho_{\mathrm{g}})}{\rho_{\mathrm{p}} A_{\mathrm{node}}} \tag{5.15}$$

where m_{s} mass of solids in the node [kg],
ρ_{p} average density of the particles [kg/m^3].

5.5.4 **High-density Bed Height**

Due to the selected discretization scheme, the node height of the bottom node, modelling the high-density bed, is constant. The bottom node should therefore be high enough to be able to contain the high-density bed, but low enough so that the height difference between the node and the bed would be small. The node should also allow the model to work properly during transients, where the high-density bed height could vary.

The calculation of the high-density bed height is started by first making an equation for the suspension density of the bed. The equation assumes that practically all solids in the bottom node are in the high-density bed, which makes the equation very simple. Note that in these equations, the subindex “bn” refers to the entire bottom node and the subindex “hbd” refers to the high-density bed which is smaller than the bottom node.

$$\rho_{\mathrm{hdb}} = \frac{m_{\mathrm{bn}}}{V_{\mathrm{hdb}}} \tag{5.16}$$

where ρ_{hdb} average suspension density in the high-density bed [kg/m^3],
m_{bn} mass of solids in the bottom node [m],
V_{hdb} volume of the high-density bed [m^3].

The suspension density in Eq. (5.16) can be also calculated as

$$\rho_{\mathrm{hdb}} = (1 - \varepsilon_{\mathrm{hdb}}) \cdot \rho_{\mathrm{solid}} + \varepsilon_{\mathrm{hdb}} \cdot \rho_{\mathrm{gas}} \tag{5.17}$$

Calculation of the high-density bed void fraction, $\varepsilon_{\mathrm{hdb}}$, in Eq. (5.17), is presented in the supplementary material of the reference (Lappalainen et al. 2014).

By combining equations (5.16) and (5.17), the equation for the high-density bed height is obtained as

$$H_{\mathrm{hdb}} = \frac{m_{\mathrm{bn}}}{(1-\varepsilon_{\mathrm{hdb}})\cdot\rho_{\mathrm{solid}}+\varepsilon_{\mathrm{hdb}}\cdot\rho_{\mathrm{gas}}} \cdot \frac{1}{A_{\mathrm{bn}}} \tag{5.18}$$

The high-density bed voidage, $\varepsilon_{\mathrm{hdb}}$, is defined for fluidizing gas velocities greater than the minimum fluidizing velocity. Despite being outside the given validity range, it was decided to use Eq. (5.18) also in these very low velocities to make the model simpler. Moreover, the bed height is used as merely a control variable, displaying the state of the bottom node, so its values in very low velocities do not affect the simulation.

The high-density bed height, H_{hdb}, does not vary much in normal operation, but in case the bed height becomes too high or too low, restrictions must be made. Because the high-density bed is assumed to be only in the bottom node, it should not become higher than the bottom node height. Therefore, when the bed height becomes more than 99 % of the node height, the interface density is automatically increased in order to decrease the bed height and to prevent errors in the mass balance.

5.6 Solid Flow Velocities

This subchapter introduces the solid velocities used in the solid balance calculations. The solid velocities affect greatly to the furnace hydrodynamics, so the subject requires careful investigation. The velocities of interest are the upward velocities in the core, downward velocities in the annulus and the vertical velocities between the adjacent core and annulus nodes. All of these velocities utilize the terminal velocity of a single particle, so it is introduced first.

5.6.1 **Terminal Velocity**

Perhaps the most important variable in calculating the bed material velocities is the terminal velocity which is the free-fall velocity of a particle. In a furnace, it is the velocity at which the drag force of gas on a particle counterweighs its gravity, making it float in the gas flow. Many terminal velocity correlations are for spherical particles, but in commercial fluidized bed applications, particles are never perfect spheres and assuming so causes significant error in calculating the velocities. Therefore, a property known as sphericity must be included in the terminal velocity calculation. For a particle, sphericity, ϕ, is the area of a sphere that has the same volume as the particle, divided by the real surface area of the particle. It can have values in the range]0, 1], the value 1 representing a perfect sphere. Solids used in the CFB furnace have typically sphericities in the range [0.5, 0.85].

Calculation of terminal velocity often includes determining the drag coefficient of a particle. As the coefficient is dependent of the velocity that is to be calculated, iterations must be made. Another way to calculate terminal velocity is through dimensionless particle size and dimensionless terminal velocity, making the calculation more straightforward. There are many correlations in literature for the drag coefficient of a non-spherical particle (Bagheri & Bonadonna 2016; Krueger et al. 2015; Dioguardi & Mele 2015), but correspondent correlations for dimensionless terminal velocity are very few in numbers. However, dimensionless terminal velocity calculation was chosen because of its simplicity (Tuuri & Lappalainen 2018). Terminal velocity is calculated for each node. The particle density is calculated as a weighted average of the solids inside the node. First, dimensionless particle size is calculated (Kunii & Levenspiel 1991).

$$d^*_{\mathrm{p,i}}(t) = d_{\mathrm{p}} \left[\frac{\rho_{\mathrm{g,i}}\,(t) \cdot (\rho_{\mathrm{p}} - \rho_{\mathrm{g,i}}(t)) g}{\mu_{\mathrm{g,i}}(t)^2} \right]^{1/3} \tag{5.19}$$

where d_{p} particle diameter [m],

ρ_{g} gas density [kg/m^3],

ρ_{p} particle density [kg/m^3],

g acceleration due to gravity, 9.81 m/s^2,

μ_{g} gas dynamic viscosity [kg/m^2/s].

Using dimensionless particle size from Eq. (5.19), dimensionless terminal velocity is calculated with a correlation from Haider and Levenspiel (1989, 69). This correlation predicts well against empirical data and covers a wide range of particle sphericities, ϕ ($0.5 \leq \phi \leq 1$).

$$u_{\mathrm{t,i}}^{*}(t) = \left[\frac{18}{d_{\mathrm{p,i}}^{*}(t)^{2}} + \frac{2.335 - 1.744\phi}{d_{\mathrm{p,i}}^{*}(t)^{0.5}}\right]^{-1} \tag{5.20}$$

Finally, the particle terminal velocity is calculated using dimensionless terminal velocity from Eq. (5.20) (Kunii & Levenspiel 1991).

$$u_{\mathrm{t,i}}(t) = u_{\mathrm{t,i}}^{*}(t)\left[\frac{\rho_{\mathrm{g,i}}(t)^{2}}{\mu_{\mathrm{g,i}}(t)\cdot(\rho_{\mathrm{p}} - \rho_{\mathrm{g,i}}(t))g}\right]^{-1/3} \tag{5.21}$$

Within this CFB model version, the tuning of terminal velocity can be done by changing the average particle size, particle densities or sphericity. This is a complicated way of tuning such an important variable and leads to unpredictable results, as it is hard to predict how much a change in particle size changes the terminal velocity, for instance. A simpler and more efficient way to tune the terminal velocity would be to have a control coefficient with which the terminal velocity would be multiplied. This is a subject for future development.

The particle velocity, which is applied in solving the solid phase velocity, can be determined using the local gas velocity and the terminal velocity of a particle, calculated from equations (5.19)…(5.21).

$$u_{\mathrm{particle,i}}(t) = u_{\mathrm{g,i}}(t) - u_{\mathrm{t,i}}(t) \tag{5.22}$$

The gas side is modelled with basic Apros components and using the 3-equation pressure-flow model. In the CFB model, the solid side affects the gas side velocities only by pressure losses. In reality, the particles also decrease the flow area of gas, therefore increasing its velocity. This is, however, not included in the model at this stage, but may be a subject for future development.

5.6.2 **Core Zone**

In the core zone, particles are not allowed to flow downward, as it is allowed only in the annulus zone. A restriction was therefore made for the solid velocities in the core, following Eq. (5.22) (Tuuri & Lappalainen 2018).

$$u_{\mathrm{c,i}}(t) = \max\left(u_{\mathrm{particle,i}}(t)\ ;\ 0\right) \tag{5.23}$$

If the gas velocity falls below the terminal velocity of the particle, the particle remains in the core node until it is transferred to the adjacent annulus node.

In order to facilitate the startup/shutdown scenario, a new variable was introduced, shown in the equation below.

$$u_{\mathrm{c,tot,i}}(t) = u_{\mathrm{c,i}}(t) + u_{\mathrm{startup}} \tag{5.24}$$

The attribute u_{startup} is a user-given global constant which is shared between all core nodes. Its default value is 0, as it is designed to be used only in the startup and shutdown situations. It is used to make the startup and shutdown smoother. As the Apros CFB model does not include particle size distribution, using the additional velocity during startup helps particles to start flowing upwards earlier, representing fines. The variable therefore helps overcome the deficiencies caused by neglecting particle size distribution in the model.

5.6.3 **Annulus Zone**

In CFBs, the gas velocity in the annulus zone is significantly less than in the core zone. Simple correlations for the gas velocity at the annulus were not found, so a simplification was made. The gas velocity at the annulus is only used for calculating velocities for the particles, as the gas nodes follow the 1D scheme. The upward gas velocity at the annulus is controlled with a coefficient (Tuuri & Lappalainen 2018)

$$u_{\mathrm{g,a,i}}(t) = k_{\mathrm{vel,a}} \cdot u_{\mathrm{g,i}}(t) \tag{5.25}$$

The coefficient $k_{\mathrm{vel,a}}$ can have values between 0…0.5, the default being 0.

In the annulus solid balance, particles cannot flow upward. A similar restriction as with the core zone is therefore made. In addition, the terminal velocity of the particles are multiplied with the coefficient $k_{\mathrm{vel,cluster}}$. The coefficient is used, because particles in the annulus do not fall down at the terminal velocity of a single particle. Particles at the annulus form clusters that may fall at a speed of 2…8 m/s, as stated in Chapter 3.1, a far greater speed than the terminal velocity of a typical particle.

$$u_{\mathrm{a,i}}(t) = \min(\, k_{\mathrm{vel,a}} \cdot u_{\mathrm{g,i}}(t) \; - \; k_{\mathrm{vel,cluster}} \cdot u_{\mathrm{t,i}}(t) \; ; \; 0) \tag{5.26}$$

The coefficient $k_{\mathrm{vel,cluster}}$ can have values between 1…10, the default being 1.

When the wall velocity coefficient, $k_{\mathrm{vel,a}}$, is 0, and the cluster velocity coefficient, $k_{\mathrm{vel,cluster}}$, is 1, particles at the annulus fall downwards with their terminal velocity. If the wall velocity coefficient is greater than 0 and the gas velocity overweighs the particle terminal velocity, the particles remain in the annulus node until they are returned back to the core node. However, if the split coefficient β is 0 and the split coefficient α is greater than 0, bed material may then accumulate into the annulus nodes, which is unrealistic. Therefore, the wall velocity coefficient must be altered carefully. Increasing the cluster velocity coefficient on the other hand increases the downward velocity of particles in the annulus, and therefore also the velocity of particles flowing from core to annulus. Hence, the coefficient greatly affects furnace hydrodynamics, and should also be done carefully. Increasing the cluster velocity coefficient, $k_{\mathrm{vel,cluster}}$, has a similar effect as increasing the global split coefficient α.

The annulus zone velocity is used also in determining the velocities of solids from core to annulus. The modelling solution for the velocity was chosen for its simplicity and stability in the entire scope of operation. However, the solid velocities from core to annulus being nearly constant is unrealistic. Therefore, the annulus zone velocity may cause some dynamic responses which are not realistic. This is investigated in Chapter 6.2.1.

5.6.4 Solid Velocities between the Core and Annulus Zones

In equations (5.3) and (5.5) it is assumed that the radial solids flow velocities are equal to the axial ones. A restriction must, however, be made for situations where e.g. core zone velocity goes to zero (Tuuri & Lappalainen 2018)

$$u_{\mathrm{ca,i}}(t) = u_{\mathrm{a,i}}(t) \tag{5.27}$$

$$u_{\mathrm{ac,i}}(t) = \begin{cases} u_{\mathrm{a,i}}(t), & \text{when } u_{\mathrm{c,i}}(t) > 0 \\ 0\,, & \text{when } u_{\mathrm{c,i}}(t) = 0 \end{cases} \tag{5.28}$$

Eq. (5.27) shows that the velocity of solids flowing from core to annulus is always the velocity of the annulus zone. If the core zone velocity was used instead, solids would get trapped in the core elements at low gas velocities. In Eq. (5.28), velocity from annulus to core is equal to the annulus zone velocity, when the core zone velocity is positive. When the core zone velocity goes to zero, the material transport from annulus to core is prevented, as in this situation all bed material must fall to the bottom bed.

When the core zone velocity is reduced to zero, all bed material should fall to the bottom of the furnace relatively quickly. It takes some time for the core nodes to be clear of particles, so it may take an unrealistically long time for the upper furnace to become clear of bed material. In this case, the coefficient $k_{\mathrm{vel,cluster}}$ in Eq. (5.26) should be increased. This increases solid velocity from the core to the annulus as well as within the annulus zone and therefore the downward flow to the bottom furnace.

5.7 External Circulation Components

External circulation components comprise usually the cyclone, standpipe, loopseal and EHE. The solid flow mechanisms in the components are simple enough that they are usually modelled as 0D, either as all volumes lumped to a single calculation volume, or several ones used in series. In Apros, there is a particle storage component (PSC) that can be used for these purposes.

The PSC describes only the particles; there is no gas volume considered in the component. The PSC is given the average size of particles, the allowed solid material types, and as initial

values, the total mass and mass fractions of different materials and the PSC temperature. From these, the amount of energy in the PSC is calculated. It can be transferred to a fluid flow line with a specific heat transfer component.

The Apros CFB model calculates the solid mass flow out of the furnace, and this can be given as an input for the PSC representing the cyclone. The PSC works as a solids inventory, but does not model mass transfer. Particle transmitters are available for this purpose, i.e. to employ mass flows to/from a PSC. Currently, the mass flows are not solved, but are given or calculated by the user. Therefore, the mass transfer rates of particle flows to/from the PSCs is typically manipulated and controlled with automation components. The external solids circulation methology has not been further developed alongside the current solid balance model development effort. More accurate modelling of the external circulation is not part of this thesis, but they are objects of further development in the future.

5.8 Heat Transfer

A major simplification in the heat transfer submodel is that heat is extracted to the water walls only from the flue gas nodes (Tuuri & Lappalainen 2018). Core and annulus phases do affect the heat transfer, according to Equations (3.3) and (3.4), but the model is simpler, when heat is extracted to the walls from only one type of calculation element instead of all three. The gas phase is the easiest to implement and it was therefore chosen. Heat transfer between gas and solids is assumed to be so intense that temperature differences between the gas phase and core and annulus phases inside each vertical node remain small.

Figure 5.4 shows schematically how heat is transferred in the model. The solids in the core and annulus transfer heat only with the flue gas. Each flue gas node transfers heat to the water/wing wall metal from which heat flows to the water/steam line, assuming that heat transfer is configured by the user for the node in question. There is no heat transfer modelled between the core and annulus other than the heat that is transferred due to the solids transport. There is, however, an option to switch on thermal diffusion (off by default) between the core nodes, represented by the dashed lines in Figure 5.4. It provides a means for fine-tuning the vertical temperature profile. There is no thermal diffusion modelled for gas or annulus nodes, as heat transfer between the three is efficient and core diffusion already affects both. So,

vertical material flows and the optional diffusion in core nodes take care of the vertical heat transfer inside the furnace. There are, however, various options to define heat transfer from the flue gas nodes to heat exchangers, such as the radiant superheaters and reheaters. (Tuuri & Lappalainen 2018.)

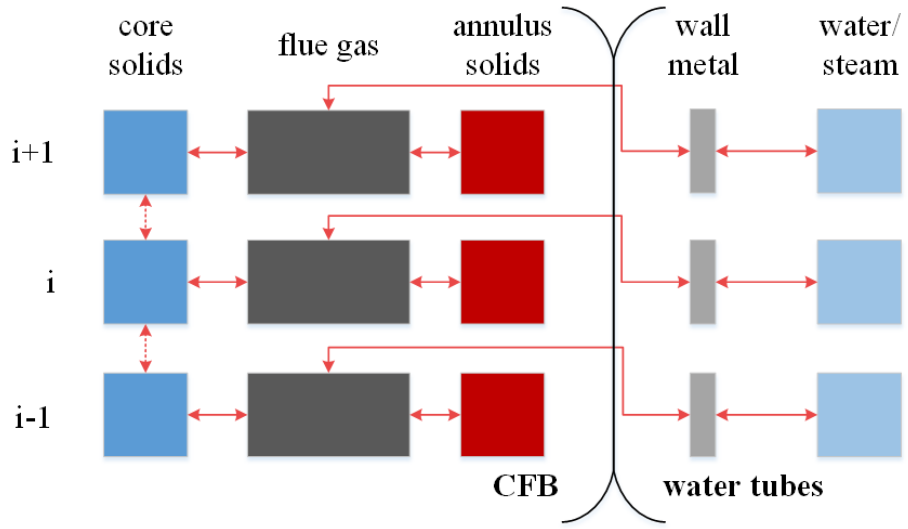

Figure 5.4. Schematic of heat transfer in the CFB component and the connected heat exchangers, for example the water walls. The brackets indicate the interface of the CFB component and the Heat pipe component of Apros.

To calculate heat transfer to the water walls and wing walls in the furnace, a correlation for the total heat transfer coefficient (HTC) in the furnace side tube wall surface is needed. The total HTC in the tube wall surface of the furnace side consists of multiple heat transfer mechanisms, mainly particle convection, particle radiation and gas radiation. The coefficient tells how much heat, at a theoretical maximum, can travel through the furnace wall surface if the thermal resistances of the tube wall and tube inner surface are very small. The total HTC over the water wall tubes is less than this, because it contains also the thermal resistances of the wall layer and steam side surface. The outer surface of the water wall is the interface for the CFB calculation model, so only this coefficient is discussed. The rest of the water wall is modeled with other Apros model components. The water wall and wing wall HTCs are calculated with Dutta-Basu correlations, so Equations (3.3) and (3.4), presented in Chapter 3.4.2.

5.9 Sensitivity Analyses for Key Correlations Used in the Model

It is important to note that correlations are typically based on empirical data, and the data is always obtained from systems with their specific conditions. Data obtained from one system can be very different than data obtained from another, and therefore the correlations fitted to the data will be different too. Correlations work best for the systems they were designed for. For example, correlations designed for small systems do not necessarily work when scaling up to larger systems, or when extrapolating the correlation outside the range that it was defined in. This problem in semi-empirical models must be addressed.

Ideally, the CFB model would have multiple correlations for e.g. terminal velocity that would cover different ranges of particle size, temperature and sphericity, among others. However, this makes the model overly complex and the data requirements huge. Not only would the model require logical structures to decide which correlation to use, but there would be issues when transitioning from one equation to another. In the transition point, the correlations most probably predict different values, so there would be a discontinuity. In this kind of transition, the calculated property would drop or rise rapidly, affecting the model behaviour in an unwanted way. To tackle this problem, the transition zones would need to be smoothened, but this would add considerably to the complexity of the model. Therefore, the decision was made that in this development stage of the CFB model, physical phenomena in the CFB are modelled with only one correlation each. Selected coefficients in these correlations can then be tuned to apply better to different systems and conditions.

Correlations for terminal velocity and HTC are inspected here. A sensitivity analysis is done for both of them to see what parameters affect the correlations the most.

5.9.1 Terminal Velocity

Figure 5.5 presents a sensitivity analysis for particle terminal velocity. Equations (5.19)…(5.21) have four variables that can be changed independently, so the analysis was done by changing one variable at a time and keeping the remaining at constant values. The values are presented in Table 5.1. In atmospheric pressure, gas density and viscosity are functions of only temperature with a constant composition, so they change along with it. The calculations were done for air. The values and their ranges are typical for a CFB.

Table 5.1. Constant values for equations (5.19)…(5.21).

Particle size, d_p	150 µm
Temperature, T	847 °C
Particle density, ρ_p	1500 kg/m^3
Sphericity, ϕ	0.84

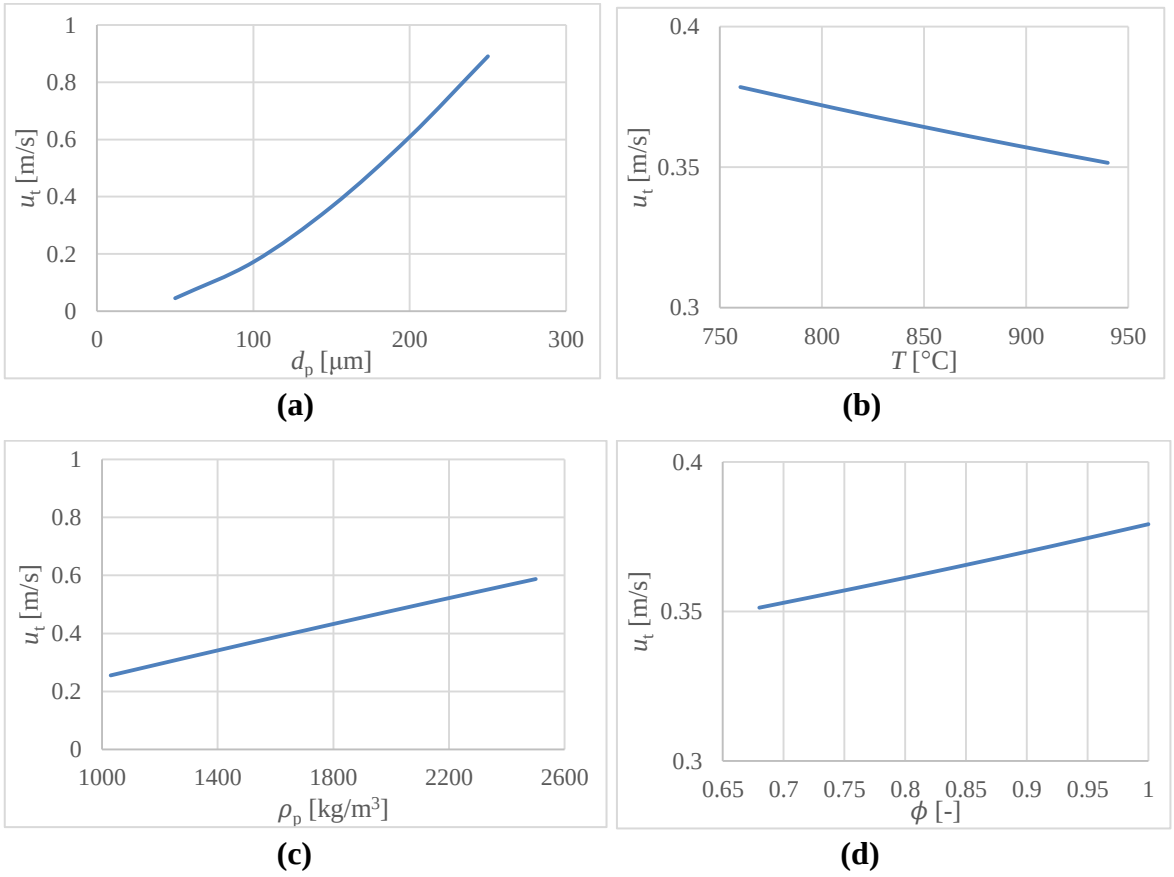

Figure 5.5. Sensitivity analysis for particle terminal velocity calculated using equations (5.19)…(5.21). Sensitivity of terminal velocity for: a) particle size; b) gas temperature; c) particle density; d) particle sphericity. Note that figures a) and c) as well as b) and d) have the same scales for the y-axis, making the comparison of the curves easier.

Terminal velocity increases as particle diameter, density and sphericity are increased. A larger, heavier and more round particle has more volume and thus weight compared to its surface area, making it harder for the gas flow to lift it. Only an increase in temperature lowers terminal velocity, as it increases viscosity. The decrease in gas density has less effect compared to the increase in viscosity.

In Figure 5.5 it can be seen that temperature and sphericity have relatively little impact on terminal velocity, whereas particle density and particle size have a major impact, especially particle size. Therefore, in the operating range of a CFB, special attention should be paid to getting the particle size and density right, with respect to terminal velocity.

It is important for the model to operate reasonably also when the boiler is going through a cold start-up or overheating due to e.g. a disturbance in the water/steam line. Therefore, sensitivity of terminal velocity should be addressed also in a temperature range of 25…1125 °C. Figure 5.6 shows the results of this analysis. The change in terminal velocity is quite linear in the temperature range, so using the correlation should not be problematic even in the conditions of extreme temperature. The results were obtained using the same constant values for the other variables as in the earlier analysis. The behaviour was however similar when using different constant values for the remaining variables.

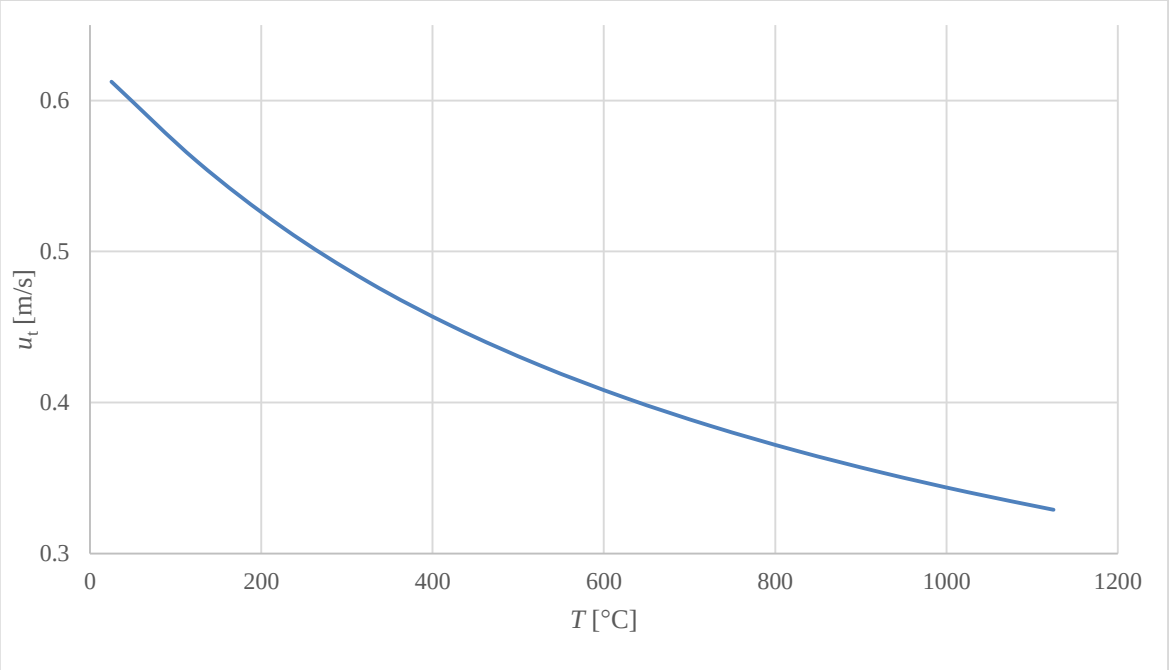

Figure 5.6. Sensitivity analysis of particle terminal velocity in a temperature range of 25…1125 °C.

5.9.2 Total Heat Transfer Coefficient

Figure 5.7 presents a sensitivity analysis for Eq. (3.3), the total HTC for water walls. Eq. (3.4), the total HTC for wing walls, is not included, as it behaves similarly to Eq. (5.21), but more mildly. Figure 5.7a shows the sensitivity of the correlation to suspension density while

keeping temperature at 847 °C. Suspension density is varied between 2…80 kg/m^3 and it can be observed that suspension density has a large impact on total HTC in typical bed conditions. Figure 5.7b shows the sensitivity of the correlation to temperature while keeping suspension density at 28 kg/m^3. Temperature is varied between 760…940 °C. In the figure (a), total HTC rises from 115 to 486 W/m^2/K and in (b) from 317 to only 329 W/m^2/K. Suspension density has clearly much larger effect on the total HTC than temperature. If model tuning is required, the results of Equations (3.3) and (3.4) can be freely multiplied with a tuning coefficient.

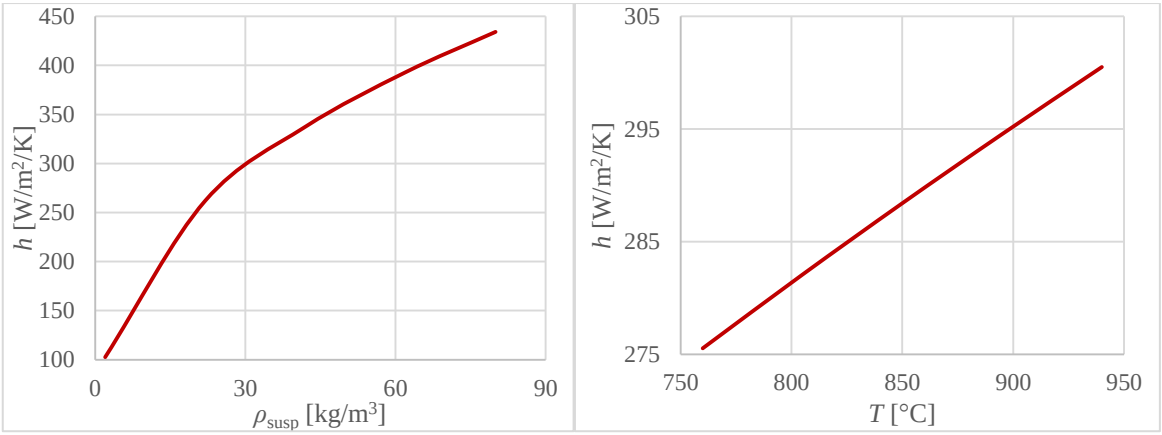

(a) **(b)**

Figure 5.7. Sensitivity analysis for total heat transfer coefficient calculated using Eq. (3.3). Sensitivity of heat transfer coefficient for: a) suspension density; b) temperature.

As for terminal velocity, the sensitivity analysis for total HTC was carried out in a wide temperature range of 25…1125 °C. Figure 5.8 shows the results of this analysis. The change in total HTC is quite linear in the temperature range, so the correlation is not problematic even at extreme furnace temperatures. The results were obtained using a suspension density of 28 kg/m^3. The results were however similarly close to linear when using different constant values as well.

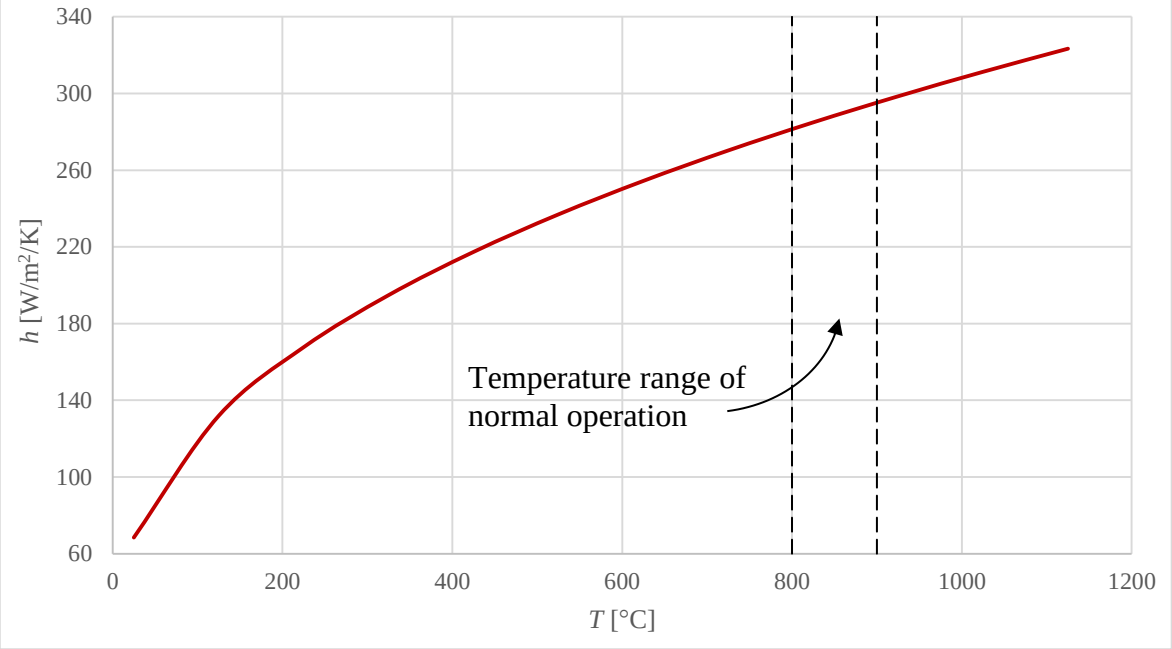

Figure 5.8. Sensitivity analysis of total heat transfer coefficient to water walls in a temperature range of 25…1125 °C.

It is worth noting a potential problem, when using this correlation at extreme temperatures. The correlation was made for commercial CFB furnaces which normally operate at temperatures in the range of 800…900 °C. As heat transfer by radiation is highly dependent of temperature, the correlation gives a poor estimate of the total HTC outside the normal CFB operation temperatures. Thermal radiation emitted by a substance is as follows

$$P = \varepsilon(T) \cdot \sigma \cdot A \cdot T^4 \tag{5.29}$$

where ε emissivity [-],

σ Stefan-Boltzmann constant, $5.67 \cdot 10^{-8}$ W/m^2/K^4,

A surface area [m^2].

As seen from Eq. (5.29), thermal radiation increases to the fourth power of temperature. Therefore, at temperatures much higher than in the normal operation range, the relatively linear Dutta-Basu equations give too low values for heat transfer. Conversely, at temperatures much lower than in the normal operation range, the Dutta-Basu equations give too high values for heat transfer.

5.10 Modular Structure of the Apros CFB Model

The CFB model in Apros consists of gas and solid flow structures, as presented in Figure 5.9. The gas structure consists of nodes and composition modules (NO and CM) and flow branches (BR and CB) between them. Pressures, enthalpies and other state variables are calculated in the nodes and gas composition and variables important for reaction calculation are calculated in the composition modules. The solid flow structure consists of heat structure modules (HS), their nodes (HN) and heat flow modules (HF) that transfer solids between the heat nodes. There are heat transfer modules (HT and HR) between the solid and gas nodes.

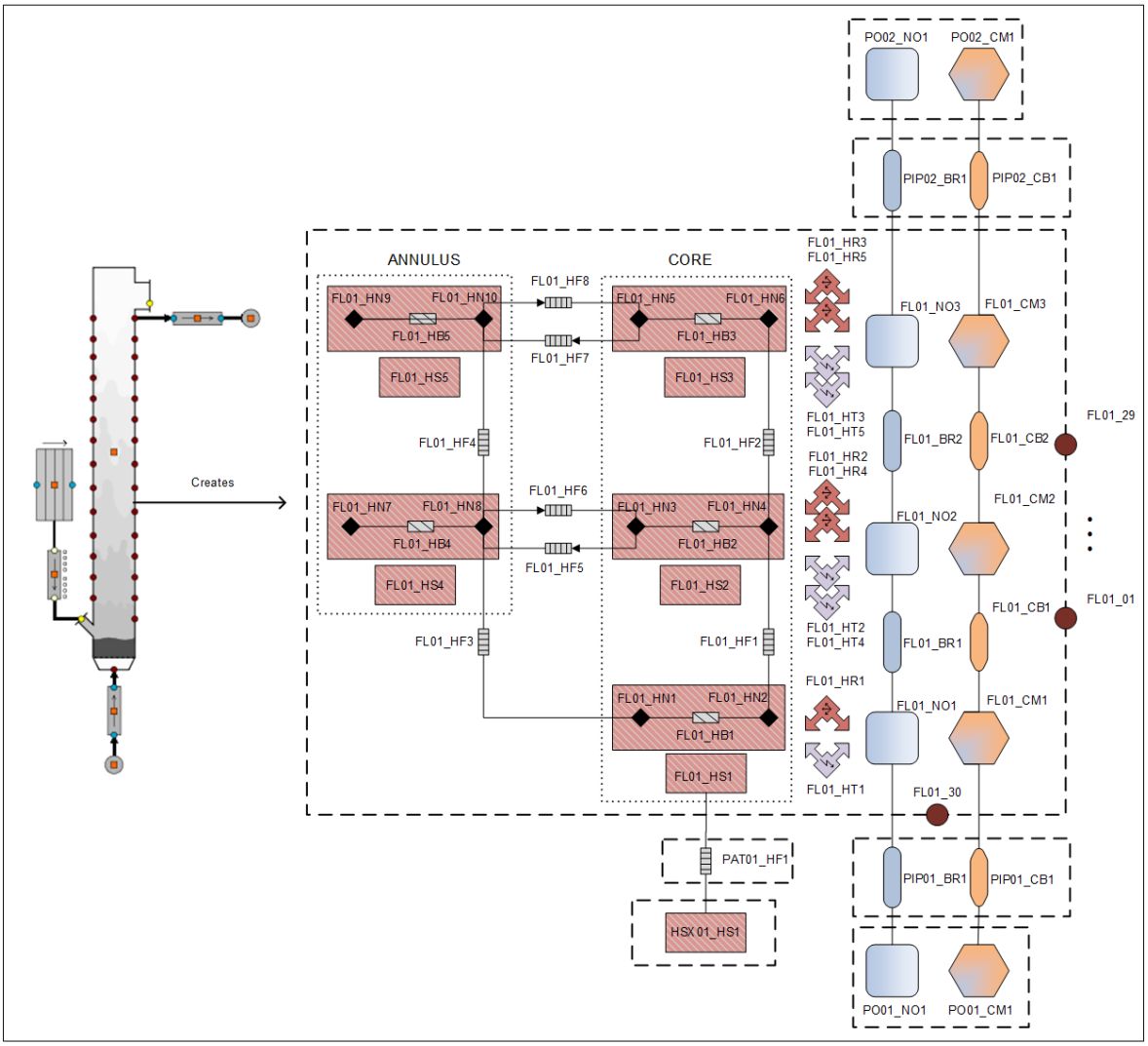

Figure 5.9. Modular structure of the Apros CFB model. Modified from the structure of the previous CFB model version.

6 VERIFICATION OF THE PRELIMINARY APROS CFB MODEL

The focus of this chapter is on the verification of the Apros CFB model. The concepts of verification and validation is discussed in the Introduction, in Chapter 1.2. The mass and energy balances of the model are first verified. Then, the furnace hydrodynamics are verified during normal operation startup and shutdown as well as in certain special cases. The normal operation includes cases such as increasing the secondary air flow and the total mass of bed material in the furnace. The special cases include the emptying of the furnace during operation and a sudden stop in fluidizing air. Heat transfer and combustion in a CFB boiler model are verified with a step change in fuel feed.

6.1 Verification of the Solids Mass and Heat Balances

The mass and heat balances of the solids must be verified in order to make sure that the model programming is implemented correctly and as planned, and that the calculation results of the CFB component are trustworthy. The verification was done in two control volumes: the bed bottom and the upper part of the furnace. The tested CFB model was divided into four nodes, so the bottom bed was the first node and the upper furnace consisted of nodes 2…4. For a more accurate description of the nodes in the model, refer to Figure 5.9. Mass and heat balances must hold true in any given time in the model and the best way to test this is to change some key parameters in the model. Heat transfer to water/steam tubes was not configured in the model. If the balances hold true, the verification can be deemed successful.

To make the testing consistent and efficient, an SCL (Simantics Constraint Language) script was made. SCL is a programming language which can be used in Apros for model configuration and the running of scenarios. When such a script is run in Apros, all defined parameter modification and progressing to the simulation is done automatically. The same test script, see Appendix 2, was used in both cases. Three different key parameters were changed individually with the script:

1. Solid feed to the bottom of the bed,
2. Fluidizing gas mass flow,
3. Fluidizing air temperature.

For checking purposes, mass balances were configured as automation component calculations within the Apros model and are continuously calculated as the simulation goes on. In equation form, the mass balances are

$$m_{\mathrm{tot}} = \sum_{\mathrm{i}=1}^{\mathrm{N}} \left(m_{\mathrm{c,i}} + m_{\mathrm{a,i}} \right) \tag{6.1}$$

$$m_{\mathrm{net}} = \int_{t}^{t_{\mathrm{end}}} \left(q_{m,\mathrm{in}} - q_{m,\mathrm{out}} \right) dt \tag{6.2}$$

where m mass [kg],
q_m mass flow [kg/s].

Equation (6.1) gives the total solid mass amount in the defined control volume at each time step. In equation (6.2) the net mass flow to the system over a time period of 1 second is integrated. The output of the equation is the accumulated net change in mass from the beginning of the simulation to a time instance. In a similar manner, the energy balances are

$$Q_{\mathrm{tot}} = \sum_{\mathrm{i}=1}^{\mathrm{N}} \left(Q_{\mathrm{c,i}} + Q_{\mathrm{a,i}} + Q_{\mathrm{gas,i}} \right) \tag{6.3}$$

$$Q_{\mathrm{net}} = \int_{t}^{t_{\mathrm{end}}} \left(q_{\mathrm{in,solid}} - q_{\mathrm{out,solid}} + q_{\mathrm{in,gas}} - q_{\mathrm{out,gas}} \right) dt \tag{6.4}$$

where Q energy [kJ],
q energy flow [kW].

The energy quantities in equation (6.3) and the gas energy flows in equation (6.4) cannot be acquired directly in Apros, but are calculated from other attributes.

Graphs for both balances were drawn to study whether the balances hold. Two curves were drawn to each graph: one for the mass/energy in the control volume and another for the change of mass/energy calculated from the mass/energy flows in and out of the control volume. The total mass and energy amounts of equations (6.1) and (6.3) were corrected accordingly

$$m_{\mathrm{tot,scaled}}(t) = m_{\mathrm{tot}}(t) - m_{\mathrm{tot,0}} \tag{6.5}$$

$$Q_{\mathrm{tot,scaled}}(t) = Q_{\mathrm{tot}}(t) - Q_{\mathrm{tot,0}} \tag{6.6}$$

where subindex 0 refers to the initial steady state value at the beginning of the simulation.

This correction made both curves start at zero, making it easier to see if the two curves were identical. If the curves remain identical at any given time during the simulation, the balances hold true.

6.1.1 **Bottom Bed**

The first control volume under inspection is the bed bottom, i.e. the single node representing the dense bed in the CFB component, see Figure 6.1. The node consists of the first core element and the first gas node. Gas enters the control volume from outside the furnace and exits the volume to go to node 2. Solids flows entering the control volume come from the annulus element of node 2 and from the loopseal. A single solids flow exits the volume and flows to node 2.

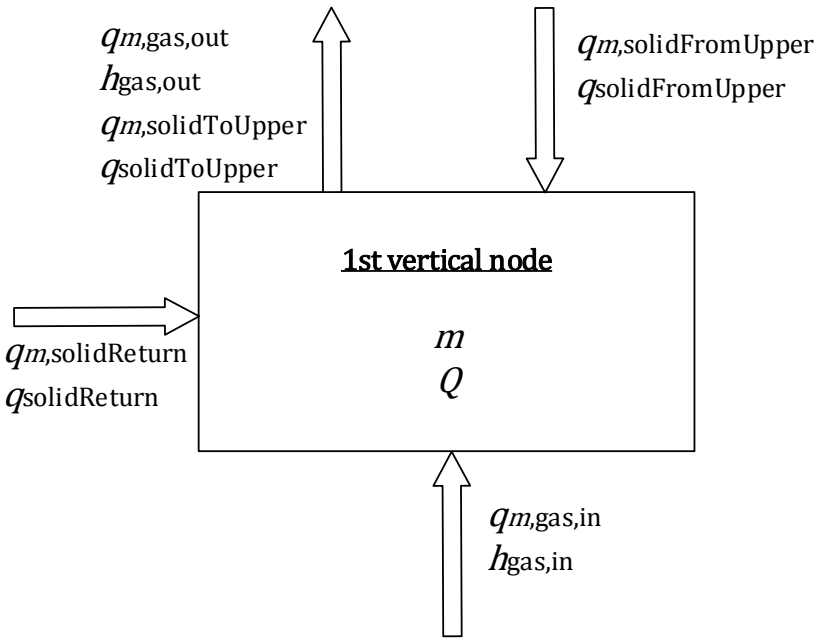

Figure 6.1. Control volume of the bottom node, simulating the high-density bed.

Simulation results can be seen in the following two figures. The simulation procedure is as follows:

1. Simulate for 5 minutes in steady state
2. Increase return solids mass flow by 0.1 % at 5 minutes.
3. Decrease return solids mass flow to 99.9 % of its original value at 15 minutes.
4. Return the mass flow to its original value at 25 minutes.
5. Increase gas mass flow by 10 % at 35 minutes.
6. Decrease gas mass flow to 90 % of its original value at 45 minutes.
7. Return gas mass flow to its original value at 55 minutes.
8. Increase gas temperature from 870 °C to 900 °C at 65 minutes.
9. Decrease gas temperature from 900 °C to 840 °C at 85 minutes.
10. Return gas temperature back to 870 °C at 105 minutes.
11. Simulate for 70 minutes without change

Figure 6.2 shows the results of equations (6.2) and (6.5), and Figure 6.3 shows the results of equations (6.4) and (6.6). The two curves in both figures follow each other well while changing the three key parameters. In paractise, they are on top of each other. The mass and energy values also return to zero at the end, when all the manipulated parameters are the same as in the start. This shows that the balances hold at the bottom bed.

The balances are in good agreement in all cases, but there is an issue when changing the fluidizing gas temperature as seen in Figure 6.3. The integrated net energy according to equation (6.4) produces some error. The Apros integrator component produces some numerical error that accumulates during the long simulation period. The error is seen best when changing the temperature at the time instances 85 minutes and 105 minutes. The error is mitigated with a smaller simulation time step. The time step used in this simulation was 0.1 seconds. The error seen in the figure comes from the integrator component, and further inspection confirmed that the heat balance is correct in the model.

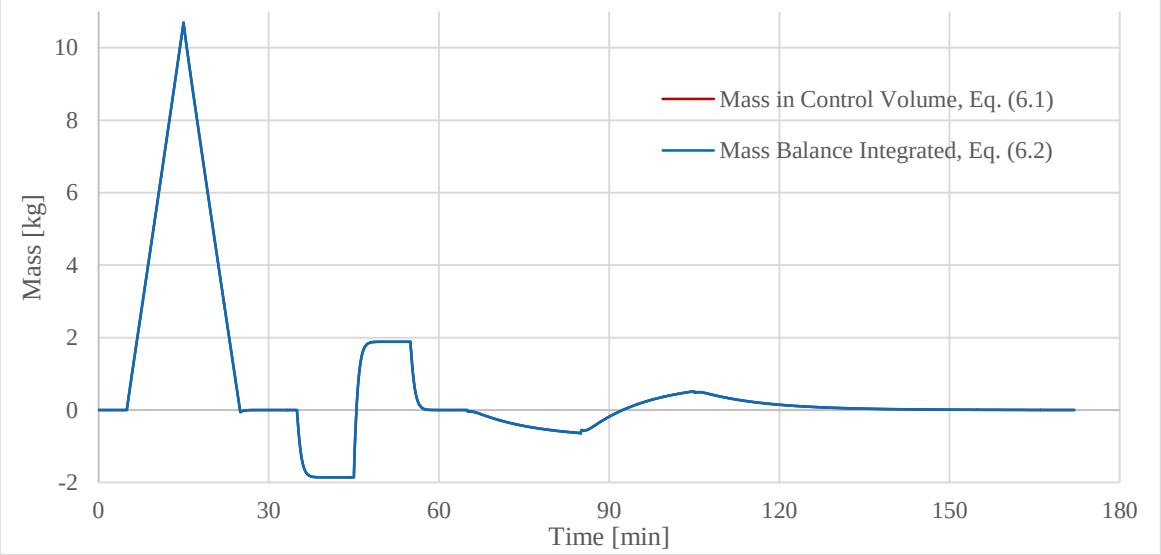

Figure 6.2. Mass balance comparison for the bottom bed.

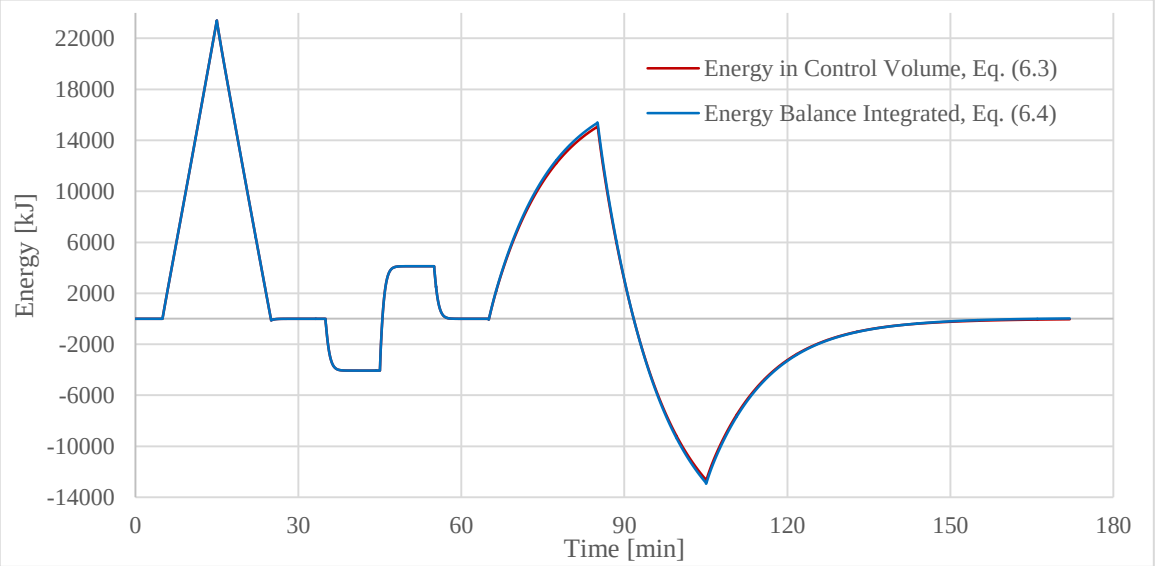

Figure 6.3. Energy balance comparison for the bottom bed.

6.1.2 Upper Part of the Furnace

For the upper furnace balance checking, a system with a boundary, as seen in Figure 6.4 was defined. The system consists of vertical nodes 2, 3 and 4 of the fluidized bed component. Each vertical node consists of a core and annulus node and a flue gas node. Regarding the vertical node 2, mass and energy flows enter the node from the bed bottom and exit the node to the bed bottom as well. From node 4, gas exits through the gas flow branch and entrained solids go to the solid inventory outside the furnace.

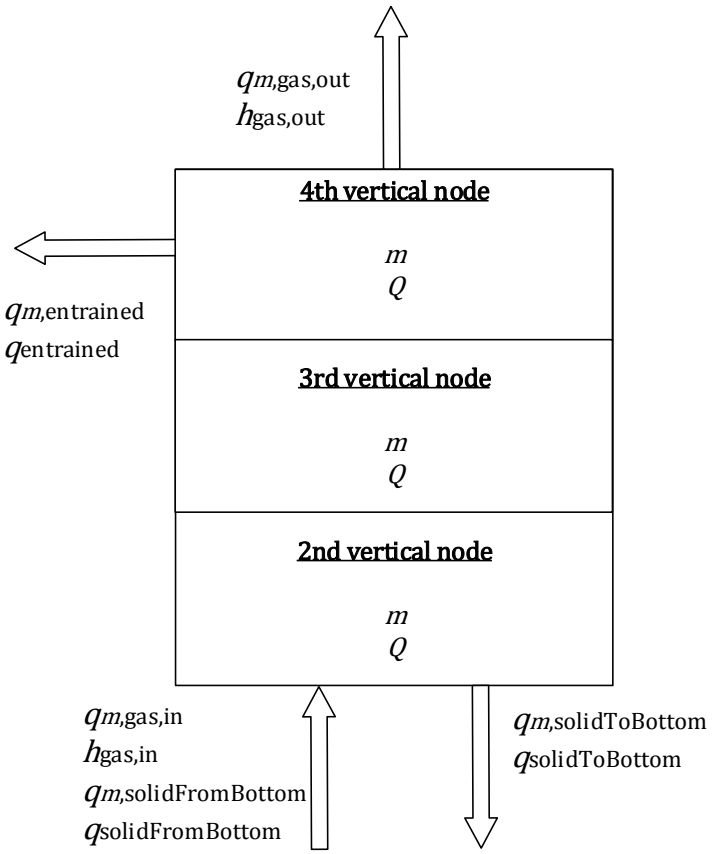

Figure 6.4. Control volume for the upper furnace.

The two figures below show the simulation results. The simulation procedure is the same as with the bottom bed. The balances are in agreement also in the upper part of the furnace.

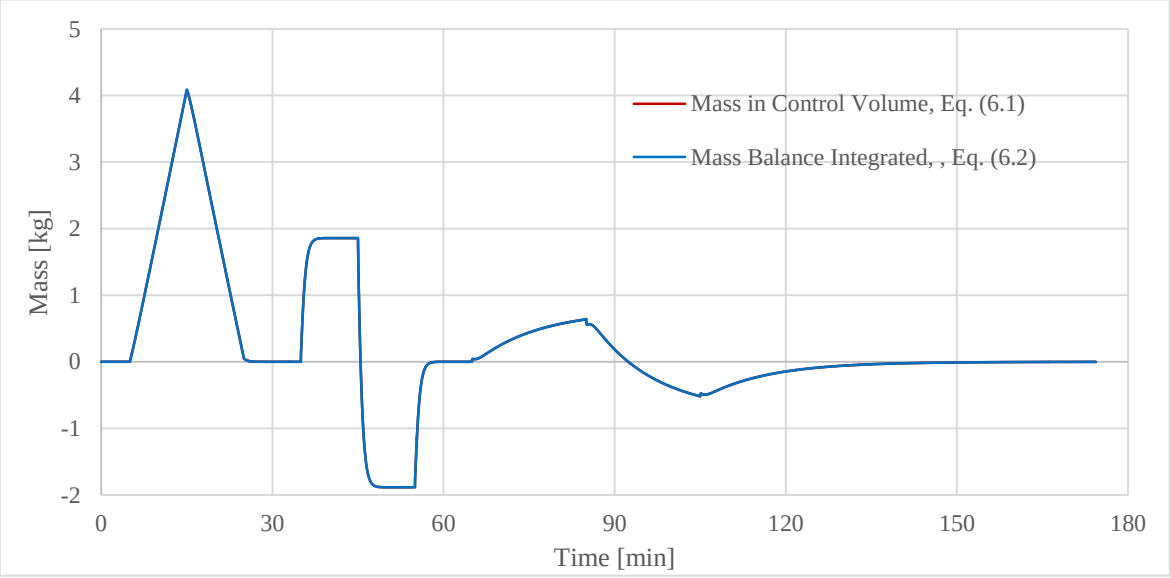

Figure 6.5. Mass balance comparison for the upper furnace.

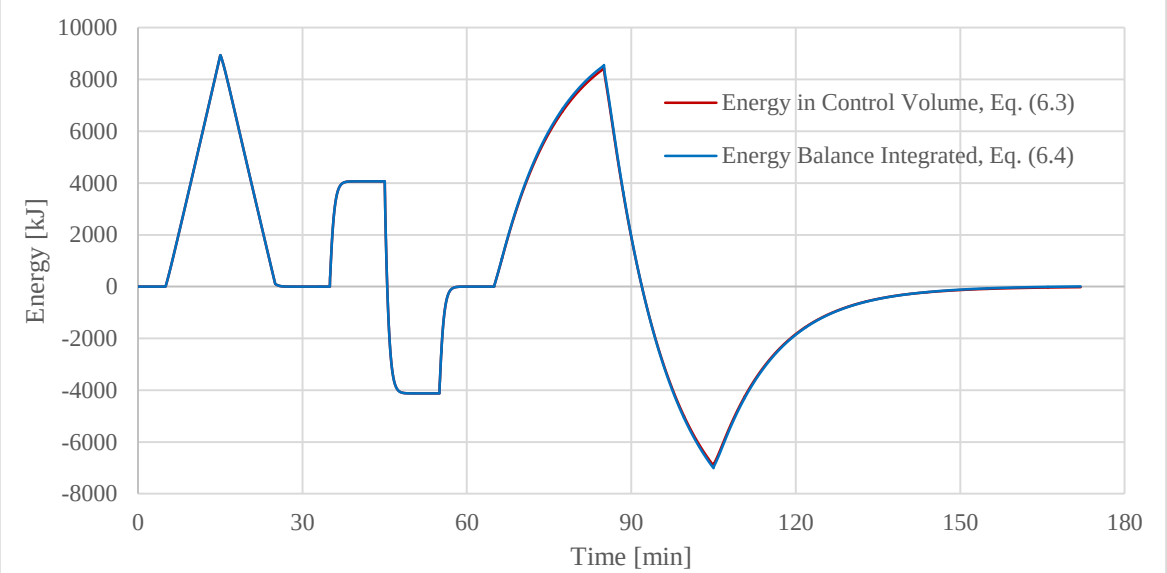

Figure 6.6. Energy balance comparison for the upper furnace.

6.2 Verification of the Hydrodynamic Submodel

Several simulation cases were planned to see how key factors in a CFB affect its operation and bed conditions. The cases aim to display that the model implementation works as it should and that transients in the model outputs behave in a reasonable way. They also provide a means to investigate if there are inconsistencies in the way the model behaves. The purpose of the cases is to verify the implementation of the model: the results do not have to be quantitatively accurate, as long as the responses to transients are physically plausible.

In most of the cases, one variable is increased at a time and then returned to its original value. Desired behavior could, for example, be that after the onset of a change in the lower part of the furnace, a certain delay is expected after which the response is seen in the upper part. The cases are shown in Table 6.1.

Table 6.1. Summary of the verification cases for the hydrodynamics submodel.

Case	Type of change	Operating condition
1	Decrease in SA feed	Normal
2	Increase and decrease in bed material feed	Normal
3	Startup and shutdown	Special
4	Immediate stop of solids recirculation	Disturbance
5	Immediate stop of fluidizing gas	Disturbance

Cases 1 and 2 explore normal operation conditions. Subjects of investigation in these two are the decreasing of secondary airflow and the increasing of bed material inventory. Case 3 examines the startup and shutdown of a CFB. Cases 4 and 5 investigate the stopping of recirculation and fluidizing gas flow, which are unusual conditions. In cases 1, 3 and 5, the mass of solids in the furnace is kept constant, meaning that the mass flows of entrained and returning solids are equal. It is a major simplification, but it should not affect the quality of the results.

Case 3 is by its nature more complicated than the other cases. The fluidization regime starts from the fixed bed, moving to the bubbling bed, then the turbulent bed and finally to the fast bed. The transition from the fixed bed to fluidization was not successful with the normal boundary conditions of the solid phase. One variable had to be controlled with normal Apros automation components.

The main parameters that are used in the case model and that are the same in all cases are presented in Table 6.2. Reactions are not modeled in these cases. The fluidizing air temperature is a constant and the value 870 °C is used so that the properties of gas are close to normal CFB conditions. The material inventory in the furnace is in the same temperature as well. Modelling parameters such as node heights and local split coefficients are given in Appendix 3.

Table 6.2. Configuration values of the CFB model that are shared between all cases.

Furnace height	41.5 m
Furnace area at grid level	123 m^2
Furnace area at 7.84 m	307.4 m^2
Secondary air injection height	7.5 m
Fluidizing air temperature	870 °C
Particle diameter	250 μm
Particle density	2 400 kg/m^3
Particle sphericity	0.8
Total mass of particles in system	190 000 kg
Fluidizing gas	Air

The model used in the cases is almost the same in all cases. For all cases but the one investigating startup and shutdown, the fluidizing gas mass flow is a boundary condition.

Also, the furnace pressure is controlled by changing the back pressure with a boundary condition.

Case 3, investigating startup and shutdown, is fundamentally more complicated than the other cases and requires some additions. In case 3, the primary air (PA) mass flow is controlled by linearly opening and closing a control valve. This was needed as the operation point during startup and shutdown changed dramatically. For this reason, the PA mass flow curves in the other cases are straight and in the case of startup and shutdown its gradient varies. In addition, the furnace has pressure control automation. The second node is kept at 1.05 bar of absolute pressure. In the case of startup and shutdown, the pressure is controlled with a control valve in the flue gas duct.

6.2.1 **Case 1. Change in Secondary Air Feed**

It is important to see how the model behaves with varying secondary air (SA) flow, as air feed, and therefore gas velocity, has a large impact on bed hydrodynamics. SA is used to optimize combustion in a CFB, and residue oxygen in the flue gas is controlled mainly with SA. Also when the boiler load is changed, the SA feed is altered more than the PA feed. Therefore, only SA feed is changed in this case.

The results in this case are obtained by controlling the value of the split coefficient α, introduced in Eq. (5.8). The coefficient values were made directly proportional to the SA mass flow and are presented in Figure 6.7. During this test it was found that the selected model approach cannot simulate this case using a constant split coefficient α. If the coefficient is not adjusted, the bottom bed density decreases and upper bed density increases, which is the opposite of what is expected to happen in a real process. The comparison with and without adjusting the coefficient is shown in Figure 6.9 and Figure 6.10. This is because the velocity of solids flowing from core to annulus, shown in Eq. (5.26) and (5.27) are almost constant, as well as the split coefficients, regardless of the fluidizing air velocity. In reality, if the fluidizing gas velocity is decreased, there is less force lifting the particles upward. Therefore, the particles have more time to drift to the annulus while moving up, increasing the suspension density lower in the furnace and decreasing it in the upper furnace. The Apros CFB model does not take into account this kind of physical phenomenon. Hence, it has to

be corrected with either increasing the annulus zone velocity, which is equal to the radial velocity of solids, or the split coefficients. There is no basis on increasing the annulus zone velocity, because decreasing the fluidizing gas flow does not necessarily increase the downward velocity of solids in the annulus. Therefore, in this case, the global split coefficient α was used. This issue is further discussed in Chapter 7.

Table 6.3 contains initial values used in case 1. The total fluidizing air mass flow is 500 kg/s with a PA ratio of 40 %. In the upper parts of the furnace this accounts to a gas velocity of roughly 5.3 m/s. The gas velocity profile in the furnace is shown in Figure 6.12.

Table 6.3. Initial values used in case 1 in addition to those presented in Table 6.2.

Mass flow of primary air	200 kg/s
Mass flow of secondary air	300 kg/s
Fluidizing air velocity	5.3 m/s
Solids concentration at furnace exit	4.0 kg/m^3
Mass flow from bottom node	14 750 kg/s
Internal circulation mass flow	10 200 kg/s
External circulation mass flow	4 550 kg/s

In the simulation, the SA feed is decreased in five steps from 300 to 200 kg/s. Each step lasts 5 minutes, and the rate at which SA is decreased is 10 kg/s per minute, shown in Figure 6.7. The system is driven to a new steady state in each step.

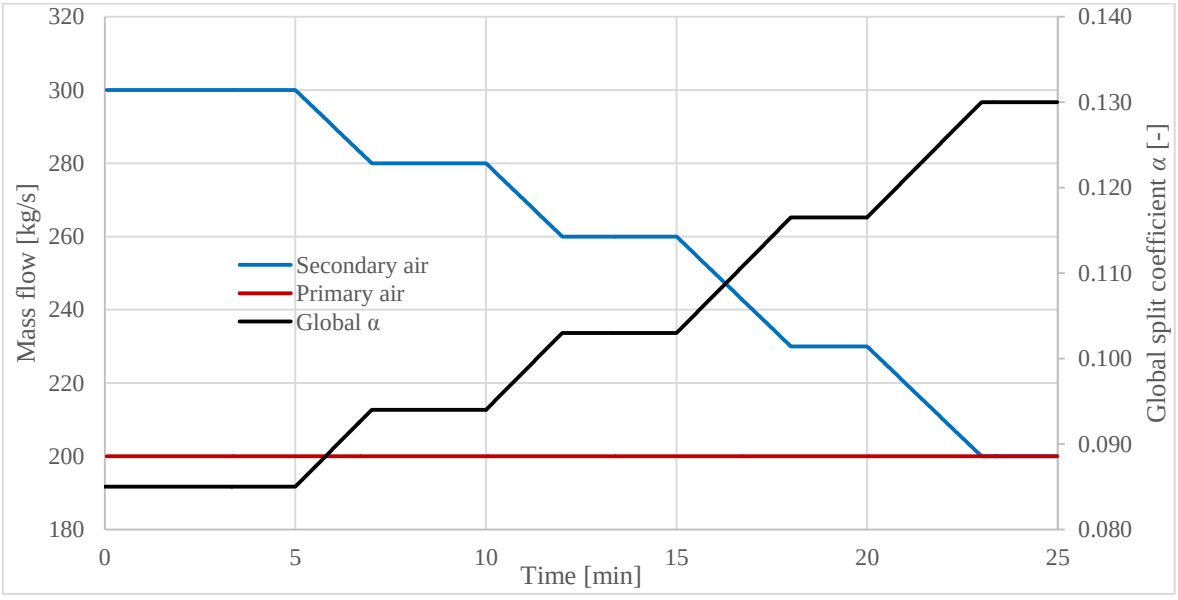

Figure 6.7. Case 1: change in SA feed. PA and SA mass flows and global split coefficient α.

Figure 6.8 shows a comparison of three important solid mass flows in the CFB model: mass flow leaving the bottom node, external circulation and internal circulation. External circulation is the mass flow of particles leaving the furnace and returning to the bottom node, which in these cases are equal. Internal circulation is the mass flow of particles returning to the bottom node from the annulus layer. The variables are biased so that only their changes to the initial state are shown. The initial values for the mass flows are shown in Table 6.3.

The mass flow leaving the bottom node experiences only minor changes, decreasing by 1.5 % at its minimum compared to its initial value. The mass flow from the bottom node decreases only because the air velocity in the bottom node decreases, due to an increased pressure drop across the bottom node. The external and internal circulation rates change more intensely, the external circulation decreasing by 61 % and the internal circulation increasing by 25 % compared to their initial values. The external circulation mass flow decreases, as with a decreased fluidizing gas flow, both the suspension density and gas velocity at the top of the furnace, affecting entrainment, are also decreased, Figure 6.9. Consequently, as fewer particles are entrained while the mass flow leaving the bottom node is relatively unchanged, the internal circulation increases.

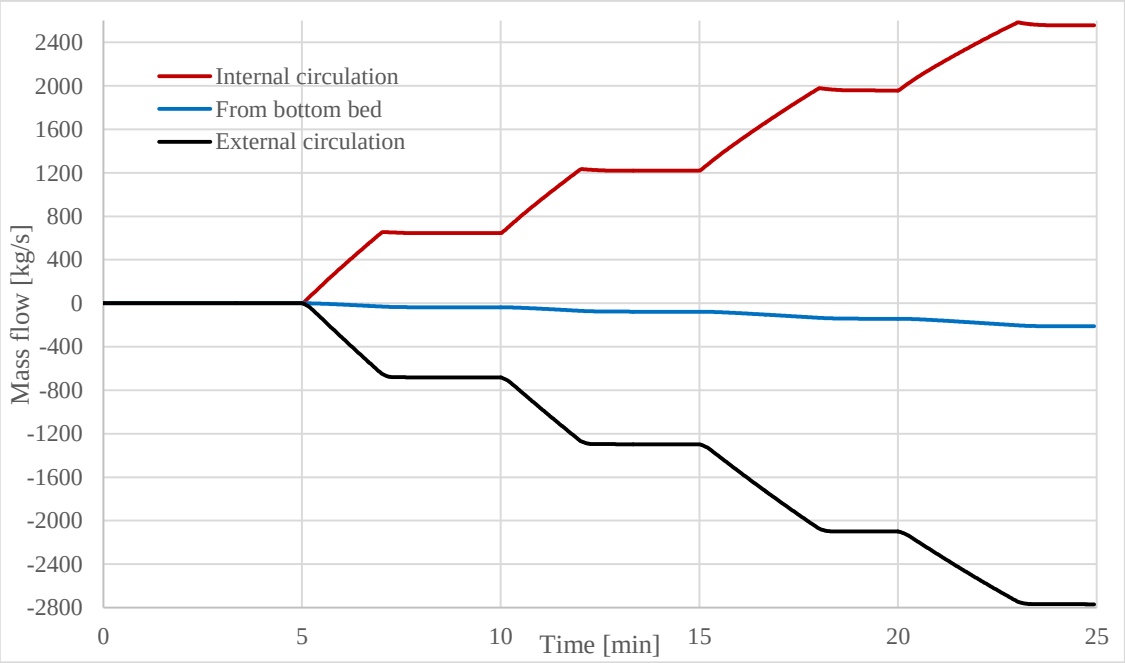

Figure 6.8. Case 1: change in SA feed. Comparison of the changes in different mass flows in the furnace. The mass flows are scaled so that the changes compared to the initial state are seen.

Figure 6.9 shows the progression of the average vertical suspension density profile during the simulation, with different SA mass flows. Each profile is obtained from a steady state. The figure shows that when the secondary airflow is decreased, the suspension density and bed height of the bottom bed increase. The bed height is seen from the height where the suspension density is still constant. The suspension density of the upper furnace decreases instead as SA flow decreases. These results are obtained by tuning the global split coefficient α. The suspension densities in the case that the split coefficient was not tuned, is shown in Figure 6.10. From these two figures it is seen that without tuning the suspension densities go to the opposite, unrealistic direction.

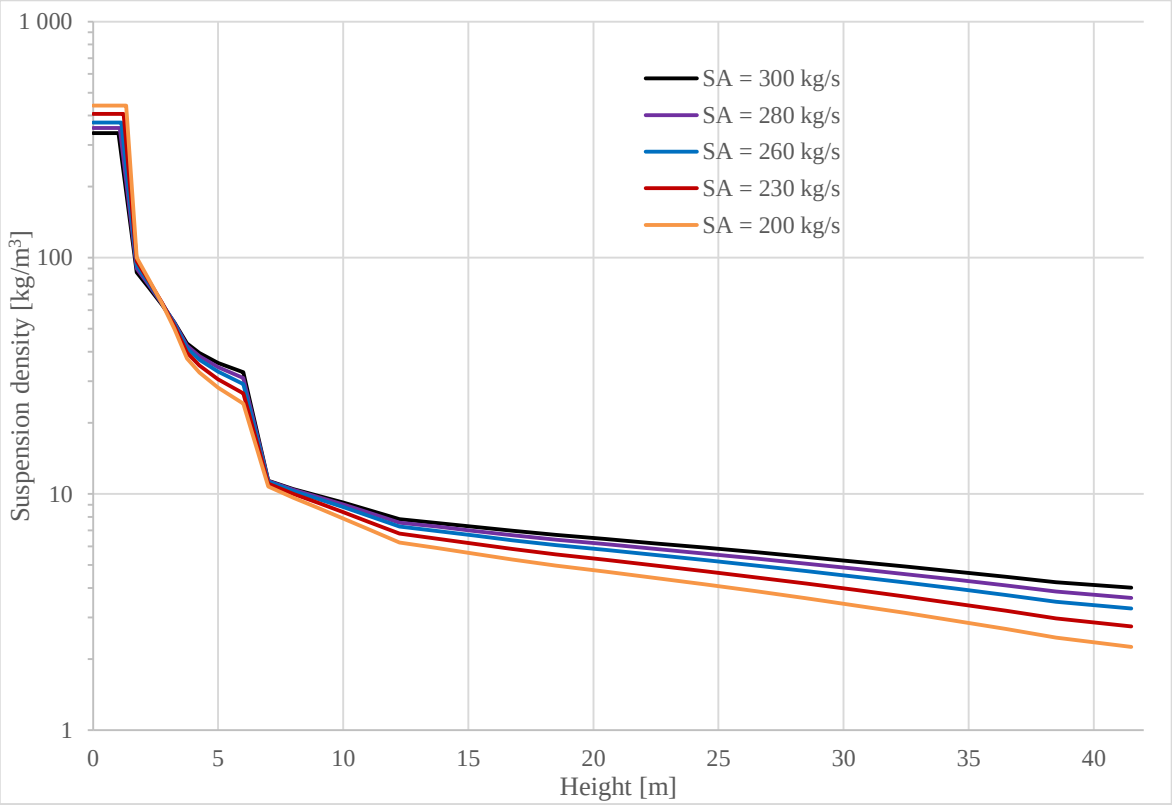

Figure 6.9. Case 1: change in SA feed. Average suspension density in relation to furnace height, with different SA mass flows. The curves are obtained from steady states.

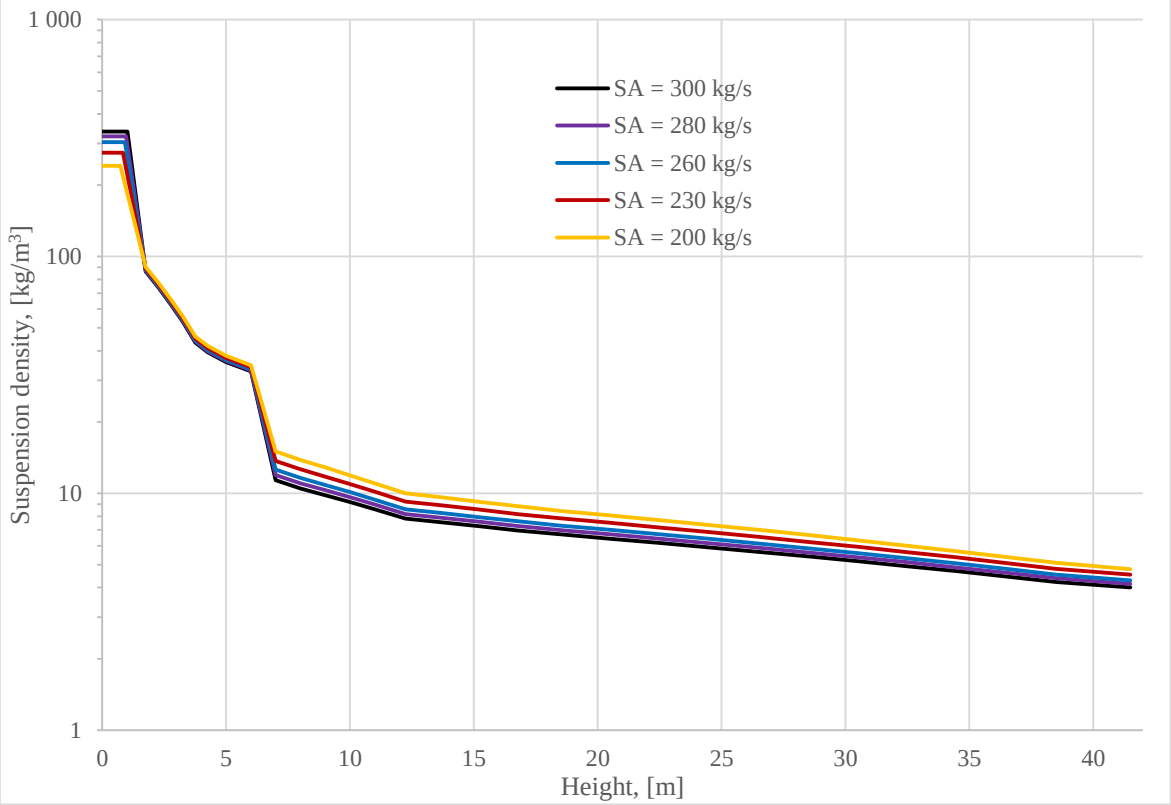

Figure 6.10. Case 1: change in SA feed. Alternative simulation without the tuning of the global split coefficient α. Progression of average suspension density in relation to furnace height, when secondary airflow is decreased. The curves are obtained from steady states.

Figure 6.11 shows how the suspension density at the top of the furnace behaves during the simulation experiment. The suspension density follows the changes in the SA feed very closely, with only little delay between the onset of change and the response. The figure shows that the changes in suspension density occur steadily which is desired behaviour of the model.

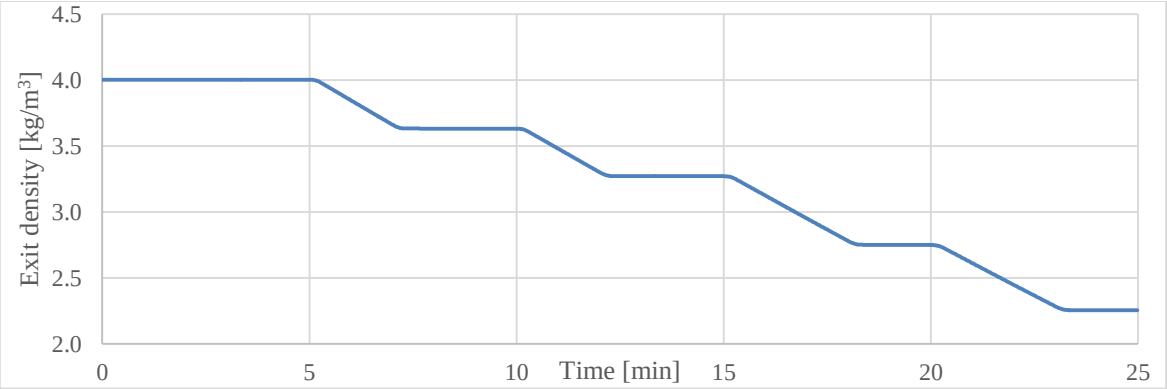

Figure 6.11. Case 1: change in SA feed. Suspension density at the top node of the furnace.

Figure 6.12 shows gas velocities in the furnace as a function of furnace height, and how they change during the simulation. The gas velocities remain roughly unchanged between the bottom node and the SA injection, after which they change heavily as the SA feed is decreased. Up until approximately 8 meters, the furnace is tapered, meaning that the cross-sectional area of the furnace increases with height. The effect of the tapering is seen as a general decreasing of the fluidizing gas velocity up to 8 meters, disrupted only by the SA injection. After the tapered section, the gas velocities remain relatively constant.

The solid phase affects the gas velocities only by pressure losses, as discussed in Chapter 5.6.1. After the tapering of the furnace ends, the gas velocities become relatively level, but increase by a small amount to the top of the furnace. The velocities increase due to the pressure losses from the solid phase becoming smaller with increasing height. In reality, also the space taken by the particles have an effect on the gas velocities. As there are less particles higher in the furnace, the flow area of gas becomes larger, therefore decreasing the gas velocity. As gas velocity is one of the most important factors contributing to bed hydrodynamics, this aspect should be included in the future development of the model.

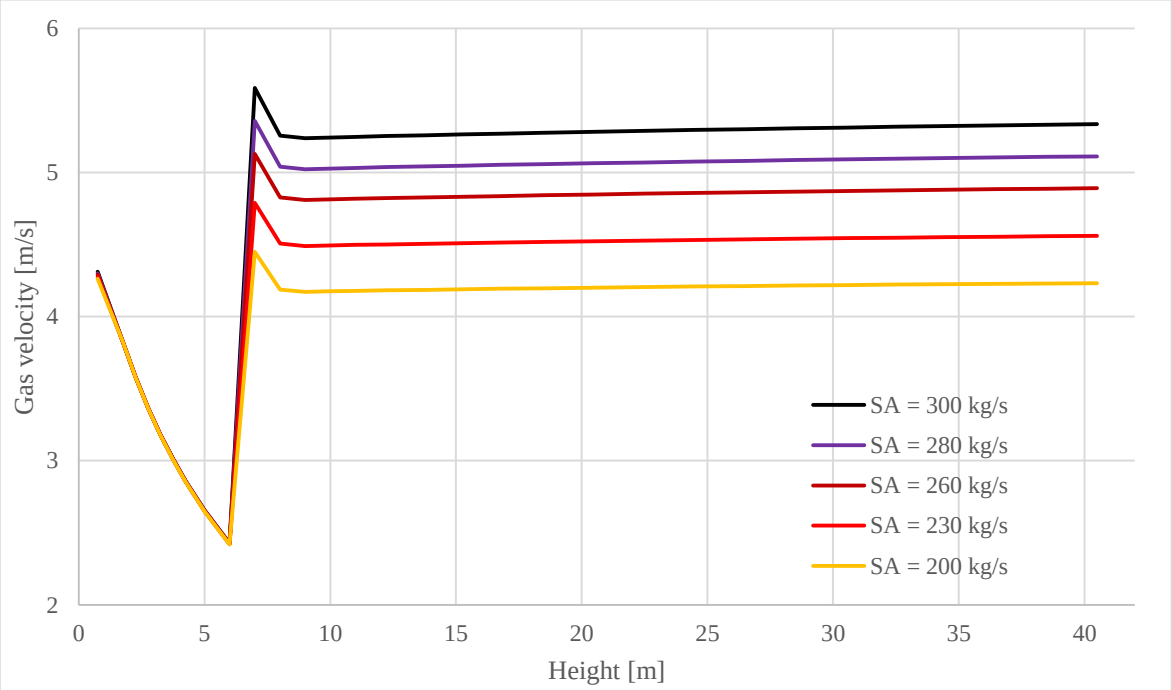

Figure 6.12. Case 1: change in SA feed. Gas velocities in relation to furnace height, when the secondary airflow is decreased. The curves are obtained from steady states.

6.2.2 Case 2. Change in Bed Material Inventory

One of the biggest downsides of the previous Apros CFB model concerned changes in the bed material inventory. Adding new bed material into the bottom furnace had an unrealistically large effect on the material inventory in the upper furnace. In reality, modest changes to the bottom bed inventory should not have a large effect on the material inventory in the upper furnace. Therefore, this case is important in validating the new model and for showing that the new model mimics the real world process better than the previous one.

In the CFB model, the two factors influencing solid outflow from the bottom node are gas velocity and the interface density which is normally a constant value. Therefore, a change in the bottom node mass has an effect on the upper furnace mass only through decreasing or increasing gas velocity in the node. Hence, the upper furnace should see only minor changes in terms of hydrodynamics in this case.

Table 6.4. Initial values used in case 2 in addition to those presented in Table 6.2.

Mass flow of primary air	200 kg/s
Mass flow of secondary air	360 kg/s
High-density bed mass	69 798 kg
Upper furnace mass	120 201 kg
Mass flow from bottom node	18 199 kg/s
Internal circulation mass flow	14 163 kg/s
External circulation mass flow	4 036 kg/s

In this case, bed mass was increased from 190 000 kg to 208 000 kg in one hour, starting from 5 minutes, and then back to 190 000 kg in one hour, starting from 75 minutes. The feed mass flow and its effects on high-density bed and upper furnace masses is shown in Figure 6.13. The values are scaled and their initial values are found in Table 6.4. The upper furnace mass experiences only mild changes, decreasing by roughly 1 % at its minimum compared to its initial value. The high-density bed mass experiences a larger change, being roughly 28 % more than initially, at its maximum.

Figure 6.13 shows the simulation results. The results show that the bottom bed mass increased more than the 18000 kg that was fed into the furnace, by receiving additional material from the upper furnace. The increased mass in the bottom bed causes a larger pressure drop, increasing the gas pressure, Figure 6.14. Increased pressure means higher gas

density and therefore lower gas velocity, as gas mass flow is kept constant. A lower gas velocity results in decreased mass flow of particles to the upper furnace. As more material remains in the bottom bed, the upper furnace mass decreases slightly.

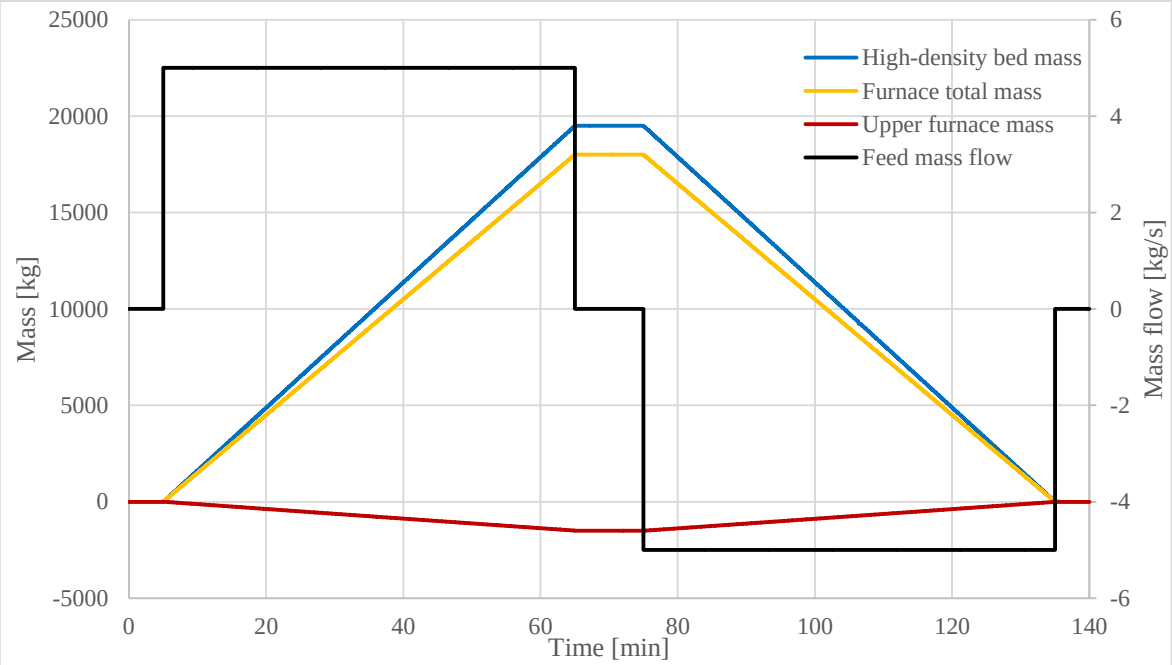

Figure 6.13. Case 2: Change in bed material inventory. Feed mass flow and changes in furnace masses. The masses are biased to illustrate the changes with respect to the initial states.

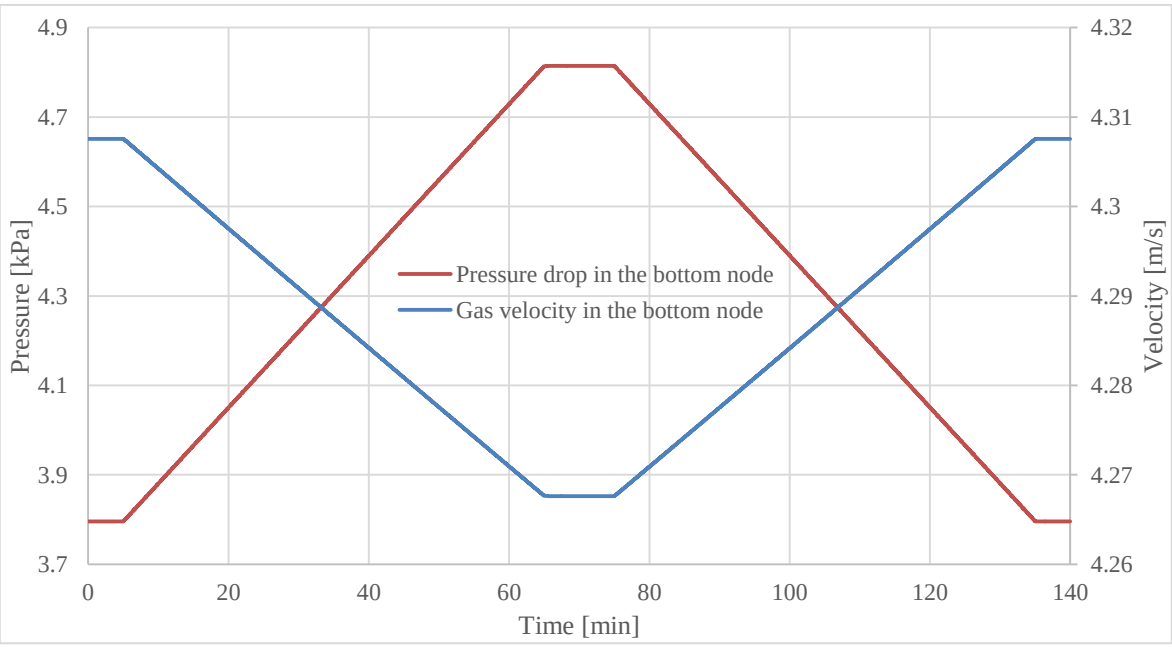

Figure 6.14. Case 2: Change in bed material inventory. Pressure drop and gas velocity in the bottom node.

Figure 6.15 shows the changes in the three solids mass flows, similar to case 1. Their initial values are found in Table 6.4. The results show that the mass flow leaving the bottom node indeed decreases more than the internal circulation, causing the additional increase in high-density bed mass and an equal decrease in the upper furnace. As less solids leave the bottom bed, also the external circulation experiences a decrease.

In reality, when material is added to the furnace, the new material increases particle concentration locally. Therefore, the flow area of gas decreases locally, and the velocity of gas consequently increases. This transports material higher in the furnace, increasing external circulation. As a result, the material inventory in the feed point decreases and finally a new steady state is reached. The current CFB model gives unrealistic results, as it does not take into account the flow-area-decreasing effect of the particles. In addition, assuming the interface density as constant may add to the results being unrealistic. The adding of new material to the furnace is therefore a subject of future development. Nevertheless, the results are much more realistic than in the previous CFB model.

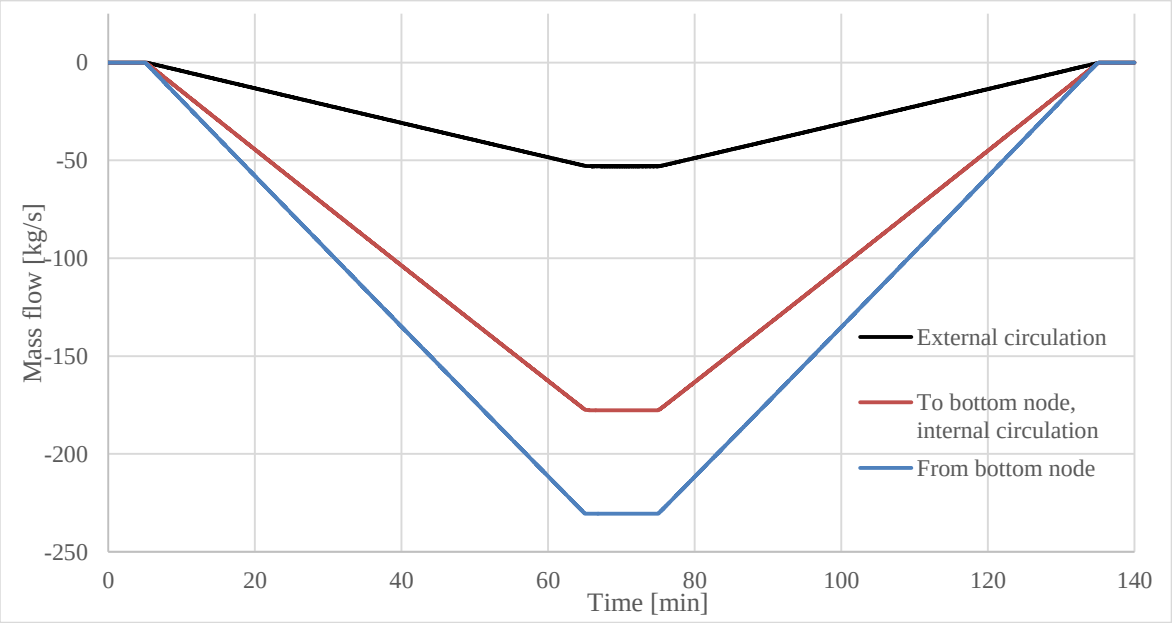

Figure 6.15. Case 2: Change in bed material inventory. Comparison of the changes in different mass flows in the furnace. The mass flows are scaled so that the changes compared to the initial state are seen.

Figure 6.16 shows how the average suspension density along the furnace height changes when the bed mass is increased. The previous figures show that the bottom bed mass

increases considerably while the upper furnace mass slightly decreases. This shows in the suspension densities as well. The suspension densities in the bottom bed increase whereas there are no notable changes in the suspension densities in the upper furnace.

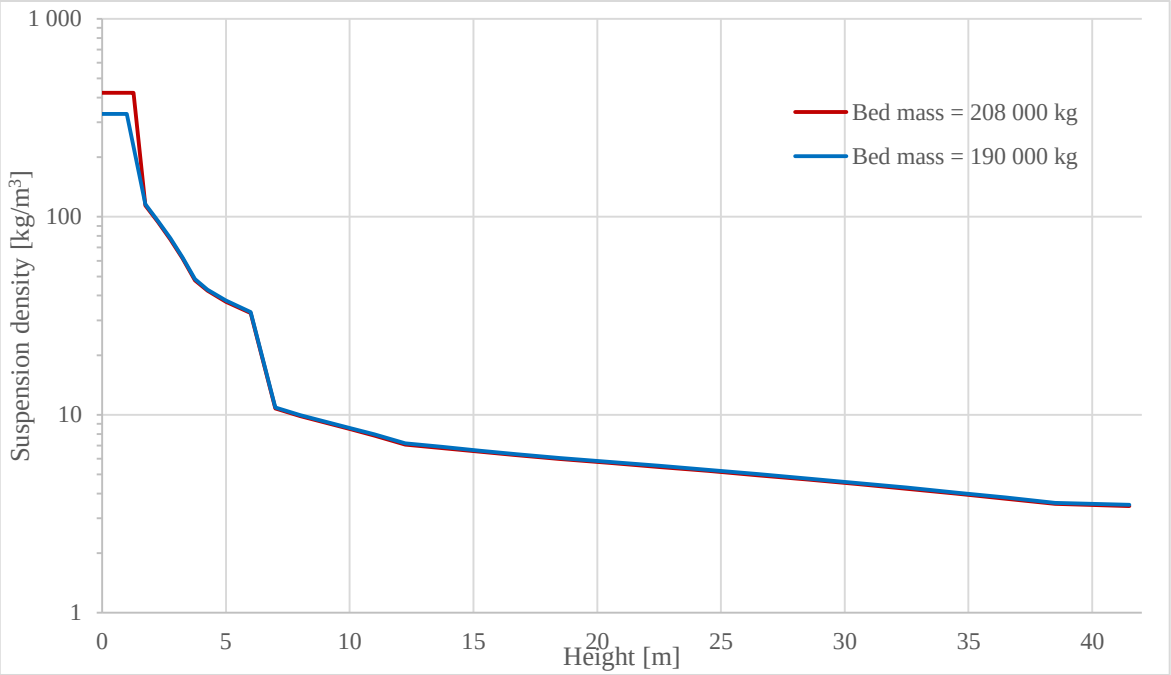

Figure 6.16. Case 2: Change in bed material inventory. Average suspension density in relation to furnace height, when the bed material feed is increased. The results are obtained from steady states.

6.2.3 Case 3. Startup and Shutdown

The desired scope of operation of the CFB model includes the startup and shutdown of the furnace, and here the topic is addressed from a hydrodynamic perspective. The simulation of startup and shutdown operations are a subject of further investigation and development, outside the scope of this thesis.

When increasing the PA feed, starting from zero, the fluidizing gas starts dragging bed material higher in the furnace. Startup and shutdown should both go smoothly without unexpected behaviour in the solid phase. In this case, only PA is used, because the objective is to demonstrate that the model is able to simulate the startup from fixed bed to fluidization and shutdown without problems. For this purpose, SA is not needed.

In the other cases, the particle diameter is 250 µm. In this case, however, the particle size was lowered to 150 µm. With the bigger particle size, the terminal velocity of particles was much bigger, so particles started moving up from the bottom node at much larger gas velocities. This let the bottom bed height, introduced in Chapter 5.5.3, rise higher than the bottom node height, causing problems in the simulation. By decreasing the particle size, particles left the bottom node at smaller velocities, and the problem was mitigated.

Even with the smaller particle size, the bottom bed height rose too high, although to a lesser extent. For this reason, a new attribute was designed solely for the startup and shutdown of the furnace. The attribute is an artificial velocity term to all core node velocities, as was presented in Chapter 5.6.2. The current model does not include particle size distribution and thus assumes average particle size. In reality, the smaller particles help in starting the fluidization earlier and in making the transitions between regimes smoother. The new variable was introduced to imitate this behaviour. By using this additional attribute, the startup and shutdown could be simulated, yielding plausible results.

Figure 6.17 shows the PA mass flow during the simulation. The PA feed is zero for the first five minutes, after which the PA valve is slowly opened, and the startup is initiated. The PA mass flow increases with a gradient of 10 kg/s/minute until 20 minutes, after which the flow levels. At 35 minutes, the process is reversed, and shutdown is initiated.

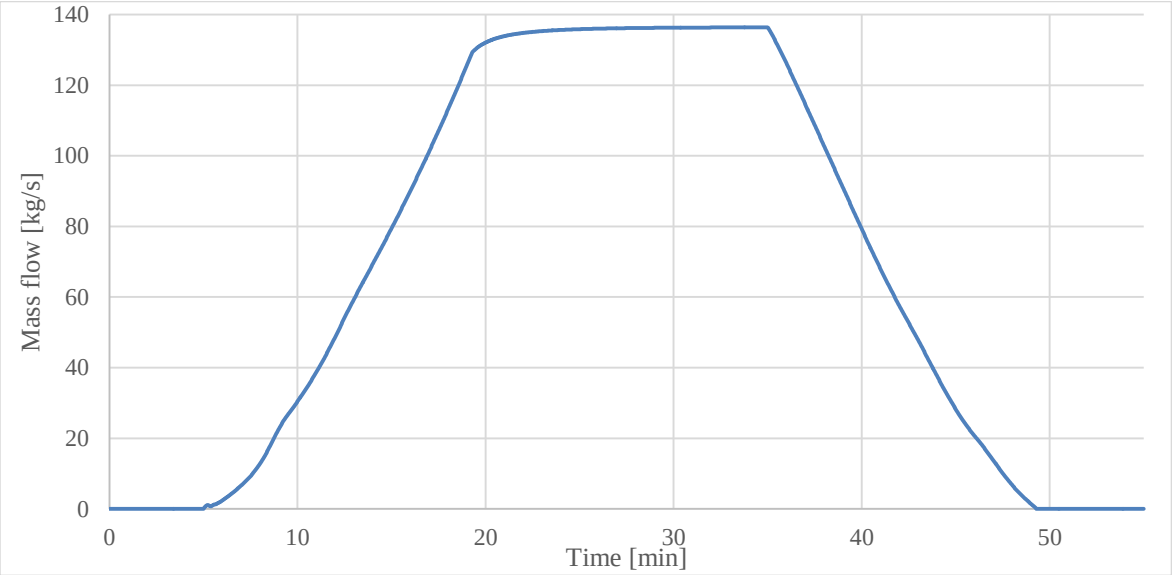

Figure 6.17. Case 3: Startup and shutdown. Mass flow of primary air.

Figure 6.18 presents important solids mass flows in the furnace during the simulation. It is seen that the mass flow from and to the bottom node increase from the moment the PA feed is increased. For the first three minutes, the mass flows from and to the bottom node rise with no effect in the external circulation. The mass flow from the bottom node rises faster, meaning that the solid inventories in the higher nodes increase. All mass flows increase as a function of PA feed and relatively smoothly, as is desired. However, the smooth results are achieved with the help of the attribute solids startup velocity. Its values, alongside the gas and solid velocities of the first node, are shown in Figure 6.19. The startup velocity is controlled as directly proportional to the PA feed, capping at 1 m/s for PA mass flow of 20 kg/s. The gas velocity does not have an effect on the solid velocities until at 9.5 minutes. Until this point, the solid velocities are equal to the solids startup velocity. At this time instance, the gas velocity exceeds the terminal velocity of the particles and the gas velocity also starts to affect the velocity of the particles.

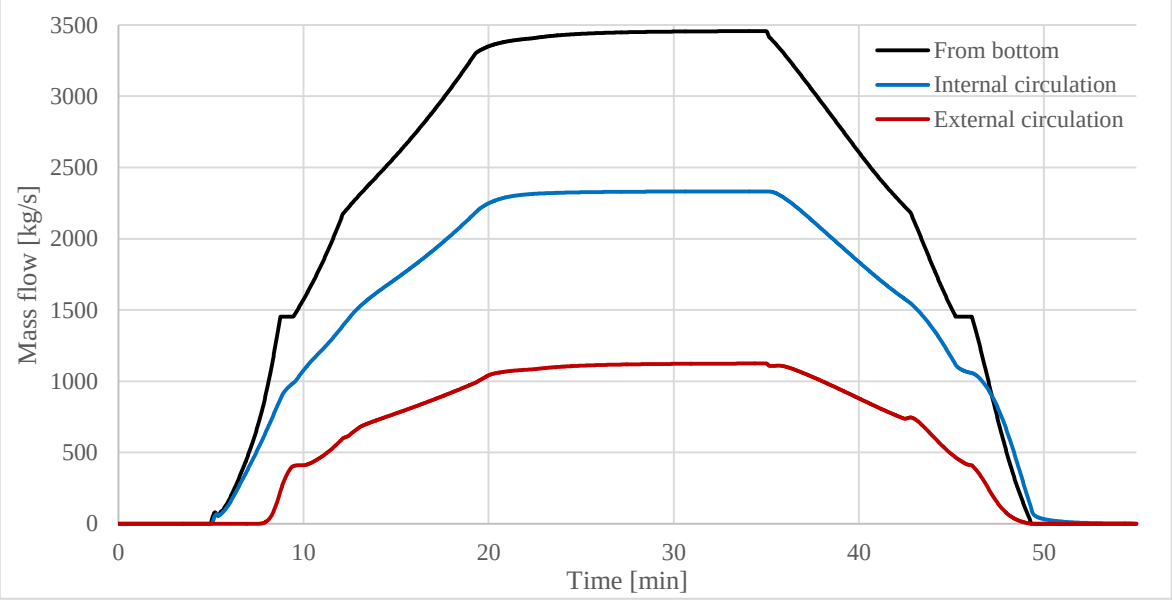

Figure 6.18. Case 3: Startup and shutdown. Different solids mass flows in the furnace.

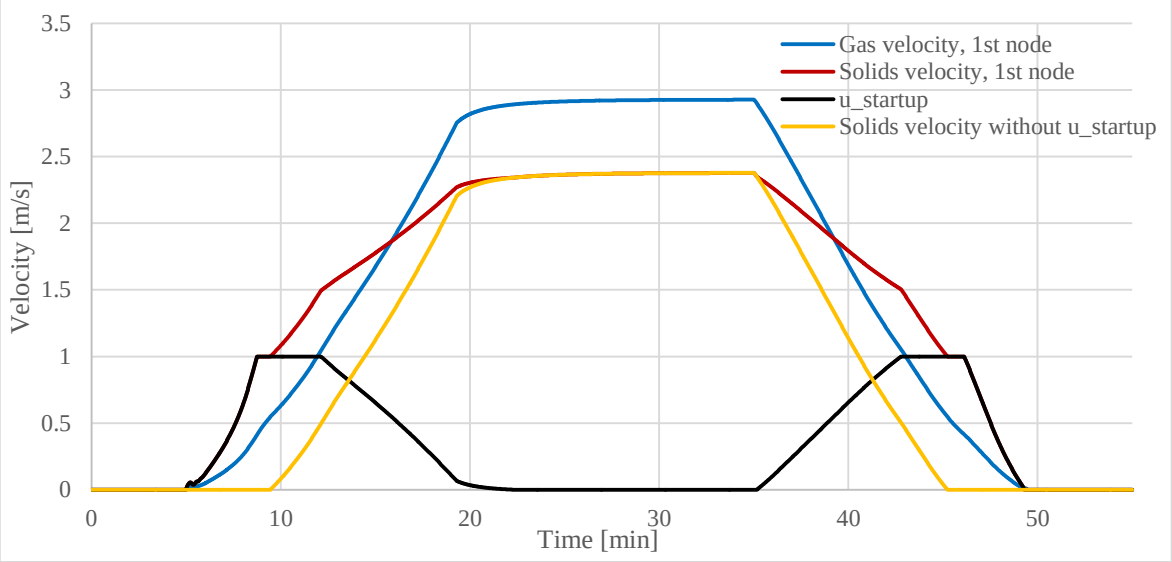

Figure 6.19. Case 3: Startup and shutdown. Gas and solid velocities in the first node and the solid extra velocity used for all nodes.

Figure 6.20 displays the pressure drop in the bottom node during the simulation. The pressure is 0 kPa, when PA feed is zero and increases by over 10 kPa, when the PA valve is opened. There is some oscillation in the pressure drop, when the valve is opened. This derives from the equation of pressure drop for the first node, as it experiences a drastic change when the feeding of air is initiated. However, this oscillation is acceptable, because it appears only in this special case and does not have a large effect on the soundness of the model behaviour. As material leaves the first node, the pressure drop decreases until it reaches a steady value when the PA feed levels.

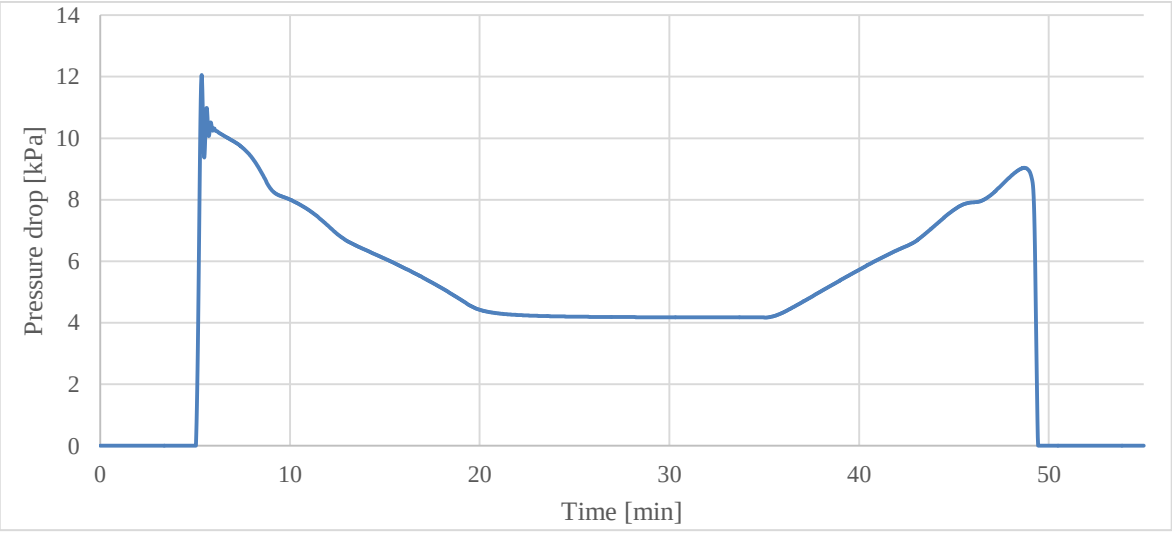

Figure 6.20. Case 3: Startup and shutdown. Pressure drop in the first node.

6.2.4 Case 4. No Recirculation

The fourth case investigates the behaviour of the model, when the mass flow of returning solids is stopped. When the entrained solids are not fed back to the bottom of the bed, the mass of solids in the furnace should deplete and become zero after some time. This case investigates the limits of the model. In reality, a boiler trip, including PA fan trip would have been caused, leading to the situation in case 5. The initial values are presented in Table 6.5.

Table 6.5. Initial values in case 4 in addition to those presented in Table 6.2.

Mass flow of primary air	200 kg/s
Mass flow of secondary air	360 kg/s
Fluidizing air velocity	5.9 m/s
Solids concentration at furnace exit	4.0 kg/m^3
Mass flow from bottom node	14 750 kg/s
Internal circulation mass flow	10 200 kg/s
External circulation mass flow	4 550 kg/s

Figure 6.21 displays simulation results of case 4. The system is at steady state, until the mass flow of returning solids is stopped at 60 seconds. As the solids are no longer returned back to the bottom node, the solids inventory in the bottom node immediately starts to deplete, leading to the dropping of the bed height. Normally, the interface density, contributing to the mass flow from the bottom node, is constant. However, in this special case, when the bottom bed inventory is quickly depleted, the mass flow from the bottom node cannot be assumed as relatively constant, as with normal conditions. Therefore, the interface density is controlled as a function of the bottom node suspension density. Figure 6.22 shows the values of the bottom node suspension density and corresponding values of the interface density during the simulation. By comparing Figure 6.21 and Figure 6.22 it can be seen that the bed height and mass flows have a very similar curve as the interface density.

Because the solids inventory in the bottom node decreases, the pressure drop caused by the bed decreases, causing the bottom node pressure to decrease. As the mass flow of fluidizing gas is kept as constant, this results in an increased gas velocity in the bottom node, as seen in Figure 6.23. An increased gas velocity increases the solids mass flow leaving the bottom node during the first 10…15 seconds. Consequently, the mass flow of internal circulation and, with a delay, also the mass flow of entrained solids increase after the onset of change.

The mass flows increase until the suspension density in the bottom node deplete to a low enough level. After this, the interface density is automatically lowered as a function of suspension density in the bottom node, with a simple control logic. When the interface density is decreased, the mass flows experience a sudden drop in values, converging towards zero. The flow-area-decreasing effect of particles is not included in the current CFB model, so the velocities of particles could behave differently in reality. However, macroscopically, the results seem plausible.

In this case, it takes approximately 3 minutes for the furnace to become almost completely emptied of bed material. This time span is influenced by the interface density and the split coefficients used in the model. They can be modified during simulation to make the results more realistic. Nonetheless, the results seem physically plausible.

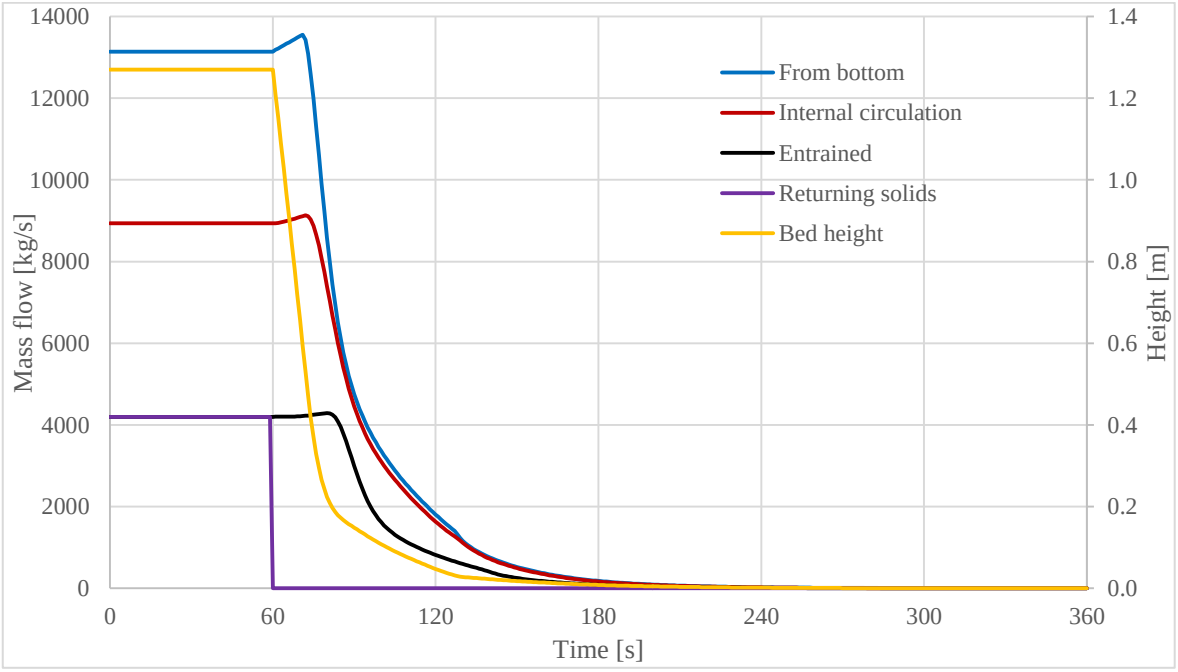

Figure 6.21. Case 4: No recirculation. Important solids mass flows of the furnace and the bottom bed height.

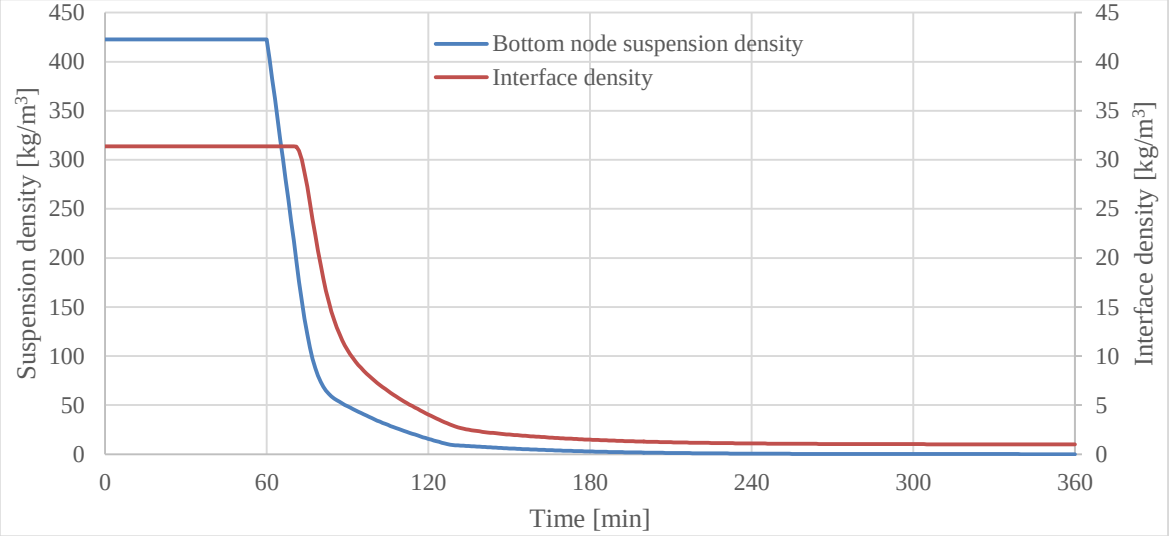

Figure 6.22. Case 4: No recirculation. Suspension density at the bottom node and the corresponding value of the interface density.

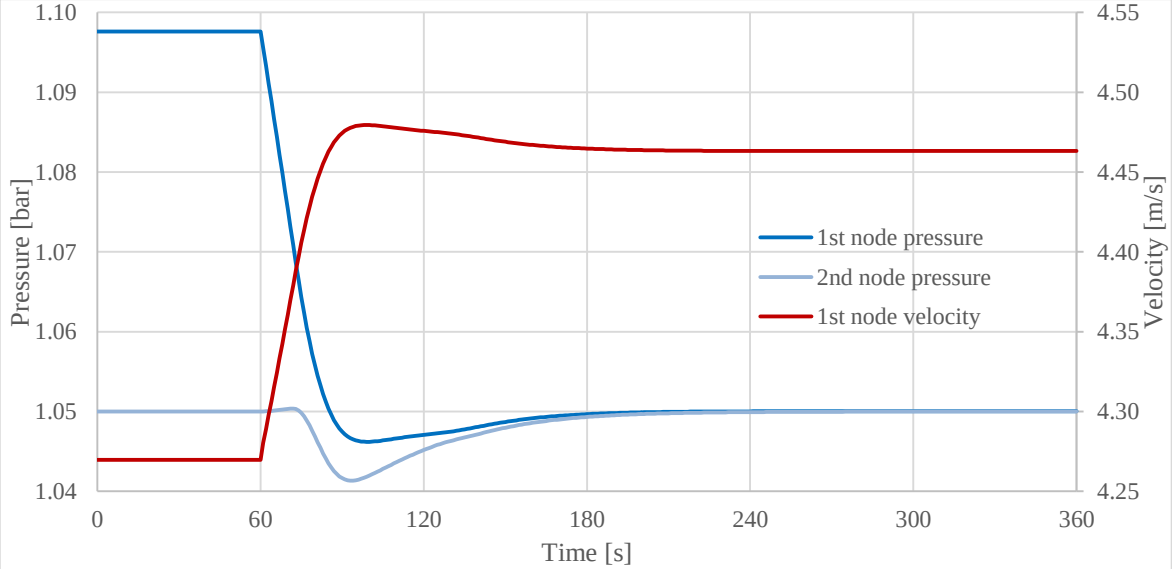

Figure 6.23. Case 4: No recirculation. Bottom node gas velocity and pressures of the first two nodes. The effect of the pressure control in the second node is seen, as the pressure is driven back to 1.05 bar.

Figure 6.24 shows the vertical average suspension density profile in the furnace during the simulation. Suspension density in the bottom node decreases steadily after the flow of returning solids is stopped. Suspension density in the upper furnace remains relatively unchanged for the first 15 seconds after the change and then starts to drop as well, when interface density is decreased. The suspension density profiles also seem physically plausible.

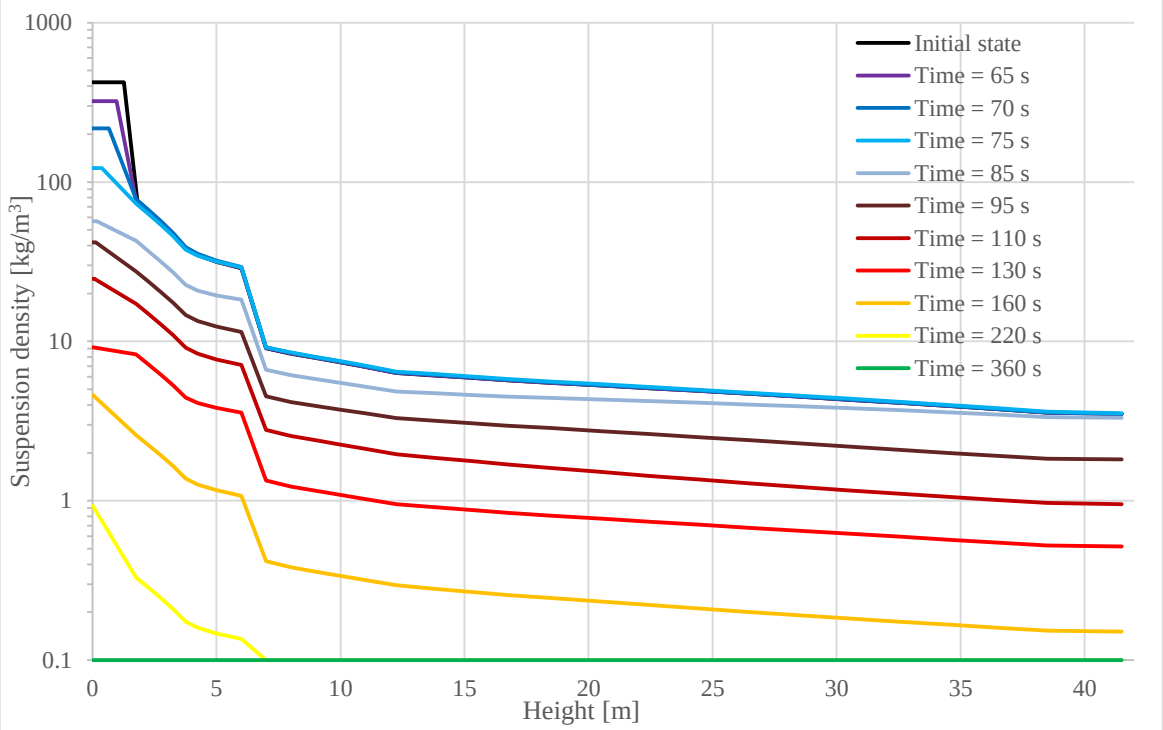

Figure 6.24. Case 4: No recirculation. Progression of average suspension densities in the riser with relation to height. The profiles are from a transient state. To make the results stand out in the figure, all values below 0.1 have been rounded up to 0.1.

6.2.5 Case 5. Sudden Stop in Primary Air Feed

In the fifth case, the fluidizing gas flow is stopped instantly. This should cause a sudden collapse of the bed, all of the bed material in the upper furnace falling into the first node. The bed is fluidized with only primary air. The initial values are presented in Table 6.6.

Table 6.6. Initial values used in case 5 in addition to those presented in Table 6.2.

Mass flow of primary air	250 kg/s
Fluidizing air velocity	2.7 m/s
Solids concentration at furnace exit	4 kg/m^3
Cluster velocity constant from Eq. (5.19)	4.0
Mass flow from bottom node	15 220 kg/s
Internal circulation mass flow	13 660 kg/s
External circulation mass flow	1 567 kg/s

In this case, the cluster velocity coefficient, presented in Eq. (5.26), is used. Increasing the value of the coefficient increases the velocity at which particles fall in the annulus zone as

well as the radial velocity of particles. If the coefficient is not increased from its default value, it takes an unrealistically long time for the upper furnace to become emptied of solids.

Figure 6.25 shows the change in PA feed. At 30 seconds, it is instantly decreased from 250 kg/s to 0 kg/s, imitating a critical system failure in the PA fans.

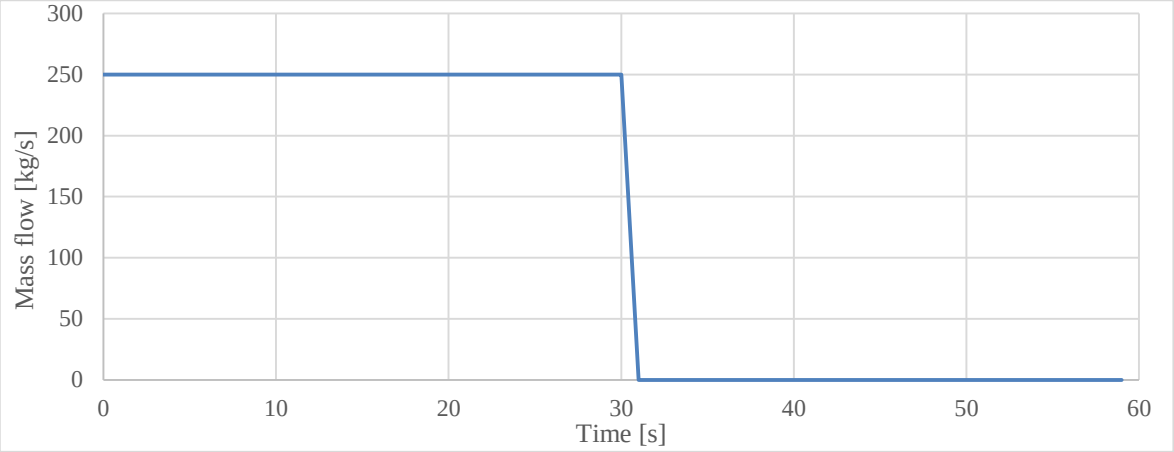

Figure 6.25. Case 5: Sudden stop in PA feed. PA mass flow.

Figure 6.26 shows the response of the bottom bed density and bed height to the sudden stop in the PA feed. The results seem plausible. Bed height instantly drops, as there is no more air flow to keep the bottom bed expanded. Then, the bed height starts to increase as the bed material from the upper furnace falls to the bottom bed. The suspension density in the bottom node only increases.

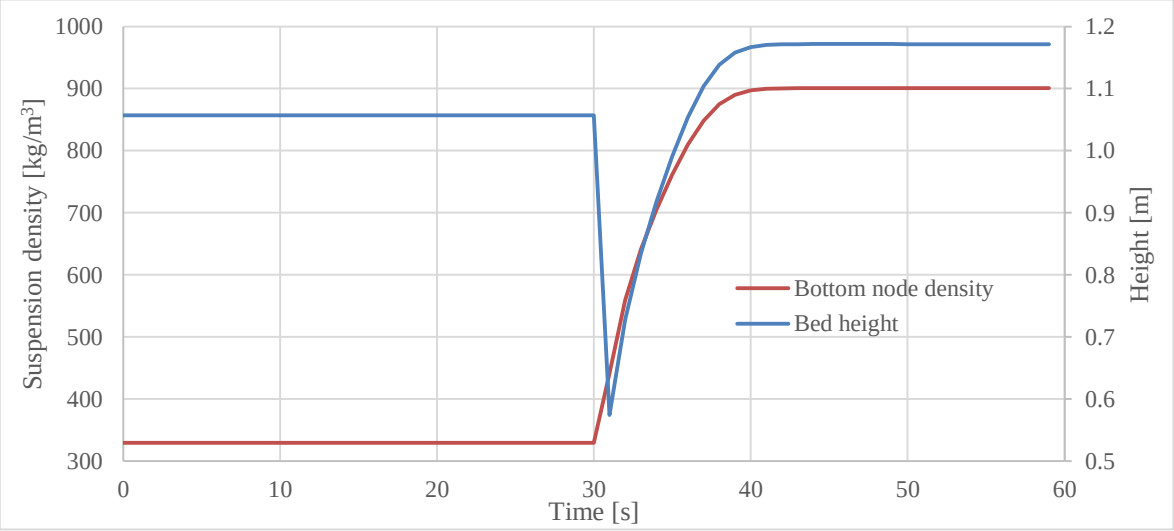

Figure 6.26. Case 5: Sudden stop in PA feed. Bottom bed height and bottom node suspension density.

Figure 6.27 shows the response of the top node suspension density to the change. When PA feed is suddenly stopped at 30 seconds, it takes only a few seconds for the top node to become emptied of solids. This seems realistic.

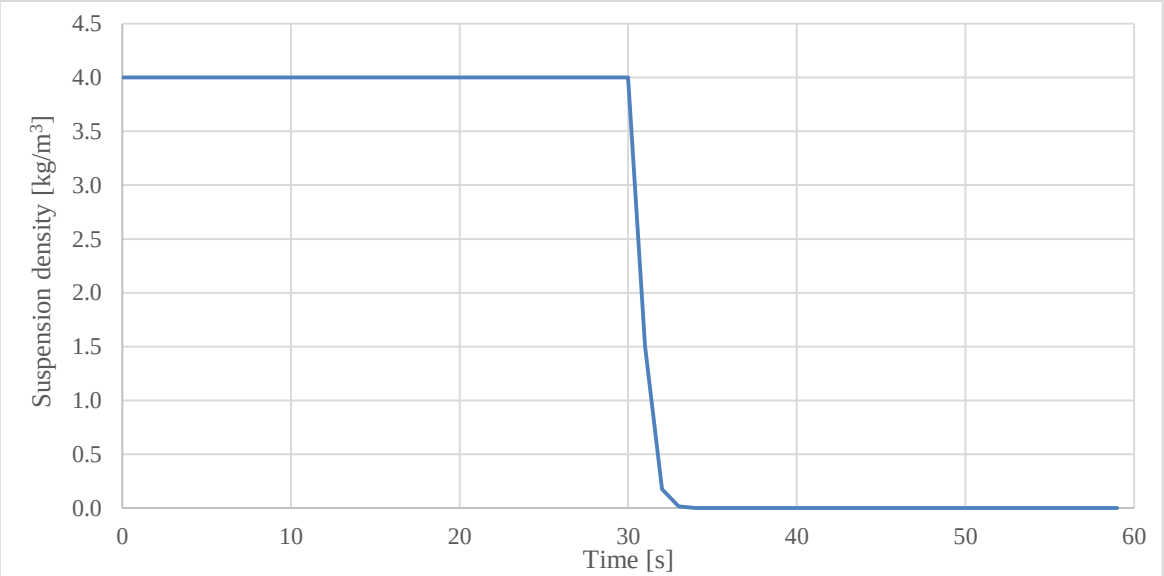

Figure 6.27. Case 5: Sudden stop in PA feed. Suspension density in the top node.

Figure 6.28 shows three important solid mass flows in the furnace. The results show that the mass flow leaving the bottom node as well as the mass flow of entrained material immediately goes to zero. The mass flow of material falling to the bottom bed from the upper furnace rises at first as the nodes above the bottom node, having high solid inventories, quickly unload to the bottom bed. Then, the mass flow decreases as the material inventory in the upper furnace decreases and because it takes more time for bed material in the upper nodes to fall to the bottom. It takes roughly 10…11 seconds before the mass flow to the bottom bed to becomes zero. The height of the furnace excluding the bottom node is 40 meters, so the average falling speed of the particles would be approximately 4 m/s. This seems plausible, as particle clusters may fall at the speed of 2…8 m/s, as stated in Chapter 3.2. Although it cannot be said if particle clusters exist in this kind of conditions, it could be assumed that the particles cannot be regarded as individual, but some kind of groups.

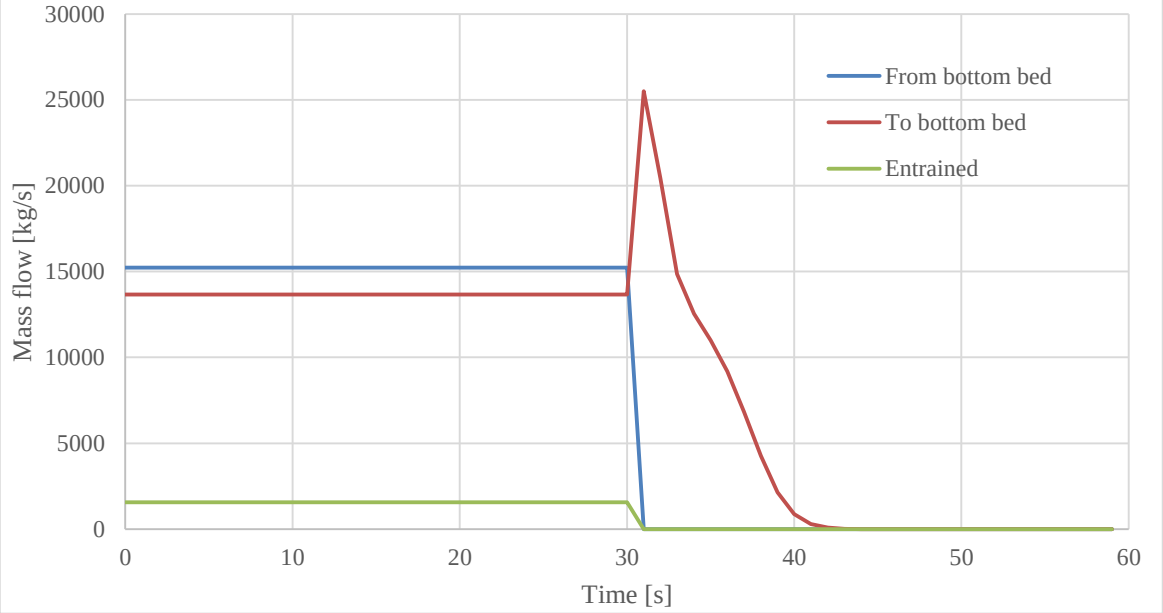

Figure 6.28. Case 5: Sudden stop in PA feed. Three important solids mass flows in the furnace: mass flows leaving and entering the bottom bed and the mass flow of entrained solids.

6.3 Verification of the Heat Transfer and Combustion Submodels

As the verification of the hydrodynamic submodel was successful, the heat transfer and combustion submodels are verified next. In order to verify these submodels, a boiler model is needed. The CFB model is connected to a water/steam cycle, and closed loop automation for the drum level is used to reach a new steady state after the change. The verification is done with an increase to the fuel feed.

6.3.1 Introduction of the CFB Boiler Model

The boiler model consists of only a section of a boiler at the vicinity of a CFB furnace, as it is the subject of interest. A schematic of the model is presented in Figure 6.29. The model includes superheating and reheating, but their properties are not discussed, as they add little to the verification. They however affect e.g. furnace conditions and were therefore included. Some key configuration values of the boiler and the fuel properties are presented in Appendix 4. The water/steam line utilizes the 6-equation model of Apros Solver. The 6-equation model solves the conservation equations for mass, momentum and energy for both water and steam flows inside the tubes and the drum.

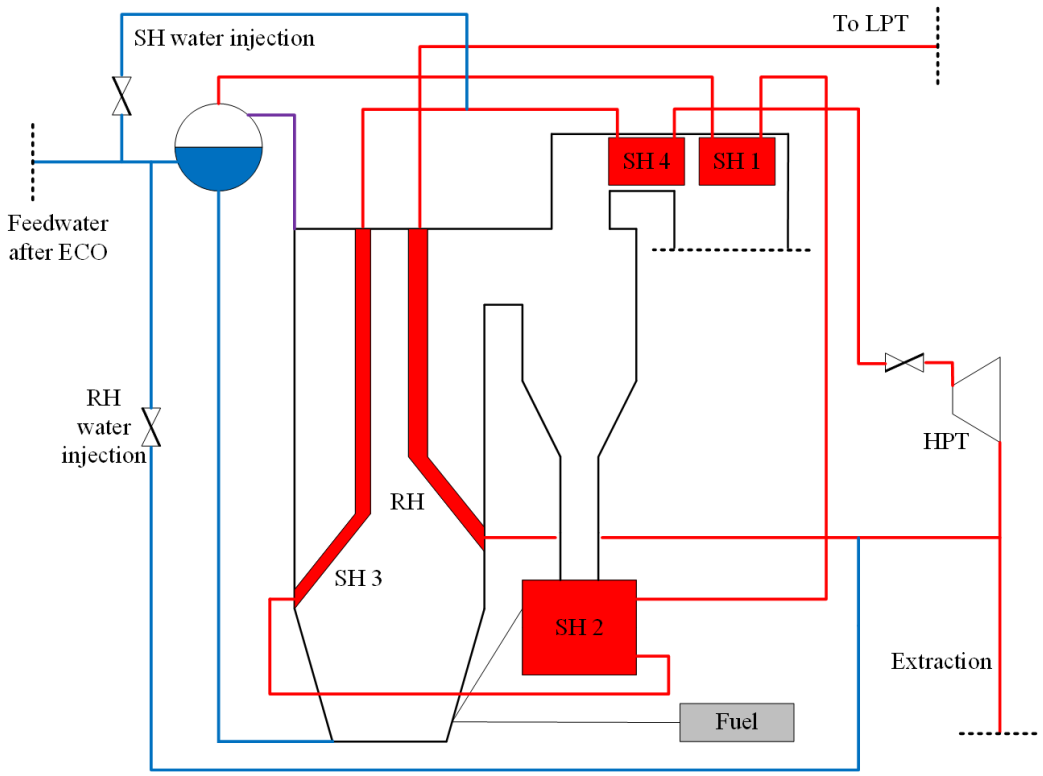

Figure 6.29. A schematic of the boiler model. Automation is not presented. The boundaries of the model are shown with dashed lines.

The main initial process values of the model are presented in Table 6.7. The initial state of the model is achieved by automating multiple process components. However, during these cases, almost all automation is open-loop, meaning that control loops are on manual mode. Only the drum level control is closed-loop, i.e., the drum level is controlled automatically. Open-loop operation makes the dependencies between input and output variables more clear and it is therefore used. The drum level control is closed-loop, because a larger heat flow from the furnace to the steam line would empty the drum and vice versa.

Table 6.7. Process design values of the boiler model.

Fuel input [kg/s]	27
Primary air [kg/s]	88
Secondary air [kg/s]	99
Primary air ratio [-]	0.47
Live steam temperature [°C]	525
Reheated steam temperature [°C]	525
Live steam mass flow [kg/s]	151
Reheated steam mass flow [kg/s]	119
Steam pressure at turbine inlet [bar]	149
Drum pressure [bar]	154

Another major simplification in the model is the external circulation. In this model, the external circulation is carried out with only one particle storage component (PSC) which combines the cyclone, standpipe and EHE. The mass flows entering and exiting the PSC are also equal at all times. As a result, the bed material inventory in the furnace and in the external inventories remain relatively constant at all times. This simplification causes the dynamics of the CFB and the heat transfer from the EHE to be more unrealistic. However, in this case, the external circulation does not change much, as only fuel feed is altered. Therefore, this simplification is considered justified.

As there is combustion included in the following case, the combustion model is briefly discussed. The CFB model utilizes the standard Apros reaction calculation by Ylijoki et al. (2016). The reaction rate of pyrolysis utilizes a modified version of the Arrhenius equation. The reaction rate of char combustion is assumed to depend mainly on the boundary layer diffusion. A separate time step is used for the reaction calculation. The time step is normally ten times shorter than the general simulation time step. The drying phase of fuel combustion is not included. The solid materials are given as dry substance in Apros and moisture in the fuel is inserted into the furnace as water.

6.3.2 Case 6. Increase in Fuel Feed

In Figure 6.30 it is shown that fuel feed is increased instantly by 3 kg/s at five minutes, while air feed is kept steady.

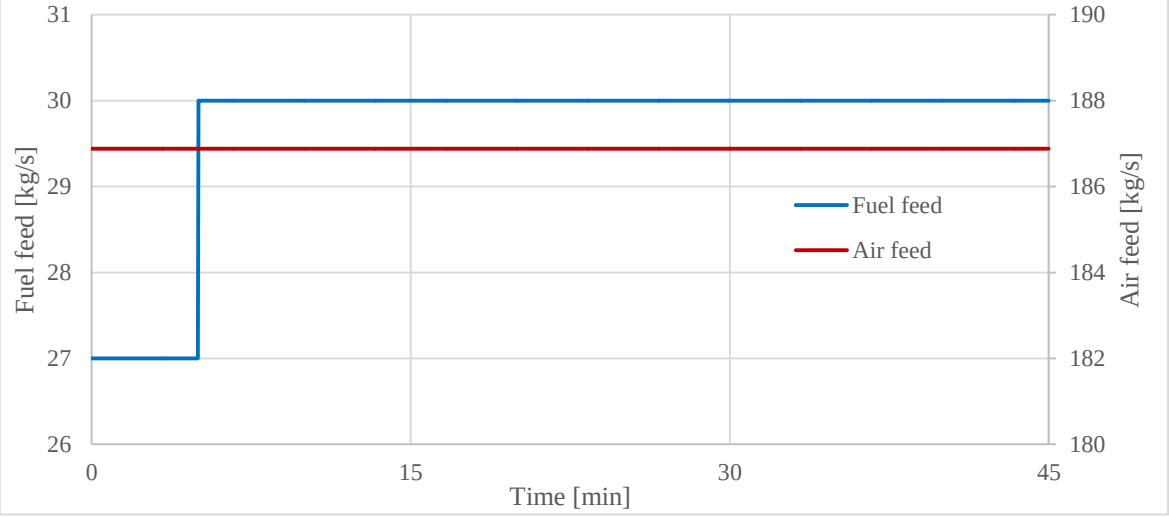

Figure 6.30. Case 6: Increase in fuel feed. Fuel and air feed rates.

Figure 6.31, Figure 6.32 and Figure 6.33 present the suspension density, temperature and heat transfer coefficient (HTC) profiles, respectively. The profiles are obtained from stationary states, at 5 minutes, before the change, and at 45 minutes. The suspension density profile becomes more uniform with the larger fuel feed, indicating elevated gas velocities. The temperature profile shows an increase with added fuel feed, therefore decreasing the gas density. A smaller density increases the gas velocity. The temperature profile is elevated with added fuel feed and its shape remains relatively similar to the lower fuel feed, which are realistic types of model behaviour. The shapes of the HTC profiles look very similar to the suspension density profiles. This is expected, as it was demonstrated in the sensitivity analysis in Chapter 5.8.2 that the value of the HTC depends mainly on the suspension density. As the shapes of the temperature profiles are similar, their effect is hardly seen in the HTC profiles.

The temperature difference between the bottom and top furnace is roughly 120 °C. The vertical temperature profiles found in literature are relatively uniform, so the model should be improved to make the results more realistic. The temperature profiles are, nevertheless, more uniform than in the previous CFB model, so the core-annulus structure was an improvement. However, the profile being still too uneven, there must be other factors contributing to the non-uniformity. This issue is further discussed in Chapter 7.2.

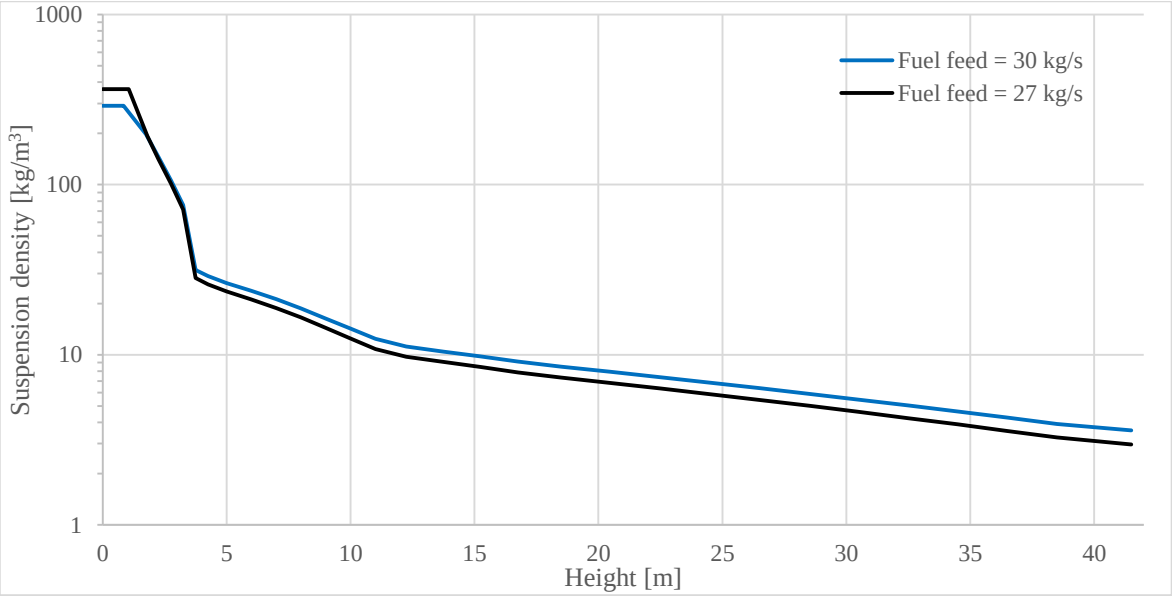

Figure 6.31. Case 6: Increase in fuel feed. Average suspension density profiles at two fuel feeds, obtained from steady states.

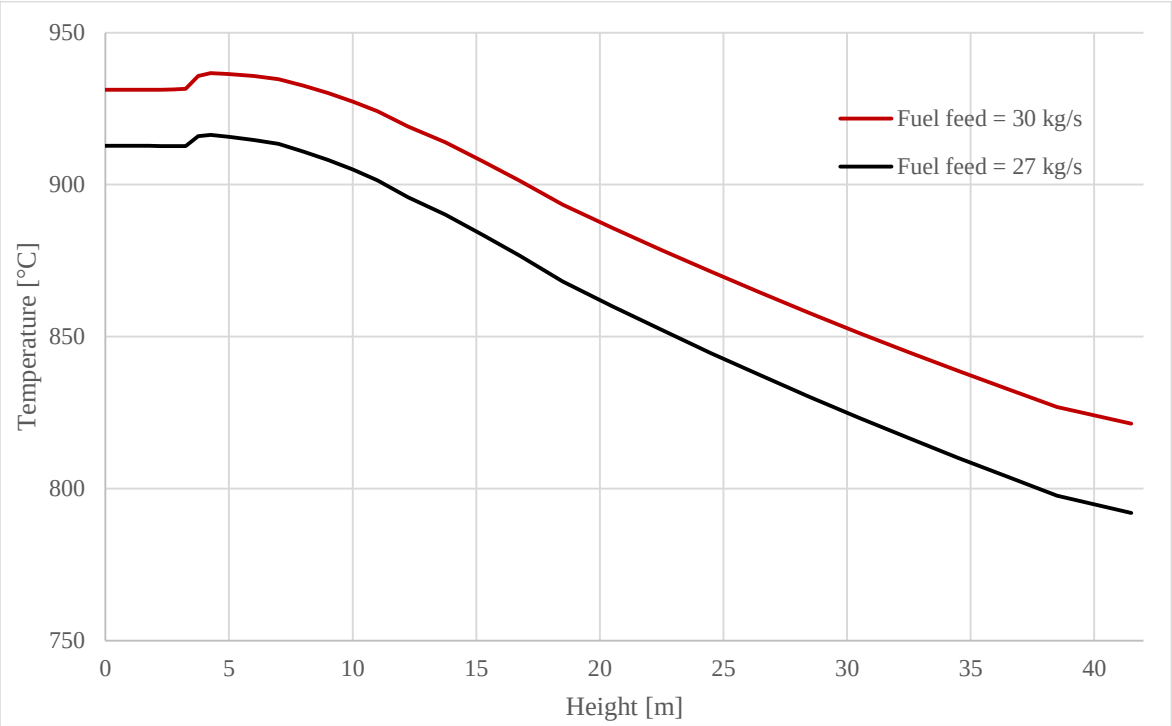

Figure 6.32. Case 6: Increase in fuel feed. Average furnace temperature profiles at two fuel feeds, obtained from steady states.

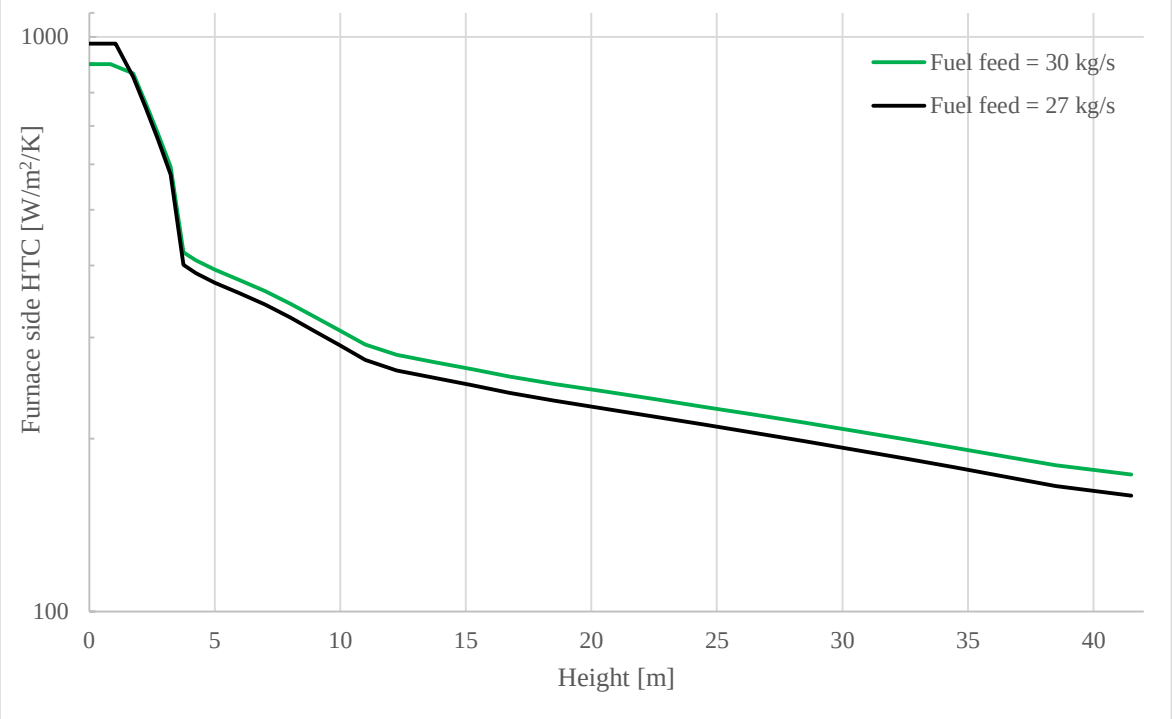

Figure 6.33. Case 6: Increase in fuel feed. Average HTC profiles at the furnace side at two fuel feeds, obtained from steady states.

Figure 6.34 displays solids temperature charts for the bottom and top nodes. When fuel feed is increased, the temperatures rise quickly. The bottom node temperature rises with a smaller gradient, because it has a much larger heat capacity due to the large solid inventory. The temperatures rise to their maximum at roughly 14 minutes, after which they decrease a minor amount and level off after 30 minutes. As the fuel feed is increased instantly, the steam line cannot entirely utilize the new addition of heat power fast enough. Some of the heat from the fuel feed is therefore stored in the bed material, and the temperatures rise. It takes time for the steam line process to reach the state in which it can fully utilize the added heat power. The additional heat stored in the bed material is therefore slowly released and the temperatures level off. The temperature at the top node rises 11 °C more than in the bottom. This is caused by the suspension density profile becoming more uniform, since the higher gas velocity is transporting more bed material to the upper furnace.

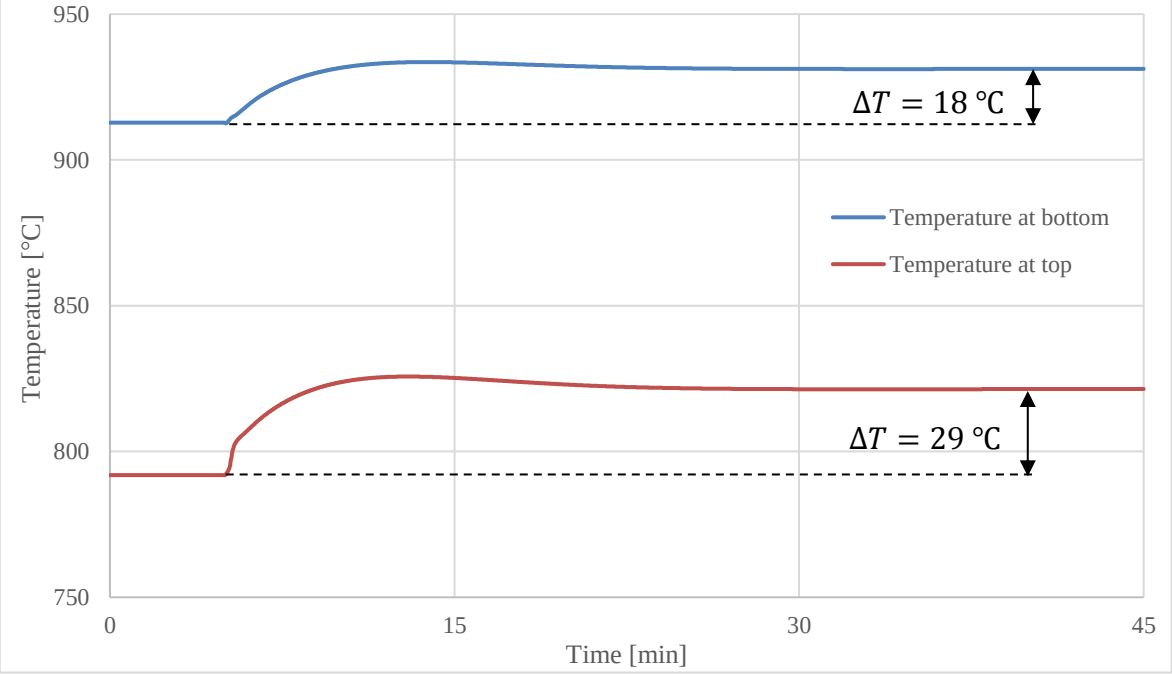

Figure 6.34. Case 6: Increase in fuel feed. Bottom and top node solids temperatures.

Figure 6.35 shows the progression of mass based O_2 concentration at the furnace exit. It takes only less than a minute for the O_2 concentration to reach a new steady state. For comparison, in the model of Kim et al. (2016, 5789), it takes over three minutes for the concentration to level off in a similar simulation case. A possible explanation is that the fuel in the Apros CFB model burns too quickly. This is further discussed in Chapter 7.2.

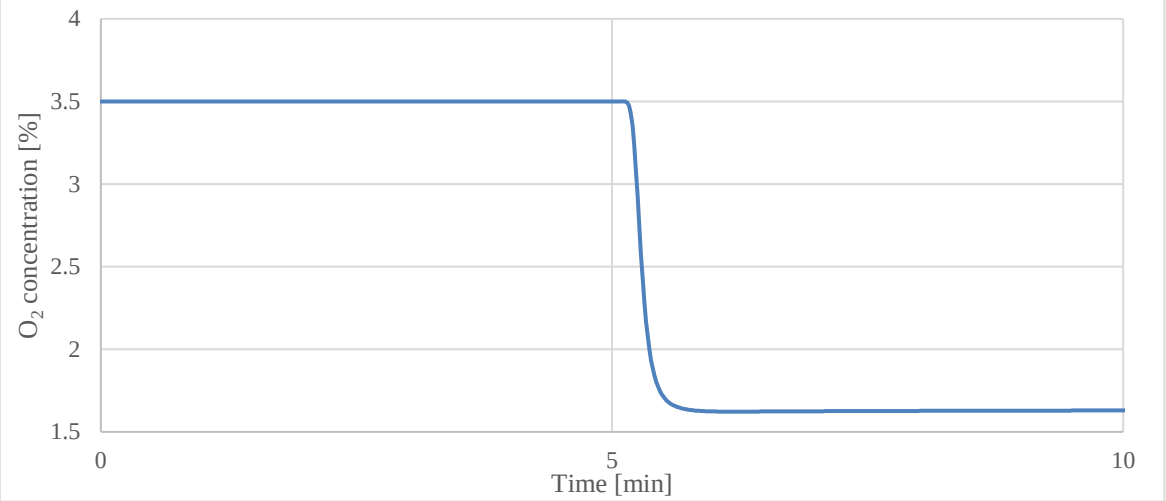

Figure 6.35. Case 6: Increase in fuel feed. Mass based oxygen concentration as at the furnace exit. Note that the time scale goes to only 10 minutes.

Figure 6.36 shows the water mass flows entering and exiting the drum as well as the drum level. The increased fuel feed generates steadily more steam in the steam line, showing as increased mass flow of saturated steam. The saturated steam mass flow increases steadily starting from the change in fuel feed and levels off to the end of the simulation. The feedwater mass flow and drum level should not be interpreted, as they are controlled with a feedback loop. Figure 6.37 shows the saturated steam temperature and pressure. They rise steadily, in a similar fashion as the saturated steam mass flow, after the change.

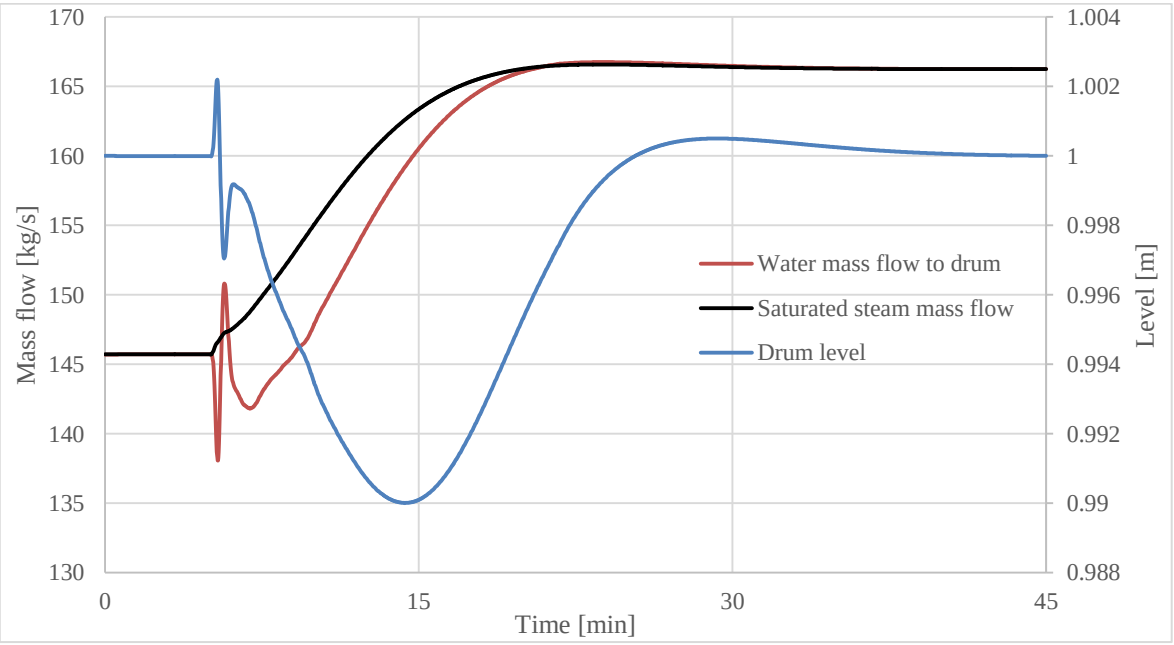

Figure 6.36. Case 6: Increase in fuel feed. Drum input and output mass flows and the drum level.

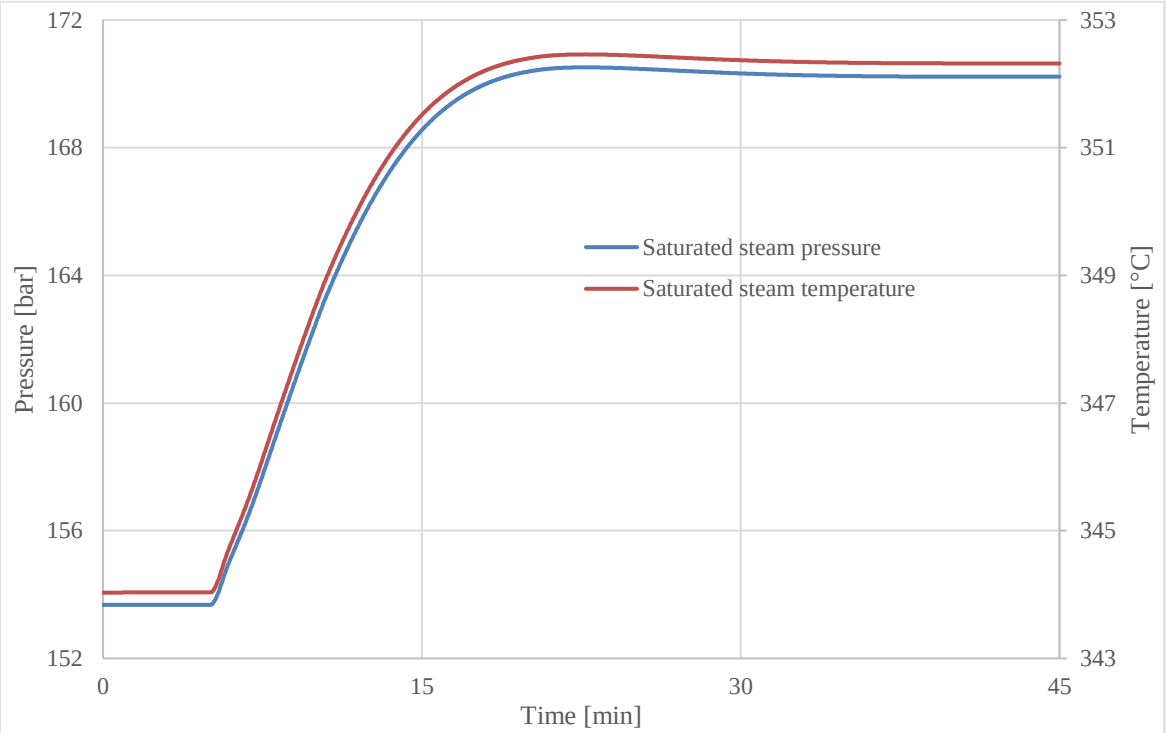

Figure 6.37. Case 6: Increase in fuel feed. Saturated steam parameters, immediately after the drum.

The drum level control is used so that a new stationary state can be reached. It is, however, important to see exactly how the drum level behaves in an open-loop simulation. Therefore, the same case was repeated with a constant feedwater mass flow to the drum. Figure 6.38 shows that the drum level generally rises for the first few minutes after the change and then starts to drop. As combustion power increases, vaporization in the water wall increases, i.e. volume fraction of steam increases and water fraction decreases. So, specific volume of water/steam mixture increases as there are more steam bubbles. Consequently, the water/steam volume increases, increasing the drum level. At 9 minutes, the mass balance difference between the feed water and saturated steam starts to show and the drum level decreases. These findings are similar to the results reported by Kim et al. (2016, 5789).

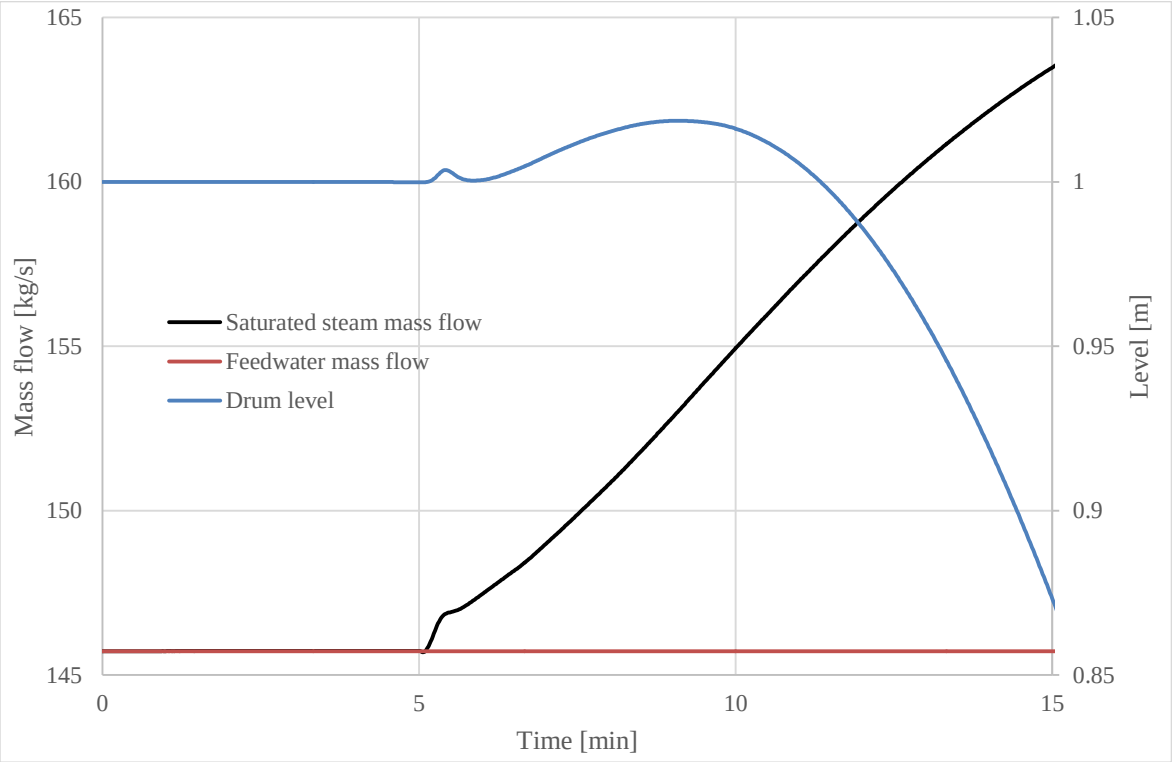

Figure 6.38. Case 6: Increase in fuel feed. A separate simulation study with an open-loop control for the drum level. Drum input and output mass flows and the drum level.

Case 6 shows that the CFB model works well, when connected to a water/steam line. As Apros components and thermohydraulic solvers have been extensively verified and validated for water/steam systems, this is expected. This simulation case was done with a very small focus on controllers to effectively demonstrate the behaviour of the CFB model. With well-tuned controllers, better results regarding the boiler system can be expected. The CFB model can therefore be used in simulating an entire CFB power plant, although quantitatively accurate results are unlikely and tuning of the CFB model is required.

7 DISCUSSION

Before the designing of the new Apros CFB model was started, some core development areas, such as startup, shutdown and the adding of new material into the furnace, were identified. Some of the modelling solutions of the new model were chosen on the basis of these issues. The split coefficients, interface density as well as radial and annulus zone velocities were developed to be essentially constant, improving the performance of the model in the aforementioned development areas. Declaring these attributes constant works well in several situations, but being constant, they respond unrealistically to some other changes in normal operation. However, plausible results can usually be obtained by controlling a single attribute.

In this chapter, the results presented in Chapter 6 are discussed in more detail. The feasibility of the model is evaluated based on the simulation cases, and issues are traced back to modelling solutions presented in Chapter 5. In addition, future development needs, identified by the simulation cases and testing the model, are addressed. The old and new model are also compared briefly.

7.1 Feasibility of the Model

Table 7.1 presents a summary of the simulation cases and the variables that needed to be tuned in each case. In three out of the six cases, one variable had to be tuned to get plausible results. The most significant of these is case 1, as it simulated a normal operating condition and the other two cases simulated special operating conditions. The model should not require tuning of variables during simulation in normal operating conditions. This decreases the feasibility of the model. In addition, the tuning and configuration of the model demands experience, knowledge and time, undermining its effectiveness. Therefore, on the basis of the verification cases, the model is not yet suitable for training simulator or boiler engineering purposes.

Table 7.1. Summary of the verification cases and the corresponding variables that needed to be tuned.

Case	Type of change	Operating condition	Tuned variable
1	Decrease in SA feed	Normal	Global α
2	Increase and decrease in bed material feed	Normal	None
3	Startup and shutdown	Special	Core extra velocity
4	Immediate stop of solids recirculation	Disturbance	Interface density
5	Immediate stop of fluidizing gas	Disturbance	None
6	Step change (increase) in fuel feed	Normal	None

Further development is needed to increase the feasibility of the model in certain areas and to make it more approachable for the user. The dynamic responses should go to the right directions without the need of case-specific control variables. Decreasing the need of control variables would greatly improve the model and make it easier for the modeller to use. The model is under development and it will be tested in actual training simulator projects. Further development and validation during the projects has been planned.

7.2 Future Development Needs

There were four main issues that were identified in the simulation cases and the testing of the model.

1. The temperature profile in the furnace was not as uniform as desired;
2. Decreasing the SA feed made the vertical suspension density profile of the furnace more uniform if split coefficient α was not adjusted;
3. The gas velocity profile was unrealistic, as the flow-area-decreasing effect of particles is not modelled, affecting also the suspension density profile;
4. The model lacks an effective way to tune the terminal velocity of the particles and therefore furnace hydrodynamics.

The first issue is the temperature profile in the furnace, discussed in case 6. Even after implementing the core-annulus approach, the temperature profile is not as uniform as desired. The vertical temperature profile should be relatively uniform in the entire furnace. The cause for the non-uniformity was identified as the solid fuel burning mostly in the lower furnace and too fast. Two main factors influence this: the size of the fuel particles and where the fuel is fed.

The CFB model does not model particle size distribution (PSD), meaning that all particles in the model are equally sized. As the size of the fuel particles is set to the size of the bed material, the particles burn very quickly in the furnace. Also, as the fuel is fed to the bottom node, where it is ideally mixed with the bed material, the solid fuel becomes trapped in the bottom node. For these reasons, too large an amount of solid fuel burns in the lower parts of the furnace, leaving too few to burn in the upper parts. Hence, the lower furnace is too hot and the upper furnace is too cold. Combustion calculation in Apros does not include the drying phase, which also affects the rate of combustion. But, as it is a relatively fast phenomenon, its effect is regarded insignificant.

As the fuel combustion is too fast, there are also too few fuel particles in the furnace. In Chapter 2.2 it was stated that according to Basu (2015, 92) the burning fuel particles normally comprise roughly 1…3 % of the bed material in the furnace. In case 6, the share of solid fuel was only 0.03 %, so approximately 30…100 times too little. The lack of fuel inventory in the bed also affects the dynamics of load change and does not allow the simulation of disturbances in the fuel feed. However, it must be noted that the fuel that was used was biomass. Biomass usually contains more volatiles and less char than e.g. coal, therefore burning more quickly, see Figure 3.10 in Chapter 3.3. The notion of 1…3 % of solid fuel is ambiguous, as the fuel inventory in the bed depends on the fuel. Therefore this information can only be used as a guideline.

The issue of solid fuel combustion should be fixed by enabling the modeler to choose the fuel feed height. If the fuel was fed to e.g. the second node of the CFB, the fuel would spread more evenly in the furnace. If the issue remains or if more accuracy is desired, PSD should be implemented. The PSD requires a significant development effort and demands considerably more calculation power, however. At the moment, the general combustion calculation in Apros has correction factors for the reaction speeds of all combustion reactions that are used. However, the factors do not work properly with the CFB model if changed from their default value, 1. The fixing of the reaction speed correction factors has already begun during this work. It should be thoroughly tested and verified, whether the different fuel feed height and reaction speed correction factors are enough to give adequate results.

The second issue is about the radial solid velocities, discussed in case 1. It was found that decreasing the SA feed increased the solid inventory above the injection point and decreased the inventory before it. This is unrealistic, as a smaller gas velocity inflicts less drag force on the particles, meaning that the solid inventory above the SA feed should decrease in this case. This problem can be traced back to the radial velocities of the solids. The velocities from core to annulus are calculated from the equations presented in Chapters 5.6.3 and 5.6.4, showing that they are normally roughly constant in the model. By using the attribute $k_{\mathrm{vel,a}}$, the annulus phase and therefore radial velocities can be made dependant on gas velocity. However, the effect of the variable to the radial velocity is not strong enough to make results plausible. Also, the annulus phase and radial solid velocities being equal at all times is unrealistic.

As the velocities remain constant, solids become trapped in the core nodes when the air feed is decreased, increasing the suspension densities in the upper furnace. As the upward gas velocity is decreased, the radial velocity of particles should rise and vice versa, implying an inverse proportionality of upward gas velocity to the radial solids velocity. This is also supported by the models of Gungor (2009) and Gungor & Eskin (2007) reviewed in Chapter 4. They had the following variable called the dispersion coefficient affecting the solid flow from core to annulus, from the reference (Hua et al. 2003, 972)

$$k = \frac{0.14}{u_{\mathrm{gas}} - u_{\mathrm{t}}} \tag{7.1}$$

By utilizing a similar modelling solution in the Apros CFB model, the dynamics of the suspension density profiles could be made more realistic. For example, the local split coefficients α_{i} could be replaced by the dispersion coefficient in some way and the global split coefficient could be kept as a control variable. There should be a restriction for the variable, when the gas velocity is equal to or less than the terminal velocity. The minimum value of the denominator could be e.g. 0.01 m/s. In a shutdown scenario, for instance, this would mean that when the fluidizing gas velocity decreases below the terminal velocity of the particles, bed material would quickly flow to the annulus and to the bottom bed.

The third issue is the gas velocity profile of the furnace, discussed in cases 1 and 2. The Apros CFB model does not take into account the decrease to gas flow area caused by the

particles. The decrease in the flow area increases the flow velocity, affecting bed hydrodynamics. By implementing this modelling solution, the model would give more realistic results when e.g. the material inventory of the furnace is changing.

The fourth issue is related to the terminal velocity of a particle. Currently, should the terminal velocity be tuned, it could only be done by changing the average particle size, density or sphericity. This kind of tuning is complicated and unpredictable. Instead, there should be a global control coefficient for terminal velocity. The coefficient would provide a simple and effective means for tuning the furnace hydrodynamics. This modelling solution could also effectively replace the variable adding extra velocity to the core nodes, introduced in Chapter 5.6.2.

The third and fourth development issue are relatively easy to implement to the model. The first and second issue are more complicated and require thorough research and development.

7.3 Comparison of the Old and New Apros CFB Model

The new CFB model was designed and implemented, because the old model did not perform well enough and did not allow the simulation of important special cases. The comparison of the models is summarised in Table 7.2. The new model performs better than the old model in terms of hydrodynamics, heat transfer and combustion. The new model responds better to changes in furnace conditions. In addition, furnace startup, shutdown and special cases can be simulated. The only ambiguous issue among the old and the new model is the need of fine-tuning of the model, as it is difficult to quantify. There is no open literature supporting the comparison of the models. The “old model” in this comparison is the CFB model in Apros version 6.07.

Table 7.2. Comparison of the old and new Apros CFB model with respect to issues of the old model and the required scope of operation of the new model.

Issues	Old model	New model	New model verified?
Response to changes in air feed	Only weak coupling between solids and air flow	Plausible, when using one control variable	In case 1
Sensitivity to changes in mass of solids	Very sensitive to both suspension profile and heat transfer	Not sensitive	In case 2
Startup and shutdown	No	Yes	In case 3
Emptying of the furnace	No	Yes	In case 4
Collapse of the bed	No	Yes	In case 5
Temperature profile	Non-uniform	More uniform	In case 6
Fine-tuning	Strongly needed, limited validity range	Improved	NA

8 CONCLUSIONS

The baseline for this work was to further develop and verify the Apros CFB model which is to be used in training simulators and engineering simulators. This formed three objectives for this thesis:

1. To gather a comprehensive theory basis on fluidization and existing dynamic 1D CFB models, focusing on the physical phenomena inside a CFB, especially hydrodynamics and heat transfer;
2. To document the modelling solutions implemented in the current Apros CFB model;
3. To develop and verify the CFB model so that the desired scope of operation is met.

The first and second objective were met in this work. The third objective was not entirely achieved, as there are still notable deficiencies in the model. Further development is therefore required regarding these deficiencies.

The theoretical overview first presents the basics of fluidization and fluidized bed technology. Secondly, the unique features and physical phenomena in a CFB are presented. The focus of the theoretical overview is on furnace hydrodynamics and heat transfer which were the objects of development for the CFB model in this thesis. The theory basis is broad and comprehensive, but does not go too much into detail on the physical phenomena. Thirdly, a review on dynamic 1D CFB models in literature was made. The modelling solutions presented in the review were not used directly in the Apros CFB model, but they still provided general information on some modelling solutions.

The documentation of the preliminary Apros CFB model is preceded by an overview on dynamic simulation, Apros simulation software and previous work regarding the CFB model. The documentation focuses on describing the new solid balance submodel and new features in the heat transfer submodel implemented in the CFB model. Sensitivity analyses were made for terminal velocity and the furnace side heat transfer coefficient and the modular structure of the CFB model was presented.

In the practical part of the work, the Apros CFB model, was verified. Six simulation cases were planned, in which only one variable was changed at a time to effectively show input-output dependencies. Five cases were carried out to verify the hydrodynamic submodel. The

model works well in most of the cases. The weaknesses of the model were exposed, showing that control variables are needed in order to obtain plausible results in some situations. These were most notably the changing of the SA feed, furnace startup and shutdown. The sixth case verified the heat transfer and combustion submodels in a CFB boiler with a step change in fuel feed. The results imitate the behaviour of a real CFB process. The major difference is that the fuel burns too quickly, showing in the responses of oxygen concentration at the furnace exit and the vertical temperature distribution in the furnace being too uneven.

The verification cases were successful, as they revealed the core development needs of the model.

1. The radial velocity of particles should depend on the gas velocity. Currently, it is almost constant, which leads to unrealistic results and need of tuning.
2. The flow-area-decreasing effect of bed material to gas flow should be taken into account. Currently, the solid phase affects the gas velocity only through energy and mass exchange as well as pressure drop.
3. The fuel feed elevation should be freely configurable and there should be a correction factor for combustion rate. Currently, the fuel is fed to the bottom node, and the solid fuel becomes trapped. Also, as all the bed material shares the same size, the fuel burns too quickly. These result in the temperature distribution inside the furnace being too uneven.

Based on the results of the simulation cases, the development of the CFB model continues. The model can be made to work in a plausible way, but it requires too much tuning, experience with the model and understanding CFB theory. To improve usability and to make the behaviour of the model more realistic, the issues should be fixed by further developing the model on the basis of the identified development needs. Development continues after this thesis, as especially combustion and heat transfer submodels have to be further tested. This was not possible in the scope of this thesis.

REFERENCES

Amec Foster Wheeler. 2016. *Amec Foster Wheeler wins contract for biomass fired CFB boiler*. [ONLINE] Available at: http://media.amecfw.com/amec-foster-wheeler-wins-contract-for-biomass-fired-cfb-boiler/. [Accessed 2.3.2018].

Apros. 2018. *General Guides, Apros Overview*. Apros Help Contents. Fortum & VTT.

Basu, Prabir. 2015. *Circulating Fluidized Bed Boilers: Design, Operation and Maintenance*. Cham: Springer International Publishing. ISBN 978-3-319-06173-3

Basu, P., & Fraser, S. 1991. *Circulating fluidized bed boilers design and operation.* Stoneham: Butterworth-Heinemann. ISBN 978-1-483-29230-4

Basu P, Nag PK. 1996. *Review of heat transfer in high temperature circulating fluidized bed.* Chemical Engineering Science, vol. 51, no. 1. ISSN 0009-2509

Bagheri, Gholamhossein & Bonadonna, Costanza. 2016. *On drag of freely falling non-spherical particles*. Powder Technology, vol 301, pp. 526–544. ISSN 0032-5910

Blaszczuk, Artur & Nowak, Wojciech. 2015. *Heat transfer behavior inside a furnace chamber of large-scale supercritical CFB reactor.* International Journal of Heat and Mass Transfer, vol. 87, pp. 464–480. ISSN 0017-9310

Blaszczuk, Artur & Nowak, Wojciech. 2014. *Bed-to-wall heat transfer coefficient in a supercritical CFB boiler at different bed particle sizes.* International Journal of Heat and Mass Transfer, vol. 79, pp. 736–749. ISSN 0017-9310

Brereton, C. M. H. & Grace, J. R. 1993. *Microstructural Aspects of the Behaviour of Circulating Fluidized Beds*. Chemical Engineering Science, vol. 48, no. 14, pp. 2565–2572. ISSN 0009–2509

Chen, Yang & Xiaolong, Gou. 2006. *Dynamic modelling and simulation of a 410 t/h Pyroflow CFB boiler*, Computers and Chemical Engineering, vol. 31, pp. 21–31. ISSN 0098–1354

da Silva, Francisco. 2015. *Dynamic Process Simulation: When do we really need it?* [ONLINE] Available at: http://processecology.com/articles/dynamic-process-simulation-when-do-we-really-need-it. [Accessed 31.7.2018].

Di Natale, F. & Nigro, R. *Heat and mass transfer in fluidized bed combustion and gasification systems*. Scala, Fabrizio. 2013. *Fluidized Bed Technologies for Near-Zero Emission Combustion and Gasification*. 1st edition. Oxford: Woodhead Publishing Limited. pp. 147–176. ISBN 978-0-85709-880-1

Dioguardi, Fabio & Mele, Daniela. 2015. *A new shape dependent drag correlation formula for non-spherical rough particles. Experiments and results*. Powder Technology, vol. 277, pp. 222–230. ISSN 0032-5910

Djerf, Tove, Pallarès, David & Johnsson Filip. 2018. *Bottom-bed fluid dynamics – Influence on solids entrainment.* Fuel Processing Technology, vol. 173, pp. 112–118. ISSN 0378-3820

Dutta, Animesh & Basu, Prabir. 2004. *An Improved Cluster-Renewal Model for the Estimation of Heat Transfer Coefficients on the Furnace Walls of Commercial Circulating Fluidized Bed Boilers.* Journal of Heat Transfer, vol. 126, pp. 1040–1043.

Dutta, Animesh & Basu, Prabir. 2002. *Overall heat transfer to water walls and wing walls of commercial circulating fluidized boilers*. Journal of the Institute of Energy, vol. 75, no. 504, pp. 85–90.

Fortum & VTT. 2017. *Basic Concepts 1*. Apros Training Material.

Grace, John & Bi, Hsiaotao. 1997. *Introduction to circulating fluidized beds*. Grace John, Avidan Amos, Knowlton Ted. *Circulating Fluidized Beds*. 1st edition. London: Chapman & Hall. pp 1–18. ISBN 987-94-010-6530-6

Grace, John & Lim, C. Jim. *Properties of circulating fluidized beds (CFB) relevant to combustion and gasification systems*. Scala, Fabrizio. 2013. *Fluidized Bed Technologies for Near-Zero Emission Combustion and Gasification*. 1st edition. Oxford: Woodhead Publishing Limited. pp. 147–176. ISBN 978-0-85709-880-1

Gungor, Afsin. 2009. *One dimensional numerical simulation of small scale CFB combustors*. Energy Conversion and Management, vol. 50, no. 3, pp. 711–722. ISSN 0196-8904

Gungor, Afsin & Eskin, Nurdil. 2007. *Analysis of environmental benefits of CFB combustors via one-dimensional model*. Chemical Engineering Journal, vol. 131, pp. 301–317. ISSN 1385-8947

Haider A., Levenspiel O. 1989. *Drag Coefficient and Terminal Velocity of Spherical and Nonspherical Particles*. Powder Technology, vol. 58, no. 1, pp. 63–70. ISSN 0032- 5910

Hannes, Jens. 1996. *Mathematical modelling of Circulating Fluidized Bed Combustion.* Doctor's thesis. Delft: Delft University of Technology. ISBN 3-88817-002-8

Hua, Yulong, Flamant, Gilles, Lu, Jidong & Gauthier, Daniel. 2003. *Modelling of axial and radial solid segregation in a CFB boiler.* Chemical Engineering and Processing, vol. 43, pp. 971–978. ISSN 0255-2701

Huang, J.-B., Wang, S.-W., Luo, Y., Zhao, Z.-C. & Wen, X.-Y. 2012. *Debates on the causes of global warming*. Advances In Climate Change Research, vol. 3, no. 1, pp. 38–44. ISSN 1674-9278

Huang, Yue. 2006. *Dynamic Model of Circulating Fluidized Bed.* Doctor's thesis. Morgantown, West Virginia: College of Engineering and Mineral Resources at West Virginia University.

Huhtinen, Markku et al. 2000. *Höyrykattilatekniikka*. 5th ed. Helsinki: Edita. ISBN 951-37-3360-2

Hyppänen, Timo & Raiko, Risto. *Leijupoltto*. Raiko, Risto, Kurki-Suonio, Ilmari, Saastamoinen, Jaakko & Hupa, Mikko. 1995. *Poltto palaminen.* 1st edition. Jyväskylä: Gummerus Kirjapaino OY. pp. 139–172. ISBN 951-666-448-2

IEA (International Energy Agency). 2017. *CO_2 Emissions From Fuel Combustion: Overview*.

Johansson, Andreas, Johnsson, Filip & Leckner, Bo. 2007. *Solids back-mixing in CFB boilers*. Chemical Engineering Science, vol. 62, no. 1, pp. 561-573. ISSN 0009-2509

Kim, Seongil, Choi, Sangmin, & Yang, Jongin. 2016. *Dynamic simulation of a circulating fluidized bed boiler system Part I: Description of the dynamic system and transient behavior of sub-models*. Journal of Mechanical Science and Technology, vol. 30, no. 12, pp. 5781–5792. ISSN 1738-494X

Kovacs, Jeno; Salo, Mikko; Ritvanen, Jouni; Hyppänen, Timo; Hultgren, Matias & Tourunen, Antti. 2012. *1-D Dynamic Simulation Study of Oxygen Fired Coal Combustion in Pilot and Large Scale CFB Boilers*. Coal Gen Europe, Poland 14–16.2.2012.

Krueger, B., Wirtz, S., Scherer, V. 2015. *Measurement of drag coefficients of non-spherical particles with camera-based method*. Powder Technology, vol. 278: no. 10. pp. 157–170. ISSN 0032-5910

Kunii, Daizo & Levenspiel, Octave. 1991. *Fluidization Engineering*. 2nd ed. Boston: Butterworth Heinemann. ISBN 0-409-90233-0

Lappalainen, Jari, Lalam, Virginie, Charreire, Romain & Ylijoki, Jukka. 2017. *Dynamic modelling of a CFB boiler including the solids, gas and water-steam systems*. Proceedings of the 12th International Conference on Fluidized Bed Technology (CFB-12), Krakow, Poland 23–26.5.2017. pp. 333–340.

Lappalainen, J., Tourunen, A., Mikkonen, H., Hänninen, M., Kovács, J.. 2014. *Modelling and dynamic simulation of a supercritical, oxycombustion circulating fluidized bed power plant concept – Firing mode switching case*. International Journal of Greenhouse Gas Control, vol. 28, pp. 11–24.

Lappalainen, J., Blom, H., Juslin, K.. 2012. *Dynamic process simulation as an engineering tool – A case of analysing a coal plant evaporator*. VGB Powertech, vol. 92, no. 1–2, pp. 62–68.

Myöhänen, Kari. 2011. *Modelling of combustion and sorbent reactions in three-dimensional flow environment of a circulating fluidized bed furnace*. Doctor's thesis. Lappeenranta: Lappeenranta University of Technology. ISBN 978-952-265- 161-7

Oka, Simeon. 2004. *Fluidized Bed Combustion*. 1st edition. New York: Marcel Dekker. ISBN 0-8247-4699-6

Pallarès, D. & Johnsson, F. *Modeling of fluidized bed combustion processes*. Scala, Fabrizio. 2013. *Fluidized Bed Technologies for Near-Zero Emission Combustion and Gasification*. 1st edition. Oxford: Woodhead Publishing Limited. pp. 147–176. ISBN 978-0-85709-880-1

Pallarès, D. & Johnsson, F. 2006. *Macroscopic modelling of fluid dynamics in large-scale circulating fluidized beds*. Progress in Energy and Combustion Science, vol. 32, pp. 539–569. ISSN 0360-1285

Phyllis2. 2006. *Database for biomass and waste*. [ONLINE] Available at: https://phyllis.nl/Browse/Standard/ECN-Phyllis#pellet [Accessed 20.8.2018].

Rim, GuanHe; Lee, DongHyun. 2016. *Bubbling to turbulent bed regime transition of ternary particles in a gas–solid fluidized bed*. Powder Technology, vol. 290, no. 4. ISSN 0032-5910

Ryabov GA, Kuruchkin AI & Folomeev OM. 1999. *Investigation of heat transfer to the waterwalls on an aerodynamic model of a circulating fluidized-bed boiler*. Thermal Engineering, vol. 46, no. 8, pp. 674–80.

Saastamoinen, Jaakko. *Kiinteän polttoaineen palaminen ja kaasutus*. Raiko, Risto, Kurki-Suonio, Ilmari, Saastamoinen, Jaakko & Hupa, Mikko. 1995. *Poltto palaminen.* 1st edition. Jyväskylä: Gummerus Kirjapaino OY. pp. 139–172. ISBN 951-666-448-2

Scala, F., Solimene, R. & Montagnaro, F. *Conversion of solid fuels and sorbents in fluidized bed combustion and gasification*. Scala, Fabrizio. 2013. *Fluidized Bed Technologies for Near-Zero Emission Combustion and Gasification*. 1st edition. Oxford: Woodhead Publishing Limited. pp. 319–387. ISBN 978-0-85709-880-1

Teir, Sebastian. 2003. *Steam boiler technology*. 2nd ed. Espoo: Helsinki University of Technology. ISBN 951-22-6759-4

Thacker, Ben, Doebling, Scott, Hemez, Francois, Anderson, Mark, Pepin, Jason & Rodriguez, Edward. 2004. *Concepts of Model Verification and Validation*. Los Alamos National Laboratory.

Tuuri, Sami & Lappalainen, Jari. 2018. *Requirements Specification for Apros CFB Improvement. Internal Report.* 24 pages. Collaboration of Fortum & VTT.

Vakkilainen, Esa. 2017. *Steam Generation from Biomass: Construction and Design of Large Boilers*. 1st ed. Oxford: Butterworth-Heinemann. ISBN 978-0-12-804389-9

Wang, Xiaoxin, Jiang, Dabang & Lang, Xianmei. 2016. *Future extreme climate changes linked to global warming intensity*. Science Bulletin, vol. 62, no. 24, pp. 1673–1680. ISSN 2095-9273

Werther, Joachim & Reppenhagen, Jens. *Attrition.* Yang Wen-Ching. 2003. Handbook of Fluidization and Fluid-Particle Systems. 1st edition. New York: Marcel Dekker. ISBN 0-8247-0259-X

Ylijoki, Jukka, Hänninen, Markku, Keinonen, Marja, Savolainen, Jouni, Lappalainen, Jari, Norrman, Sixten. 2016. *Chemical Reaction Simulation in Apros.* Apros Help Contents. VTT.

Zhou, J., Grace, J.R., Lim, C.J. and Brereton, C.M.H. 1995. *Particle velocity profiles in a circulating fluidized bed riser of square cross-section*. Chemical Engineering Science vol. 50, no. 2, pp. 237–244. ISSN 0009-2509

APPENDIX 1. DERIVATION OF EQUATIONS (5.11)…(5.13)

The objective is to find the formulation of suspension density in the last (topmost) node, ρ_{N}, as a function of interface density and split coefficients α. Because the density of the last node and the split coefficients α are known beforehand, the interface density can then be solved from the equation. First, we calculate the density of a core node i (2…N). It can be derived from the mass balance of a core node, from Eq. (5.2).

$$\frac{d\rho_{\mathrm{c,i}}(t)}{dt}V_{\mathrm{i}} = \dot{m}_{\mathrm{c,i-1}}(t) - \dot{m}_{\mathrm{c,i}}(t) + \dot{m}_{\mathrm{ac,i}}(t) - \dot{m}_{\mathrm{ca,i}}(t) \tag{A1.1}$$

In steady state, the left hand side of Eq. (A1.1) is zero. Also, the flow from the annulus phase back to the core phase is neglected, giving

$$0 = \dot{m}_{\mathrm{c,i-1}} - \left(\dot{m}_{\mathrm{c,i}} + \dot{m}_{\mathrm{ca,i}}\right) \tag{A1.2}$$

$$\begin{aligned} 0 = {} & (1-\alpha_{\mathrm{i-1}}) \cdot A_{\mathrm{i-1}} \cdot u_{\mathrm{c,i-1}} \cdot \rho_{\mathrm{c,i-1}} \\ & - \left((1-\alpha_{\mathrm{i}}) \cdot A_{\mathrm{i}} \cdot u_{\mathrm{c,i}} \cdot \rho_{\mathrm{c,i}} + \alpha_{\mathrm{i}} \cdot A_{\mathrm{i}} \cdot u_{\mathrm{a,i}} \cdot \rho_{\mathrm{c,i}}\right) \end{aligned} \tag{A1.3}$$

The rightmost term in Eq. (A1.3) includes the entire solid flow leaving the core node.

$$\begin{aligned} & \rho_{\mathrm{c,i}}\left((1-\alpha_{\mathrm{i}}) \cdot A_{\mathrm{i}} \cdot u_{\mathrm{c,i}} + \alpha_{\mathrm{i}} \cdot A_{\mathrm{i}} \cdot u_{\mathrm{a,i}}\right) \\ & \quad = (1-\alpha_{\mathrm{i-1}}) \cdot A_{\mathrm{i-1}} \cdot u_{\mathrm{c,i-1}} \cdot \rho_{\mathrm{c,i-1}} \end{aligned} \tag{A1.4}$$

The solid density of a core node i (2…N) is

$$\rho_{\mathrm{c,i}} = \rho_{\mathrm{c,i-1}} \cdot (1-\alpha_{\mathrm{i-1}}) \frac{A_{\mathrm{i-1}} u_{\mathrm{c,i-1}}}{(1-\alpha_{\mathrm{i}}) \cdot A_{\mathrm{i}} \cdot u_{\mathrm{c,i}} + \alpha_{\mathrm{i}} \cdot A_{\mathrm{i}} \cdot u_{\mathrm{a,i}}} \tag{A1.5}$$

The solid density of the core node 1 is derived from a similar mass balance equation as Eq. (A1.4).

$$(1-\alpha_1) A_1 \cdot u_{\mathrm{c,1}} \cdot \rho_{\mathrm{c,1}} + \alpha_1 \cdot A_1 \cdot u_{\mathrm{a,1}} \cdot \rho_{\mathrm{c,1}} = u_{\mathrm{c,0}} \cdot \rho_{\mathrm{int}} \cdot A_0 \tag{A1.6}$$

where 0 denotes the bottom bed.

$$\rho_{\mathrm{c,1}} = \rho_{\mathrm{int}} \cdot \frac{A_0 u_{\mathrm{c,0}}}{(1-\alpha_1) A_1 \cdot u_{\mathrm{c,1}} + \alpha_1 \cdot A_1 \cdot u_{\mathrm{a,1}}} \tag{A1.7}$$

By combining equations (A1.5) and (A1.7), we get

$$\rho_{\mathrm{c,N}} = \rho_{\mathrm{int}} \cdot \frac{A_0 u_{\mathrm{c},0}}{(1-\alpha_1)A_1 \cdot u_{\mathrm{c},1} + \alpha_1 \cdot A_1 \cdot u_{\mathrm{a},1}} \cdot \prod_{\mathrm{i}=1}^{\mathrm{N}-1}(1-\alpha_{\mathrm{i}}) \cdot \prod_{\mathrm{j}=2}^{\mathrm{N}} \left(\frac{A_{\mathrm{j}-1} u_{\mathrm{c,j}-1}}{(1-\alpha_{\mathrm{j}}) \cdot A_{\mathrm{j}} \cdot u_{\mathrm{c,j}} + \alpha_{\mathrm{j}} \cdot A_{\mathrm{j}} \cdot u_{\mathrm{a,j}}} \right) \quad \text{(A1.8)}$$

$$\rho_{\mathrm{c,N}} = \rho_{\mathrm{int}} \cdot \prod_{\mathrm{i}=1}^{\mathrm{N}-1}(1-\alpha_{\mathrm{i}}) \cdot \prod_{\mathrm{j}=1}^{\mathrm{N}} \left(\frac{A_{\mathrm{j}-1} u_{\mathrm{c,j}-1}}{(1-\alpha_{\mathrm{j}}) \cdot A_{\mathrm{j}} \cdot u_{\mathrm{c,j}} + \alpha_{\mathrm{j}} \cdot A_{\mathrm{j}} \cdot u_{\mathrm{a,j}}} \right) \quad \text{(A1.9)}$$

$$\rho_{\mathrm{c,N}} = \rho_{\mathrm{int}} \cdot C \quad \text{(A1.10)}$$

The suspension density of the node N includes also the density of the annulus node. It can be derived from a similar mass balance equation as Eq. (A1.4). The left hand side represents the mass flow from the core node N to the annulus node N, and the right hand side represents the mass flow leaving the annulus node N.

$$\alpha_{\mathrm{N}} \cdot A_{\mathrm{N}} \cdot u_{\mathrm{a,N}} \cdot \rho_{\mathrm{c,N}} = A_{\mathrm{N}-1} \cdot u_{\mathrm{a,N}} \cdot \rho_{\mathrm{a,N}} \quad \text{(A1.11)}$$

$$\rho_{\mathrm{a,N}} = \rho_{\mathrm{c,N}} \cdot \alpha_{\mathrm{N}} \frac{A_{\mathrm{N}}}{A_{\mathrm{N}-1}} \quad \text{(A1.12)}$$

$$\rho_{\mathrm{a,N}} = \rho_{\mathrm{c,N}} \cdot D \quad \text{(A1.13)}$$

The density of the final node is

$$\rho_{\mathrm{N}} = \rho_{\mathrm{c,N}} + \rho_{\mathrm{a,N}} \quad \text{(A1.14)}$$

$$\rho_{\mathrm{N}} = \rho_{\mathrm{c,N}} + \rho_{\mathrm{c,N}} \cdot D = \rho_{\mathrm{c,N}}(1+D) \quad \text{(A1.15)}$$

$$\rho_{\mathrm{N}} = \rho_{\mathrm{int}} \cdot C \cdot (1+D) \quad \text{(A1.16)}$$

Finally, the interface density is

$$\rho_{\mathrm{int}} = \frac{\rho_{\mathrm{N}}}{C(1+D)} \quad \text{(A1.17)}$$

where

$$C = \prod_{\mathrm{i}=1}^{\mathrm{N}-1}(1-\alpha_{\mathrm{i}}) \cdot \prod_{\mathrm{j}=1}^{\mathrm{N}} \left(\frac{A_{\mathrm{j}-1} u_{\mathrm{c,j}-1}}{(1-\alpha_{\mathrm{j}}) \cdot A_{\mathrm{j}} \cdot u_{\mathrm{c,j}} + \alpha_{\mathrm{j}} \cdot A_{\mathrm{j}} \cdot u_{\mathrm{a,j}}} \right) \quad \text{(A1.18)}$$

$$D = \alpha_{\mathrm{N}} \frac{A_{\mathrm{N}}}{A_{\mathrm{N}-1}} \quad \text{(A1.19)}$$

APPENDIX 2. SCL SCRIPT FOR MASS AND HEAT BALANCE SIMULATION

```
import "Apros/Legacy"
import "Apros/Simulation"

// We want the energy output and mass output to be 0 at the beginning
// of simulation. Therefore, the initial values of the outputs
// are subtracted from the outputs. Because of this, the two curves in the
// balance graphs both start from zero and are easy to compare.
// The analog signal names are different in both models.
analogComponents_BB = ["XA09", "XA12", "XA53", "XA71"]
analogComponents_UF = ["XA12", "XA73", "XA53", "XA71"]
massOutput    = agetV (analogComponents_UF!0) "ANALOG_VALUE" :: Double
energyScaling = amodi (analogComponents_UF!1) "ANALOG_VALUE" massOutput
energyOutput  = agetV (analogComponents_UF!2) "ANALOG_VALUE" :: Double
energyScaling = amodi (analogComponents_UF!3) "ANALOG_VALUE" energyOutput

// We want to store the current values in variables to be used later.
// Function agetV fetches the attribute value of the component and
// returns it as Double. (agetV component attribute :: DataType)
solidsFeedCoeffInit = agetV "VT02"  "VT_COEFFICIENT"          :: Double
massFlowInit        = agetV "PIP04" "PI12_MIX_MASS_FLOW"      :: Double
temperatureInit     = agetV "PO01"  "PO11_TEMPERATURE"        :: Double

// Here are all the function parameters that we will use in simulation.
// They are given as a list of tuples, so each element of the list consists
// of (module, attribute, value, simulation time).
// The simulation time is included, because for example change in
// return mass flow (VT_COEFFICIENT) has a much larger impact than
// for example fluidizing gas mass flow.

solidsFeedTime  = 10*60 :: Double  // one minute
massFlowTime    = 10*60 :: Double
temperatureTime = 20*60 :: Double

modifyingList = [
    ("VT02",  "VT COEFFICIENT",     (solidsFeedCoeffInit * 1.001), solidsFeedTime),
    ("VT02",  "VT COEFFICIENT",     (solidsFeedCoeffInit * 0.999), solidsFeedTime),
    ("VT02",  "VT COEFFICIENT",     (solidsFeedCoeffInit),         solidsFeedTime),
    ("PIP04", "PI12_MIX_MASS_FLOW", (massFlowInit * 1.1),          massFlowTime),
    ("PIP04", "PI12_MIX_MASS_FLOW", (massFlowInit * 0.9),          massFlowTime),
    ("PIP04", "PI12_MIX_MASS_FLOW", (massFlowInit),                massFlowTime),
    ("PO01",  "PO11 TEMPERATURE",   (temperatureInit + 30.0),      temperatureTime),
    ("PO01",  "PO11 TEMPERATURE",   (temperatureInit - 30.0),      temperatureTime),
    ("PO01",  "PO11_TEMPERATURE",   (temperatureInit),             temperatureTime)
    ]

// Simulation speed to max, and then initial simulation for 5 minutes.
setSpeed 1000000
step (5*60)

// In each iteration we have a new list element (which is a tuple). We tell at the
// beginning that the first tuple element is called "module", the second is
// "attribute" etc. Then the module attribute is modified to the given value,
// and simulation is run for  given time.
for modifyingList (\(module, attribute, value, time) -> do
    amodi module attribute value
    step time
)
step (30*60)

// eof
```

APPENDIX 3. MODELLING PARAMETERS USED IN THE CASES

This appendix contains the node heights, split coefficients α and interface densities used in the cases in Chapter 6.2. The node heights of the model are:

- Node 1: $h = 1.5$ m
- Nodes 2…7: $h = 0.5$ m
- Nodes 8…14: $h = 1$ m
- Nodes 15…18: $h = 1.5$ m
- Nodes 19…30: $h = 2$ m

The case model uses local alfas and they are given as follows:

- For nodes 2…5, $\alpha_{\mathrm{local}} = 2$
- For nodes 6…14, $\alpha_{\mathrm{local}} = 1$
- For nodes 15…29, $\alpha_{\mathrm{local}} = 0.5$

APPENDIX 4. MODELLING VALUES USED IN CASE 6

Table A4.1. Configuration values used in case 6.

Bed height [m]	41.5
Area at grid level [m^2]	80
Area at 7.5 m [m^2]	200
Area at 41.5 m [m^2]	200
Bed mass [kg]	140 000
Particle density [kg/m^3]	2400
Particle diameter [µm]	250
Particle sphericity [-]	0.8
Cluster velocity coefficient [-]	6
Number of tubes, water wall [-]	400
Tube inside radius, water wall [mm]	30
Number of tubes, SH wing wall [-]	250
Tube inside radius, SH wing wall [mm]	24
Tube length, SH wing wall [m]	34
Number of tubes, RH wing wall [-]	350
Tube inside radius, RH wing wall [mm]	30
Tube length, RH wing wall [m]	27
Air inlet temperature [°C]	250
Feedwater inlet temperature [°C]	300
Feedwater inlet pressure [bar]	176

Table A4.2. Fuel properties used in case 6. Wood pellets are used as the fuel (Phyllis, fuel ID #2808).

		Unit	Value, ar	Value, dry
Proximate analysis	Moisture content	wt%	8.7	
	Ash content	wt%	0.46	0.5
	Volatile matter	wt%	74.4	81.49
	Fixed carbon	wt%	16.44	18.01
Ultimate analysis	Carbon	wt%	45.79	50.15
	Hydrogen	wt%	5.54	6.07
	Oxygen	wt%	39.43	43.18
	Nitrogen	wt%	0.08	0.09
	Sulphur	wt%	0.01	0.01
	Net calorific value, LHV	MJ/kg	16.78	18.61